Università degli Studi Roma TRE

e

Consorzio Nazionale Interuniversitario per le Scienze Fisiche della Materia

Dottorato di Ricerca in Scienze Fisiche della Materia
XXIV ciclo

Titolo

Laboratory phase contrast nano-imaging using X-ray waveguide

Tesi di dottorato del dott. Andrea Sorrentino

Relatore

Dott. Alessia Cedola

Coordinatore Dottorato

Prof. Settimio Mobilio

a. a. 2011/2012

alla mia famiglia

Contents

Introduction

A major use of X-rays, ever since they were discovered over a century ago, has been and still is the visualization of the inside of systems which are not transparent for visible light. Whatever the imaging process used, it implies the registration of an inhomogeneous intensity on a detector. The physical mechanism leading to this contrast characterizes the various kinds of image. Absorption radiographs are still by far the most common X-ray images, both for medical and technical needs. In this case contrast has been based on the difference in absorption coefficient of different materials. However, small samples consisting of light elements, such as organic samples, show very weak absorption contrast, even at soft X-ray energies. More pronounced contrast can be obtained if also the phase-shift of the probing X-ray beam introduced by the sample is measured. Any imaging technique that converts this phase shift in measurable intensity modulations is called Phase Contrast Imaging (PCI) [Nugent, 1996]. By utilizing phase contrast rather than absorption contrast only, a good contrast can be achieved using high energy hard X-ray ($E \geq 8$ keV). In this way the absorbed dose, which often limits the spatial resolution achievable in microscopy, can be reduced considerably. Moreover hard X-ray photons allow a simpler sample environment and preparation: the sample does not need to be put into vacuum. These facts make PCI very suitable for the imaging of biological specimen. Also for this reason PCI has become an active field of research and now it plays an important role among the various kind of imaging techniques, covering a wide range of applications. Many X-rays PCI techniques have been successfully developed and applied nowadays. We can distinguish between lens-based and lens-less microscopy and imaging. A lens based X-ray microscope requires complicated and often expansive optical devices such as the Fresnel Zone Plates and the achievable resolution is often limited just by the imperfections of the utilized optics setup. To overcome these limitations a lens-less PCI method based on the propagation in free space had been extensively studied and developed: the Propagation based Phase Contrast Imaging (PPCI).

Till the first attempts, it was clear that the coherence properties of the X-ray beam impinging on the sample are fundamental in order to realize successful PPCI experiments. For this reasons the first important results were obtained at the modern synchrotron radiation sources (see for example [Snigirev, 1995]). In general modern synchrotron radiation sources offer best possibilities for hard X-ray imaging, especially for PCI. The key factors are the intensity, stability, homogeneity and coherence of the beams, sometimes control over polarisation, and/or the possibility of easy producing sub-micrometer sized spots. The problem is that the scale and cost of such sources limit the applicability of high resolution phase contrast microscopy and coherent methods both in bio-medicine and in industrial processing. Therefore there is still a need to scale down PCI techniques to conventional table top laboratory source. One of the most promising techniques to do this is the waveguide assisted-PPCI. An X-ray WG can be schematized as a very narrow channel in which the X-ray beam can be confined and propagates by multiple total reflections. A WG can produce a nano size divergent beam which can be used for projection microscopy with a very high resolution, limited only by the size of the source, i.e. by the exit gap dimension of the WG. Remarkably the WG beam can be spatially coherent and this property can be used also to implement hard X-ray holography and the recent Coherent X-ray Diffraction Imaging (CXDI) [Van der Veen, 2004].

During this PhD work, a high resolution ($\approx$200-300 nm) WG-based X-ray propagation-phase contrast microscope had been designed and realized at the X-ray laboratory of the Institute for Photonics and Nanotechnologies, CNR. It had been successfully used to implement high resolution X-ray phase contrast microscopy as well as X-ray holography in one dimension. The transition to two dimensions applications is under processing.

The thesis is organized as follows:

Chapter 1:

The basics features of X-ray PCI, the advantageous with respect to the standard absorption imaging technique and an overview on the principal X-ray PCI methods are reported. Finally the PPCI technique is deeply discussed.

Chapter 2:

The basic theory and the fundamental concepts of the X-ray WG are reported both with a study on the X-ray WG self imaging effect.

Chapter 3:

The chapter is devoted to the description of the WG fabrication processes.

Chapter 4:

The chapter describes the basics features of the WG based phase contrast microscope and the characterization of the WG beam.

Chapter 5:

A quantitative holographic reconstruction of a test sample is attempted using two different reconstruction methods.

Chapter 6:

Some interesting phase contrast microscopy results on human hair fibres are reported.

All the chapters start with a brief introduction.

1. X-ray phase contrast imaging

Phase Contrast Imaging (PCI) is any imaging technique that converts the X-ray beam phase variations due to the interaction with the sample in measurable intensity modulations [Nugent, 1996]. Before going insight the classification and the description of the various PCI techniques (section 1.4), when and why PCI is preferable with respect to standard absorption technique will be explained. With this aim, the X-ray refraction index will be introduced (1.1) and connected with the transmission function of the sample (1.2). Moreover, some considerations about the benefits in terms of radiation dose will be making (1.3). The Propagation based PCI technique will be described in details in section (1.5). Finally a simulation program able to predict the intensity distribution on the detector plane using some approximations, will be described in section (1.6).

1.1 X-rays Refraction Index

The refraction index of a material is defined as the ratio between the speed of light in vacuum and the speed of light in the material:

$$n = \frac{c}{v} = \frac{\sqrt{\varepsilon\mu}}{\sqrt{\varepsilon_0\mu_0}} \approx \sqrt{\varepsilon_r} \qquad (1.1)$$

and from Maxwell equations results that it satisfies the *dispersion relation:*

$$k^2 = \omega^2 n^2 / c^2 \qquad (1.2)$$

From (1.1) and (1.2) it is possible to re-write the refraction index in the X-ray energy region as [Attwood, 1999]:

$$n(\omega) = 1 - \frac{n_a r_e \lambda^2}{2\pi}[f_1^0(\omega) + if_2^0(\omega)] \tag{1.3}$$

where f_1^0 and f_2^0 are the real and the imaginary part of the total scattering factor for *forward scattering*, λ is the wavelength in vacuum, n_a is the average density of atoms and r_e is the classical electron radius. It is worth noting the asymptotic trend of f_1^0 and f_2^0 for $\omega \gg \omega_0$ where ω_0 represents the resonance frequencies of the atom:

$$f_1 \rightarrow Z \tag{1.4}$$

$$f_2 \rightarrow 0 \quad (f_2 \propto E^{-2}) \tag{1.5}$$

where Z is the atomic number. Usually (1.3) is re-rewritten as:

$$n(\omega) = 1 - \delta(\omega) - i\beta(\omega) \tag{1.6}$$

with

$$\delta = \frac{n_a r_e \lambda^2}{2\pi} f_1(\omega) \qquad \beta = \frac{n_a r_e \lambda^2}{2\pi} f_2(\omega). \tag{1.7}$$

From equations (1.4), (1.5) and (1.7) one can easily deduce the asymptotic trend of δ and β at high energy:

$$\delta(E) \propto \frac{1}{E^2} \qquad \beta(E) \propto \frac{1}{E^4} \tag{1.8}$$

14

In next section δ and β will be directly connected with modulus and phase of the transmission function of the sample. Here let's consider the propagation of a plane wave $\mathbf{E}_0 e^{i(\omega t - \mathbf{kr})}$ in the sample. Assuming $\mathbf{kr} = kr$ and using the dispersion relation (1.2), one has:

$$\mathbf{E}_0 e^{i(\omega t - \mathbf{kr})} = \mathbf{E}_0 e^{i[\omega t - \frac{\omega}{c}(1 - \delta - i\beta)r]} = \mathbf{E}_0 e^{i(\omega t - k_0 r)} e^{ik_0 \delta r} e^{-k_0 \beta r} \qquad (1.9)$$

where $k_0 = \omega / c = 2\pi / \lambda$ is the wave vector in vacuum. In (1.9) the first factor represents the phase advance has the wave been propagating in vacuum; the second factor containing δ represents the modified phase shift due to the interaction with the medium; the last factor containing β represents decay of the wave amplitude in the medium due essentially to the photo absorption. Hence the phase shift due to the interaction with the sample is determined by δ, while the attenuation by β. The *linear attenuation coefficient* μ is defined as the inverse of the distance into the material for which the intensity related to the wave amplitude (1.9) is diminished by a factor $1/e$:

$$\mu = \frac{4\pi}{\lambda} \beta. \qquad (1.10)$$

The absorption component β falls off very fast with respect to δ (see equations 1.8) and hence for high-energy X-rays (E $\geq$ 8keV, "hard" X-rays) δ is orders of magnitude larger than β. This is especially true for biological sample made up of light elements (see Figs. (1.1a-c)).
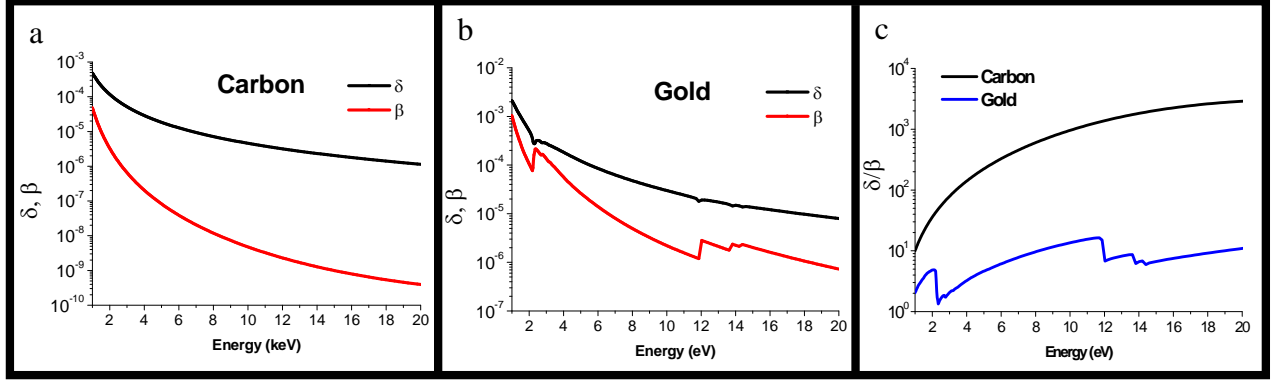
Figure 1.1: δ and β *as a function of the energy of the incoming radiation a) for Carbon, b) for Gold. c) Ratio* δ/β *as a function of the energy for both cases. In the X-ray energy range* δ *is orders of magnitude bigger than the imaginary part* β *and this is especially true for light elements.*

1.2 Transmission function

In calculating a wave front disturbed by an object we assume a linear relation like:

$$V_0 = T \cdot V_{in} \qquad (1.11)$$

Where V_{in} is the incident field on the object, V_0 the emerging field from the object and T the Transmission Function (TF) of the object. In principle TF depends not only on the sample but also on the incident field and so it cannot be considered an intrinsic property of the object. In practice we assign a TF to an object, making an error which is negligible if the TF remains constant over regions whose dimension are of the same order of the wavelength [Gori, 1995]. Moreover we assume a "thin" object in the following sense: every scatterer interacts with the incident wave, not with the scattered wave, i.e. we use the *Born approximation* and ignore

multiple scattering events: the object is sufficiently thin so that we can neglect any deviation from straight line propagation through the sample. In this case the properties of the three-dimensional diffracting sample can be treated via a simple integral along the optical axis, a projection through the object, and the TF can be written as [Born, 1987]:

$$T(\xi,\eta) = M(\xi,\eta)e^{i\varphi(\xi,\eta)} \qquad (1.12)$$

with

$$M(\xi,\eta) = \exp\left[-\frac{1}{2}\int_{object}\mu(\xi,\eta,z)dz\right] = \exp(-\mu_z) \qquad \varphi(\xi,\eta) = -\frac{2\pi}{\lambda}\int_{object}\delta(\xi,\eta,z)dz \qquad (1.13)$$

where ξ,η are the object plane coordinates and z the optical axis (see Fig.(1.2)), μ and δ are the linear attenuation coefficient and the difference from unity of the real part of the refraction index as defined in (1.6) and (1.10) respectively and μ_z is half of the projection along z of the linear attenuation coefficient. The integrals in (1.13) describe the absorption M and phase shift φ inside the sample. This approximation is known as the *projection approximation* or *thin object approximation*. It can be show that the effects of the three-dimensionality of the object can be neglected if (apart from a numerical factor) [Nugent, 2010]:

$$\tau << \frac{r_{tot}^2}{\lambda} \qquad (1.14)$$

where τ is the maximum thickness of the sample and r_{tot} the achievable resolution. Note that in the hard x-ray region ($\lambda \approx 10^{-10}$ m) with resolution of the order of 10 μm, the projection approximation is valid also for macroscopic samples. For example, for PCI mammography, if τ was of the order of compressed breast thickness ($\tau \approx 5 \times 10^{-2}$ m) and r_{tot} of the order of 10^{-5} m, the approximation is still valid [Cloetens, 1999].

There is one further approximation that is frequently adopted and which permits to obtain an analytical easy expression for the intensity on the image plane under the assumption of a weakly interacting object: *the weak object approximation*. Let's assume the thin object approximation. From (1.12) and (1.13), the TF can be written as

$$T = Me^{i\varphi} = e^{-\mu_z}e^{i\varphi} = \exp[-\mu_z + i\varphi]$$ (1.15)

If the interactions (absorption and phase shift imparted by the object) are assumed to be sufficiently weak that both term in the square bracket of the right-hand side of (1.15) may be considered small respect to one, we can Taylor expand the exponential to the first order [Pogany, 1997]:

$$T \approx 1 - \mu_z + i\varphi$$ (1.16)

Even if at hard x-ray energy absorption and phase shift are often small respect to one, (1.16) is not ever valid. A detailed theoretic study on the validity of the weak object approximation can be found in [Cloetens, 1999; De Caro, 2008] and in references therein.
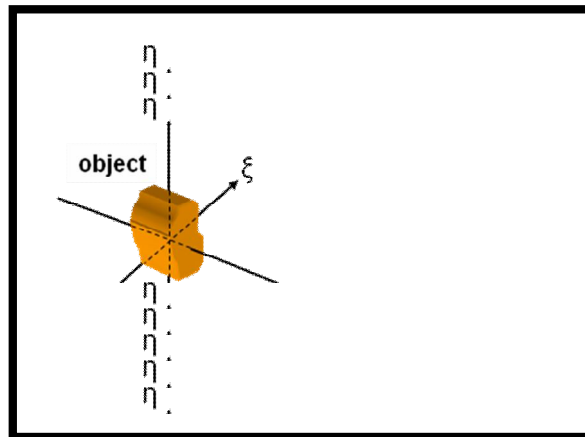
Figure 1.2: Coordinates in the object plane.

1.3 Absorption imaging and radiation dose

X-ray absorption imaging consists in detecting the photons transmitted through the investigated object. This produces a map of the linear attenuation coefficient μ (see expression 1.10), integrated along the X-ray path in the object. The number of photons N after transmission through the sample, along z, can be written as [Cloetens, 1999(2)]:

$$I(x,y) = I_0(x,y)\exp\left[-\int_{object}\mu(x,y,z)dz\right] \qquad (1.17)$$

where I and I_0 are the emerging and incident intensities, respectively. Therefore in absorption imaging one measures only the modulus of the transmission function, while the information about the phase is lost (see equations (1.12) and (1.13)). Moreover the linear attenuation coefficient μ is a rapidly decreasing function of the photon energy ($\propto 1/E^3$, see equations (1.8) and (1.10)). This fact limits the achievable contrast, especially when one wants to distinguish different kind of soft tissues (small atomic number Z). Usually to get enough contrast, one can increase the exposure time of the sample to the X-ray beam. However increasing the exposure time one will increase the *dose* absorbed by the sample. The dose is the ionizing energy deposited or absorbed per unit mass by the sample resulting in the so called *radiation damage* of the sample. Absorption leads to the breaking of chemical bounds in the sample due to the emission of photoelectrons and Auger electrons [Cazaux, 1997]: the lack of sufficient number of conducting electrons, which prevents the quick restoration of the electrical neutrality of the ionized insulating specimen, causes the radiation damage. Even if dry or frozen samples are in general more robust to radiation damage than wet samples [Lindaas, 1996] it is anyway very important minimize the absorbed dose, especially for biological sample. Many clinical situations require the revelation of contrast of different types of soft tissues. This task is generally very hard to achieve with conventional absorption

radiography, whereas the radiation dose limits the exposure time and consequently the achievable contrast that in turn will limit the resolution to several microns (20-50 µm). The absorbed dose in PCI is much smaller than the absorbed dose in absorption imaging in the hard X-rays energy range. At typical standard absorption radiography energies, the phase term is at least 10^3 times greater than the absorption one.

Basically this fact is due to the different interaction processes which lead to PCI and absorption contrast imaging, i.e. scattering and photoelectric absorption respectively. It can be shown [Jacobsen, 1990] that the ratio between the scattering cross section σ and the photoelectric cross section τ is:

$$\frac{\sigma}{\tau} = \frac{r_{tot}^2}{8} \pi \frac{r_e}{\lambda^3} \frac{\left(f_1^2 + f_2^2\right)}{f_2} \tag{1.18}$$

where r_{tot} is the resolution. In Fig. (1.3) the ratio (1.18) for Gold and Carbon as a function of the energy of the incoming X-ray beam is reported.

We can conclude that if one wants to image biological sample using hard X-rays it is more convenient to use PCI than standard absorption because PCI assures a better contrast and a lower absorbed dose.
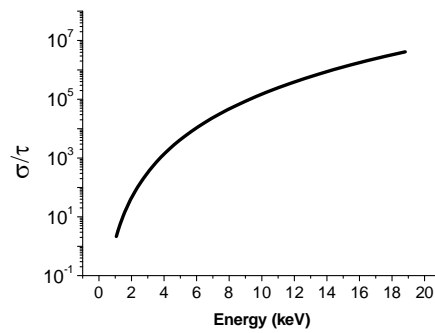
Figure 1.3: *Expression (1.18) calculated for a fixed 200 nm total resolution as a function of energy of the incoming radiation. For hard X-ray (E $\geq$ 8 keV), the scattering is more than 10^4 times more favourite respect to photo absorption.*

1.4 X-ray phase contrast imaging techniques

1.4.1 Introduction

As showed in the previous section, the sample may change the *phase* of a transmitted hard X-ray beam much more significantly than its amplitude and this is especially true for light materials. Therefore the registration of the X-ray phase shift due to the interaction with the sample, i.e. the measurement of the phase φ of the sample Transmission Function, is convenient, especially when the imaging of biological sample is realized using hard X-ray. In the last decades many PCI techniques have been successfully applied. They permit to convert the X-ray beam phase variations due to the interaction with the sample in measurable intensity modulations. Usually they can be classified into two main categories: lens-based and lens-less PCI techniques. In the first category we can mention X-ray *interferometry* and X-ray *refraction* techniques. These techniques require complicated and often expansive optical devices and the achievable resolution is limited just by the imperfections and the instability of the optics setup. The second category is the simplest and most straightforward X-ray PCI implementation, because it is based on the development of phase contrast via the free space propagation. *Propagation Phase Contrast Imaging* (PPCI) doesn't require any additional optics, leading to source-limited rather than optics-limited resolutions as we will discuss deeply in section 1.5.

1.4.2 X-ray interferometry

In X-ray interferometry, an interferometer is used to produce an interference pattern. The changes in the interference pattern induced by the sample contain quantitative information about the object phase. The principal interferometric techniques are *interferometry with crystals* and *interferometry with gratings*:

Interferometry with crystals

In X-ray interferometric imaging with crystal interferometers, the interference pattern is produced by splitting and recombining the X-ray beam using a perfect crystal. In the crystal the beam suffers three diffraction processes: the first crystal lamellae produces the splitting of the beam essentially in two beams (for simplicity we consider only the two first diffraction orders), the second splits each beams again, acting, if we consider only the two convergent beams, like a mirror, and the third one recombines the two beams giving rise to the interference pattern on the detector (see Fig. (1.4a)). Let suppose that the three diffraction processes are perfect. Therefore, if the incoming X-ray beam is perfectly coherent, the two beams on the detector are also perfectly coherent and in phase. The resulting intensity has the simple well known form:

$$I_{tot}(\mathbf{r}) = I_1(\mathbf{r}) + I_2(\mathbf{r}) + 2\sqrt{I_1(\mathbf{r})I_2(\mathbf{r})}\cos\phi(\mathbf{r}). \qquad (1.19)$$

In these hypotheses, if one inserts a phase sample (i.e. a sample which modifies only the phase of the beam) in the path of one of the two beams (see Fig. (1.4b)), the phase shift introduced by the sample, i.e. the phase of the object TF, will modify the interference pattern (1.19) in:

$$I_{tot}(\mathbf{r}) = I_1(\mathbf{r}) + I_2(\mathbf{r}) + 2\sqrt{I_1(\mathbf{r})I_2(\mathbf{r})}\cos\phi'(\mathbf{r}). \qquad (1.20)$$

Therefore in this case one can recover the object phase directly from (1.20). Note that if the absorption in the sample is not negligible, the data represented by (1.20) does not yield an unambiguous reconstruction of the phase, because a variation in the phase can produce an identical effect on the measured intensity as a variation in the amplitude. In this case, one can change the phase of one of the two beams after the first crystal lamellae in a controlled and known manner, producing a series of interferograms that are used to solve the amplitude and the phase contribution independently.

This method was proposed for the first time by Bonse and Hart in 1965 [Bonse & Hart, 1965]. Nowadays is applied especially in soft-tissue imaging for biomedical problems both for two dimensional [Hirano, 1999; Momose, 1995; Takeda, 1995; Momose, 1995(2)] and three dimensional (PCI tomography) biomedical applications [Takeda, 2000; Mizutani, 2007; Momose, 2006; Koyama, 2005; Momose, 2005; Takeda, 2000(2)].
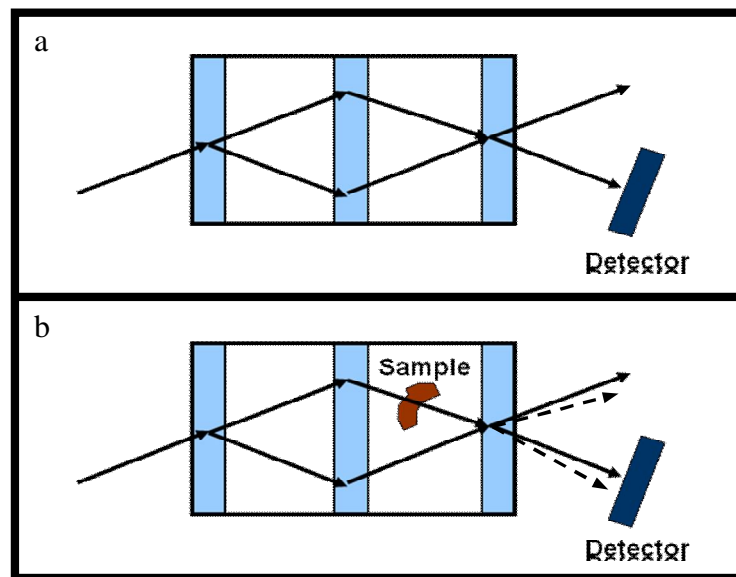
Figure 1.4: *Conceptual layout of the crystal interferometry PCI method.*

Interferometry with gratings

The gratings-based X-ray interferometer consists of a phase grating and an absorption grating (G_1 and G_2 respectively in Fig. (1.5)). Beyond the phase grating, the interference pattern arises. If we put an object before the phase grating, the refraction that occurs in the object leads to a perturbation of the incident field on the grating and a consequent local displacement of the fringes. The fundamental idea of the method is to detect the position of the fringes and

determine from this position the phase shift induced by the object [Weitkamp, 2005]. However, since the period of the phase grating does not exceed few microns (and thus the spacing of the interference fringes), the detector in the image plane will not have generally enough resolution to resolve the exact position of their maxima. In order to overcome this problem, the well know *Talbot effect* [Talbot, 1836] is exploited. Beyond the phase grating, the field profile is self-repeated, i.e. the intensity is the same, at particular distances called *Talbot distances*. Furthermore, there are some other interesting self-imaging phenomena at fractional Talbot distances [Gori, 1995]. For example, assuming an incident plane wave impinging on a phase grating with period D, phase shift π and duty factor 0.5, the self-imaging occurs at the fractional Talbot distance $z_T = (D/2)^2 / \lambda$ [Born, 1987].

For this reason an absorbing grating G_2 with absorbing lines of the same period of the fringes, is placed in the image plane just in front of the detector at a fractional Talbot distance from G_1. The fringes position is then transformed into intensity variation. It can be shown that the detected signal profile as a function of the absorption grating transversal position x (see Fig. (1.5)), contains quantitative information about the *phase gradient* of the object: the intensity in each pixel in the detector plane will oscillate as a function of the transversal position of the grating and the phase Φ of these intensity oscillations are related to the gradient of the phase shift φ by [Weitkamp, 2005]:

$$\Phi = \frac{\lambda d}{P} \frac{\partial \varphi}{\partial x} \qquad (1.21)$$

where λ is the wavelength, d the distance between the two gratings and P the period of absorption grating. The phase profile of the object can thus be retrieved from (1.21) by a simple one-dimensional integration.

Pfeiffer and colleagues have used this method both for X-rays [Kottler, 2007; Pfeiffer, 2006; David, 2007] and neutrons [Grunzweig, 2008]. Even in this case the method has been extended to the 3D tomography PCI [David, 2007; Strobl, 2008; Pfeiffer, 2007].
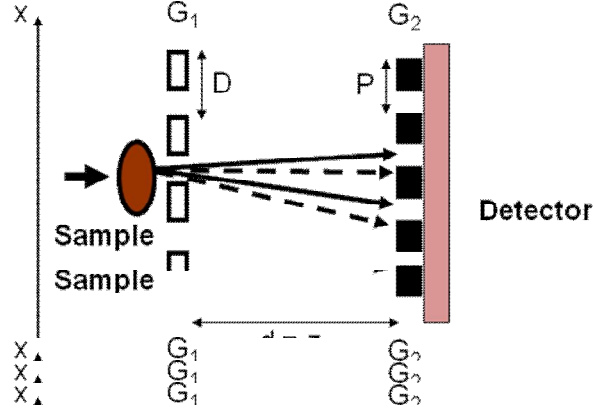
Figure 1.5*: Conceptual layout of the interferometry with gratings PCI method.*

1.4.3 X-ray refraction techniques

X-ray refraction techniques do not require the generation of interferograms to measure the object phase but are based purely on the X-ray refraction. The phase information is obtained from a direct measure of the deviation angles of the incident beam on the sample. In particular, it can be shown that the deviation angle α due to the interaction with the sample, under relaxed coherence condition, is [Wilkins, 1996]:

$$\alpha = \frac{\lambda}{2\pi}\left|\vec{\nabla}_{x,y}(\varphi)\right| = \left|\vec{\nabla}_{x,y}\left[\int_{object}\delta(x,y,z)dz\right]\right| \qquad (1.22)$$

where for the right hand side, the second of equations (1.13) is used. Depending on the way in which this deviation is measured, one can distinguish different refraction techniques:

25

Diffraction enhanced imaging

In this case the deviated beam is analyzed by a crystal (see Fig. (1.6)): only the rays which satisfy the Bragg condition of the crystal will be diffracted to the detector. Since the rocking curve of the crystal is strongly picked around few µrad, even very small X-ray deviations are converted in intensity modulations on the detector.

The idea to develop a PCI method in which a crystal is used to detect the deviation of the X-ray beam due to refraction by the object has its origin in the work of Ingal and Beliaevskaya [Ingal, 1995]. Some years later, Davis et al. [Davis, 1995] proposed a modification to this approach, and Chapman et al. [Chapman, 1997] developed yet another configuration and it is the last of these that has most promise and is now known as diffraction-enhanced imaging (DEI). Many works was produced in order to quantify the phase information obtainable from this method [Nesterets, 2006; Nesterets, 2004; Pavlov, 2004; Pagot, 2003]. The image intensity contains information about the *phase gradient* of the object. DEI is now a potentially important approach to high-sensitivity medical imaging [Arfelli, 2000; Arfelli, 2000(2); Chapman, 1997; Lewis, 2003].
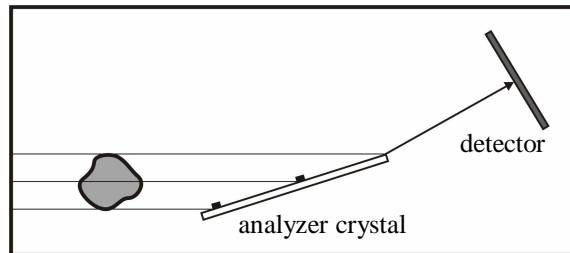
*Figure 1.6: Conceptual layout for the Diffraction Enhanced Imaging method.*

Coded aperture method

Coded aperture X-ray PCI method is a very recent refractive method similar to DEI. In this case the sensitivity to the deviation is obtained by exploiting the *edge illumination principle* [Olivo, 2011]: the discrimination of the refracted photons direction is obtained by

illuminating only the edge of the detector pixels instead of using an analyzer crystal. The principle is illustrated in Fig. (1.7) for a single pixel: a thin individual beam straddling the edge between two pixels. Photons deviated due to refraction in the sample, which is scanned in the beam, can change their status from undetected to detected.

The so called *coded aperture setup* allow repeating the process described above for every detector row (or column) of a 2D detector illuminated by a divergent, polychromatic beam. The use of a 2D detector makes sample scanning unnecessary. The coded aperture setup consists of two misaligned gratings which allow the illumination only for a small portion of each pixel of the detector. The remaining part of each pixel is not illuminated: it is the misalignment between the masks that permit the angular sensitivity. The method is discussed in details in [Olivo, 2007]. An application example in security inspections is proposed in [Olivo, 2011].
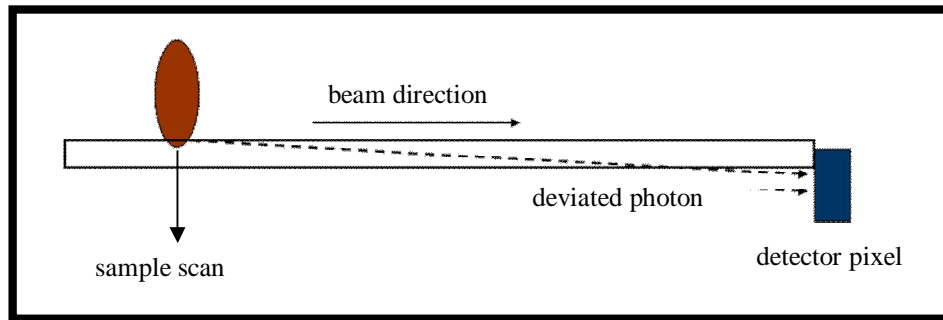
Figure 1.7: Conceptual layout of the edge illumination principle.

1.4.4 X-ray propagation Phase Contrast Imaging applications

This technique, which is the PCI method used in the framework of this thesis, will be described in details in the next section. Let's here just a brief report of some interesting application examples. One of the first examples of the power of the method arose from the work of Spanne *et al.* [Spanne, 1999], who showed phase contrast of an artery specimen and discussed the potential for phase contrast in medical imaging. A three-dimensional analysis of

bone structures is reported in [Salome, 1999]. Work by Arfelli and colleagues [Olivo, 2001; Arfelli, 2000] have demonstrated the applicability of PPCI to mammography. Many biological applications have been successfully realized [Hopper, 2009; Thurner, 2003; Jheon, 2006; Zabler, 2006; Rau, 2006]. Even in this case the 3D tomography extension has been realized, both for material and medical samples [Cloetens, 1997; Spanne, 1999; Salome, 1999]. PPCI was also realized using laboratory sources [Mayo, 2003]. Other interesting applications have been reported in palaeontology [Tafforeau, 2008; Lak, 2008; Perrichot, 2008; Tafforeau, 2006]. Recently, Salditt and collaborators used x-ray waveguides as highly confining optical elements in order to realize PPCI experiments on unstained biological cells with nano-scale resolution [Giewekemeyer, 2011].
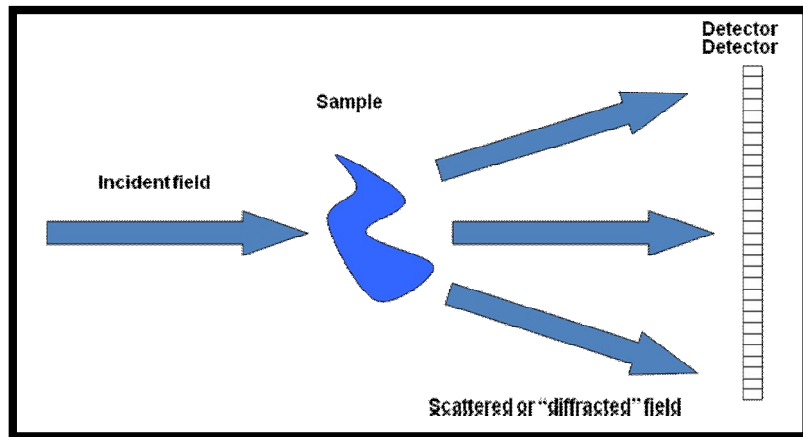
Figure 1.8: Conceptual layout of the Propagation based PCI method.

1.5 Propagation Phase Contrast Imaging

1.5.1 Theoretical basis

The conceptual layout of the experimental setup which corresponds to PPCI is reported in Fig. (1.8). Information about the sample is extracted from the measured intensity distribution on the detector given by the square modulus of the scattered or "diffracted" field. In this section the mathematical basis and the fundamental concepts necessary to understand how

propagation can transform phase modulations due to the interaction with the sample to detectable intensity variations, are described. It can be shown that the effect of the propagation from one plane to another plane on the optical axis z can be expressed by the convolution of the emerging field from the object (1.11) and a *propagator*, i.e. the relation between the emerging field V_0 on the object plane and the field V_z on a generic plane z is [Gori,1995]:

$$V_z(x,y) = \iint_\infty V_0(\xi,\eta)P_z(x-\xi, y-\eta)d\xi d\eta = V_0 \otimes P_z \qquad (1.23)$$

where ξ, η are the object plane coordinates, x, y the z plane coordinates and the symbol $\otimes$ indicates the convolution. Note that using the *convolution theorem*, we can re-write (1.23) in Fourier space as a simple product:

$$\tilde{V}_z = \tilde{P}_z \cdot \tilde{V}_0. \qquad (1.24)$$

where the tilde indicates the Fourier Transform (FT).

If one adopts the *Fresnel approximation* the propagator can be written as [Gori, 1995]:

$$P_z(x-\xi, y-\eta) \equiv \frac{ie^{-ikz}}{\lambda z}\exp[-ik\frac{(x-\xi)^2+(y-\eta)^2}{2z}]. \qquad (1.25)$$

where λ is the radiation wavelength and $k = 2\pi/\lambda$ the corresponding wave vector. Notice that the phase factor exp(-ikz) does not affect the intensity and for simplicity it is often dropped from the expression of the propagator. The effectively Fresnel propagator in Fourier space is given by

$$\tilde{P}_z(p,q) = \exp[i\pi\lambda z(p^2+q^2)]. \qquad (1.26)$$

where p and q are the *spatial frequencies*:

$$p = \frac{k_x}{2\pi} \qquad q = \frac{k_y}{2\pi} \qquad (1.27)$$

The conditions of validity of (1.25) i.e. the Fresnel approximation, are discussed in many text books and papers (see for example [Gori, 1995; Nugent, 2010]). It remains valid in the cases facet experimentally in this thesis work.

It is easy to show that the diffracted field in Fresnel approximation has approximately the same transversal dimension of the sample [Gori, 1995]. For this reason the Fresnel approximation is often called *paraxial approximation*.

Expanding the quadratic terms in (1.25) and taking constants out of the integration, (1.23) can be re-written as [Lindaas, 1994]:

$$V_z(x,y) = \frac{i e^{-ikz}}{\lambda z} \exp[-\frac{ik(x^2+y^2)}{2z}] \iint_{\infty} V_0(\xi,\eta) e^{-i\frac{k}{2z}(\xi^2+\eta^2)} e^{\frac{ik}{z}(x\xi+y\eta)} d\xi d\eta. \qquad (1.28)$$

The first exponential in the integral is a quadratic phase function. If:

$$z \gg \frac{\pi(\xi^2+\eta^2)_{max}}{\lambda}, \qquad (1.29)$$

the quadratic phase function can be set to unity and we obtain the *Fraunhofer approximation* or *far field approximation* for V_z:

$$V_z(x,y) = \frac{i e^{-i[kz+\frac{k}{2z}(x^2+y^2)]}}{\lambda z} \iint_{\infty} V_0(\xi,\eta) e^{\frac{2\pi i}{\lambda z}[x\xi+y\eta]} d\xi d\eta \qquad (1.30)$$

It is an approximate spherical wave (the factor before the integral) modulated by the FT of V_0 calculated in $(x/\lambda z, y/\lambda z)$. Unlike the Fresnel field (i.e. (1.23) with (1.25)), the Fraunhofer field (1.30) increases its transversal dimensions linearly with the propagation distance z. This starts to happen when z reaches a transition value defined by the so called *Fresnel distance*:

$$D_F = \frac{d^2}{\lambda} \qquad (1.31)$$

where d is the typical object dimension.

Consider now the case of a divergent field impinging on the sample produced by a point source. In order to treat these cases it is common to introduce an effective propagation distance called *defocusing distance*, defined as:

$$D = \frac{z_1 z_2}{z_1 + z_2}. \qquad (1.32)$$

where z_1 and z_2 are respectively the source-object planes distance and the object-image planes distance, as shown in Fig. (1.9a). Moreover the divergence of the field produces an enlargement of the object on the image plane which is possible to quantify introducing the *geometrical magnification*, defined as the ratio between the enlarged dimension of the object I on the image plane and the original dimension ι on the object plane:

$$M = \frac{I}{\iota} \qquad (1.33)$$

It is easy to show from geometrical consideration (see Fig. (1.9b)) that:

$$M = \frac{z_1 + z_2}{z_1}. \qquad (1.34)$$

31

It is worth to noting that if $z_1 \gg z_2$, we recover the case of a plane wave, with $D \approx z_2$ and $M \approx 1$, while if $z_1 \ll z_2$, we have $D \approx z_1$ and $M \approx z_2/z_1 \gg 1$.

Moreover it was shown [Pogany, 1997] that the formalism for a plane wave illumination is still valid by substituting $z \rightarrow D$ and $(x,y) \rightarrow (x/M, y/M)$.
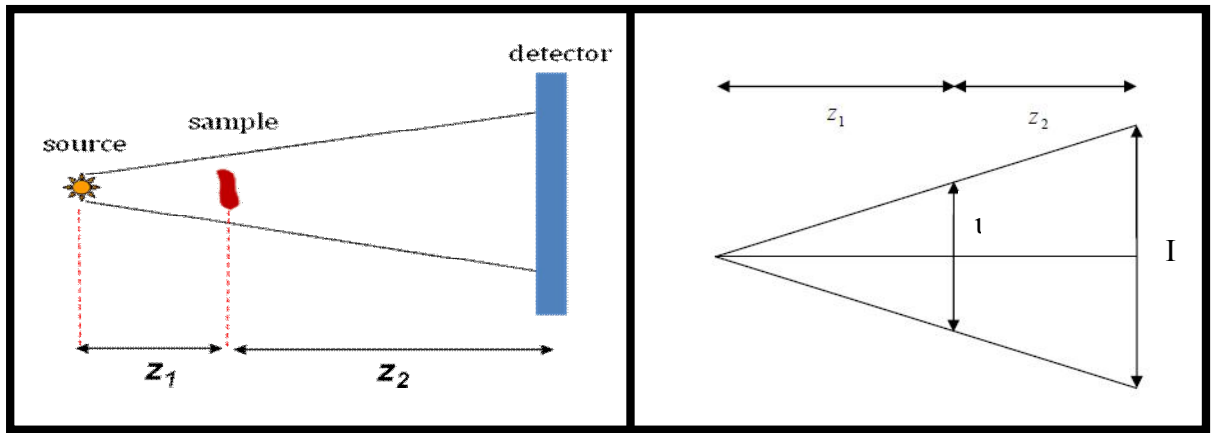
Figure 1.9: *Point source illumination case. a) significant distances: source- sample distance z_1 and sample detector distance z_2. b) Geometrical representation of the Magnification.*

1.5.2 Contrast Transfer Function

Consider now an incident plane wave of unit amplitude ($V_{in} = 1$) on a weak and thin object for which the approximation (1.16) for the transmission function is valid. For any position along the optical axis z, the field amplitude in the Fourier space can be calculated using (1.24) with $\tilde{V}_0 = \tilde{T}$:

$$\tilde{V}_z = \tilde{P}_z \cdot \tilde{T}. \qquad (1.35)$$

Using (1.16) in calculating $\tilde{T}$ and the expression (1.26) with q=0 (one-dimensional case) for $\tilde{P}_z$, one finds

$$\tilde{V}_z = e^{i\chi}(\delta + i\tilde{\varphi} - \tilde{\mu}_z)$$ (1.36)

where $\chi = \pi\lambda z p^2$. Moreover the tilde indicates the Fourier Transform (FT) and δ is the Dirac delta function. Therefore the field in the Fourier space becomes

$$\tilde{V}_z = (\delta - \tilde{\mu}_z \cos\chi - \tilde{\varphi}\sin\chi) + i(\tilde{\varphi}\cos\chi - \tilde{\mu}_z \sin\chi)$$ (1.37)

coming back in the real space by the inverse FT:

$$V_z = (1 - \mu_z \widetilde{\cos}\chi - \varphi\widetilde{\sin}\chi) + i(\varphi\widetilde{\cos}\chi - \mu_z \widetilde{\sin}\chi)$$ (1.38)

Therefore the intensity, by retaining only first order terms in φ and μ_z is:

$$I_z = |V_z|^2 \approx 1 - 2\mu_z \widetilde{\cos}\chi - 2\varphi\widetilde{\sin}\chi$$ (1.39)

Finally, by the use of another FT, the intensity in the Fourier space is [Pogany, 1997]:

$$\tilde{I}_z \approx \delta - 2\tilde{\mu}_z \cos\chi - 2\tilde{\varphi}\sin\chi$$ (1.40)

The first term (Dirac delta function) corresponds to a homogeneous background in the image due to the direct, non-interacting beam. The terms and $\sin\chi$ and $\cos\chi$ are called *phase* and *amplitude contrast transfer function* (CTF). Their behaviour versus the normalized frequency $\sqrt{\lambda z}\,p$ is plotted in Fig. (1.10). It is evident that after the propagation in the free space, the phase modulations due to the interaction with the object are transferred into detectable

33

intensity modulation. In what follows the defocusing distance (1.32) is used instead of z, since it gives a more general point of view.
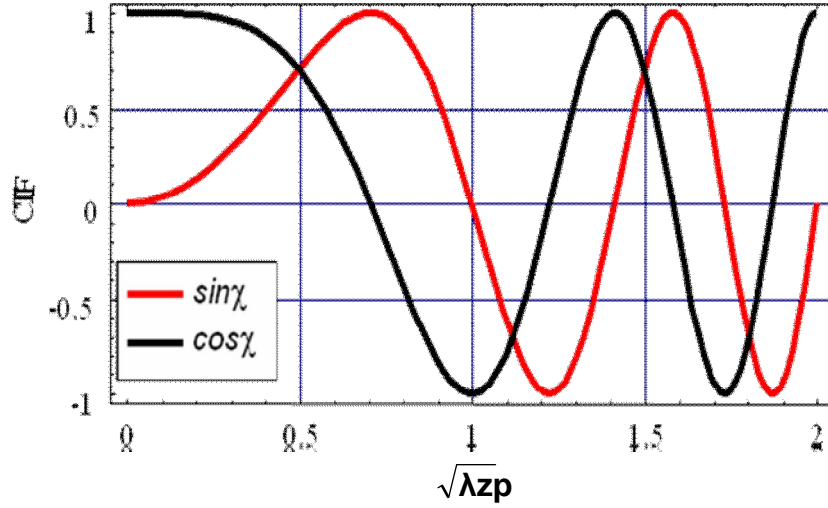
Figure 1.10: Phase (red line) and amplitude (black line) contrast transfer function as a function of the normalized frequency $\sqrt{\lambda z}\, p$.

1.5.3 Regions of image formation

Different regimes of imaging can be exploited as a function of the defocusing distance and the object size. They can be roughly discriminated comparing the defocusing distance (1.32) with the Fresnel distance (1.31). To do this, is usual to introduce the *Fresnel number*:

$$N_F = \frac{D_F}{D} \tag{1.41}$$

*Absorptio*n: In this case $D=0$ and $I_{D=0}=1-2\mu_z$. Using the definition of μ_z in (1.13) it is easy to receive equation (1.17), i.e. the intensity in absorption imaging.

Near field regime: In this case $D << D_F$ ($N_F >> 1$) and the intensity in the real space can be calculated as [Cowley,1995]:

$$I(x) = I_{abs}(x)\left[1+\frac{\lambda D}{2\pi}\Delta(\varphi(x))\right] \qquad (1.42)$$

It describes an absorption image (first term) with an additional contribution from the Laplacian of the object phase distribution, i.e. to the second derivate of phase shift. In practise the contrast arises as an *edge-enhancement* image in which the sharp edges of the object appears as characteristic black-white fringes. This regime allows to direct measure the geometrical features of the sample because only its edges, where the real part of the refraction index varies fast, posses a good contrast. Therefore a reconstruction of the object transmission function (see for example [Khon, 1997; Nugent, 1996]) is possible but not necessary. Therefore this regime permits an immediate imaging of samples which do not display sufficient contrast using standard absorption radiology technique. This feature makes it particular appealing for medical diagnosis application. Some other features of (1.42) may be noted [Pogany, 1997]:

1- The contrast in the image increases with D
2- The geometric features of the contrast are wavelength independent, λ appears only as a separable factor.
3- The defocusing does not affect the absorption image [cloetens 1997].

Holographic regime If the defocusing distance increases further, the intensity distribution tends to lose resemblance with the original object and usually the corresponding intensity

distribution is called hologram. The resemblance with the real object shape is more and more weak and hence unlike the previous situation, the amplitude and the phase of the object transmission function has to be necessarily reconstructed using a suitable algorithm. If $D \approx D_F$ ($N_F \approx 1$), one speaks of *Fresnel regime* and the field is given by (1.23) with the propagator given by (1.25) while if $D >> D_F$ ($N_F << 1$), one speaks of *Fraunhofer regime* or *far field regime* and field is given by (1.30).

Further details about holography will be reported in Chapter 5 where examples of holography reconstructions will be proposed.

Here, for the sake of completeness, it is important to mention that if one looks at the fringes *outside* the illumination cone of the impinging beam on the sample in the *far field* regime, one usually speaks of *diffraction*. If one considers non periodic object (for periodic object one has the well know Bragg-diffraction), one has the methodology called *Coherent Diffraction Imaging*, which is a particular lens less technique whose resolution can approach in principle the diffraction limit [Sayre, 1952; Miao, 1999; Robinson, 2001] and which has an enormous potentiality if used with the complete coherent beam produced by the next generation synchrotron source (free electron laser). For a complete description of X-ray CDI see [Chapman, 2006]. In Figs. (1.11) the simulated image for the same object (a Kevlar fibre) in the three different imaging situations described above are reported with the corresponding intensity profile.
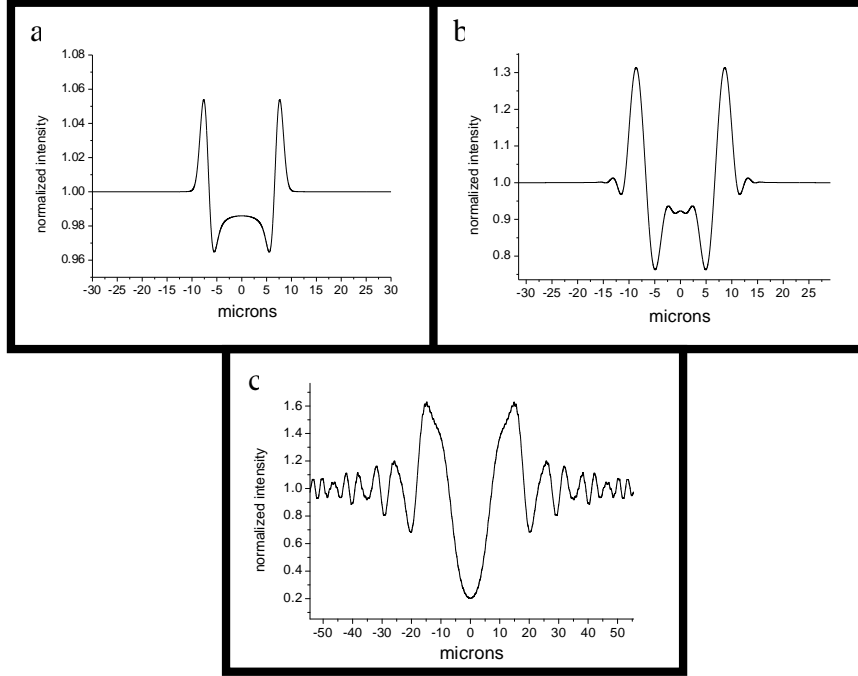
Figure 1.11: Simulated intensity distribution from a Kevlar fibre in three different imaging situations: a) near field regime b) Fresnel regime c) Fraunhofer regime. In a) the effect of phase is present only at the edge of the fibre (edge enhancement effect). In a) and b) the simulated resolution is the same (∼ 0.5 μm) and the same amount of information is in principle present in the two images. In c) the simulated resolution is 50 nm. For a complete description of the used simulation program see section 1.5.6.

1.5.4 Coherence

Coherence in X-ray imaging is a very important concept because the coherence properties of the X-ray beam impinging on the sample can strongly affect the intensity on the detector plane. Till now, we regarded the X-ray beam as a fully coherent wave field, i.e. we assumed constant phase differences of all partial waves during the time of measurement. In practice, we have implicitly assumed that knowing the field at one point in the space and at one instant in time we could know the field everywhere and at anytime. This is only true for an ideal

monochromatic point source. However for real X-ray sources, from standard X-ray tubes to third generation synchrotron radiation, spectral bandwidth and the finite spatial dimension of the source cannot be neglected. Mathematically, one utilizes the *Mutual Coherence Function* (MCF)

$$\Gamma(\mathbf{r}_1,\mathbf{r}_2,\tau) = \langle U(\mathbf{r}_1,t)U^*(\mathbf{r}_2,t+\tau)\rangle, \qquad (1.43)$$

and its normalized version, called *complex degree of coherence*:

$$\gamma(\mathbf{r}_1,\mathbf{r}_2,\tau) = \frac{\Gamma(\mathbf{r}_1,\mathbf{r}_2,\tau)}{\sqrt{\langle I(\mathbf{r}_1,t)\rangle\langle I(\mathbf{r}_2,t)\rangle}} \qquad (1.44)$$

In (1.43) and (1.44) $\mathbf{r}$ denotes the position in space, t is time and $\langle\ \rangle$ indicates an *ensemble* average over many realizations of the random process [Nugent, 2010]. Phenomenological the degree of coherence of a field corresponds to the ability of the field to form interference patterns in a two pinhole Young experiment, where the interference term of the time averaged intensity at a point P on the detector plane is proportional to the modulus of (1.44) [Reynolds, 1989]:

$$I(P) = I_1 + I_2 + 2\sqrt{I_1 I_2}|\gamma|\cos(\arg\gamma + \frac{2\pi}{\lambda}d) \qquad (1.45)$$

with $I_i = \langle I(\mathbf{r}_i,t)\rangle$, $\mathbf{r}_i$ positions of pinholes, τ time delay between the arrival of the light from the two pinholes to the detector and $d = |\mathbf{r}_1 - \mathbf{r}_2|$. The *fringes visibility*,

$$V = \frac{I_{\max} - I_{\min}}{I_{\max} + I_{\min}} \qquad (1.46)$$

where $I_{\max}$ and $I_{\min}$ are the maximal and minimal intensities of two neighbouring fringes in the interference pattern, can also be expressed as $V = |\gamma_{12}|$ [Gori, 1995].

In order to quantify the volume in which one can consider the field sufficiently correlated with itself, i.e. where one has well definite phase relationships between field amplitudes, the coherence lengths are introduced. In the case of relatively narrow bandwidth fields ($\tau \ll \frac{1}{\Delta\omega}$, [Gori, 1995]), the so called quasi monochromatic approximation for the MCF can be used:

$$\Gamma(\mathbf{r}_1, \mathbf{r}_2, \tau) \approx J(\mathbf{r}_1, \mathbf{r}_2) \exp(-i\omega_0 \tau) \qquad (1.47)$$

where ω_0 is the central angular frequency and $J(\mathbf{r}_1, \mathbf{r}_2)$ is called *Mutual Intensity* (MI). It is evident that in this case the coherence properties are determined by the spatial part of Γ, i.e. just by the MI. If it is assumed that the complex degree of coherence (1.44), for a quasi monochromatic source has a gaussian function of the form

$$\gamma(\mathbf{r}_1 - \mathbf{r}_2) = \exp\left[-\frac{|\mathbf{r}_1 - \mathbf{r}_2|^2}{l_c^2} \right] \qquad (1.48)$$

then we use this as the implicit definition of the *spatial coherence length* l_c [Nugent, 2010]. Therefore the coherence length characterizes the *separation* of the points at which the correlations have dropped to a value of e^{-1}. Sometimes the half-width at half-maximum is used, l_c^{HW}. In this case,

$$l_c^{HW} = l_c \sqrt{\ln 2} \approx 0.83 l_c. \qquad (1.49)$$

Using l_c or equivalently l_c^{HW}, we can introduce a characteristic coherence area A_c:

$$A_c = l_c^2 \qquad (1.50)$$

It measures the area in the transversal direction into which the field is correlated with itself. The concept of longitudinal coherence can be introduced adopting a definition that is consistent with the definition for spatial coherence. Let suppose we have a field that has a Gaussian distribution of power

$$S(\omega) = \exp\left[-\frac{\ln(2)}{4} \frac{(\omega - \omega_0)^2}{\Delta\omega^2} \right] \qquad (1.51)$$

so that in this case $\Delta\omega$ is FWHM of the frequency distribution. The temporal coherence length may be obtained by taking the FT of this, so that the temporal coherence function has the form

$$\gamma(\tau) = \exp(-i\omega_0\tau) \exp\left[-\frac{\Delta\omega^2}{\ln(2)} \tau^2 \right] \qquad (1.52)$$

and the corresponding coherence length, then , is given by

$$l_c^{long} = c\frac{\sqrt{\ln 2}}{\Delta\omega} = \frac{\sqrt{\ln 2}}{2\pi} \frac{\lambda^2}{\Delta\lambda} \qquad (1.53)$$

where c is the speed of light. The product

$$V_c = l_c^{long} \cdot A_c \qquad (1.54)$$

is the *coherence volume* of the radiation field, often called a *mode* of the field. Inside a mode the field maintains a well defined phase.

The process of propagating the MI function from an *incoherent* source in the plane π_1 to the plane of interest π_2 is described by the Van Cittert-Zernike theorem. This theorem states that the MI generated on the plane π_2 (coordinates x, y) by the source lying on the plane π_1 (coordinates ξ, η) is given by [Gori, 1995]:

$$J(Q_1, Q_2) = \frac{e^{-\frac{ik}{2z}\left[\left(x_1^2 + y_1^2\right) - \left(x_2^2 + y_2^2\right)\right]}}{z^2} \int_\pi I_0(\xi, \eta) e^{i\frac{k}{z}\left[(x_1 - x_2)\xi + (y_1 - y_2)\eta\right]} d\xi d\eta \qquad (1.55)$$

where $I_0(\xi, \eta)$ is the intensity distribution on the source plane and the MI function corresponding to the completely incoherent source is (see Fig.(1.12))

$$J(S_1, S_2) = I_0(S_1)\delta(S_1 - S_2) \qquad (1.56)$$
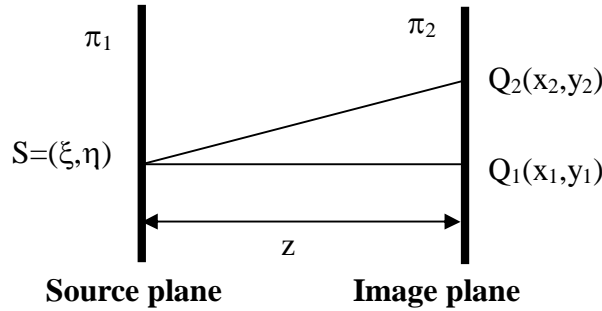
Figure 1.12: Coordinates for the van Cittert-Zernicke theorem (1.55)

Equation (1.55) states that the mutual intensity arising from a primary incoherent source is proportional to the Fourier transform of the intensity distribution of the source itself. This result has an enormous importance because it explains how the radiation field from a primary incoherent source gains coherence during the propagation. Even if the source had the form

41

(1.56) on the source plane, $J(Q_1, Q_2)$ with Q_1 and Q_2 on the plane π_2 would be different from a δ Dirac function $J(Q_1, Q_2) \neq I(Q_1)\delta(Q_1 - Q_2)$ (except for the case of an infinite and uniform source distribution $I_0(S_1)$=constant). This means that the source on π_2 has acquired a certain degree of coherence. In particular [Attwood, 1999], if one chooses for the source intensity distribution $I_0(S_1)$ a Gaussian function with Full Width at Half Maximum (FWHM) s, apart for a phase factor the integral (1.55) gives another Gaussian with coherence length

$$l_c = \frac{\lambda z}{s}, \tag{1.57}$$

apart numerical factors which depend on the exact way in which one defines the gaussian distribution $I_0(S_1)$ and the coherence length (look at equations 1.48 and 1.49). It is important to stress that the definition (1.57) for the coherence length is strictly valid assuming a completely incoherent source and a Gaussian shape for the MI function.

The correspondent coherence area (1.50) is

$$A_c = l_c^2 \propto \left(\frac{\lambda z}{s}\right)^2 = \frac{\lambda^2 z^2}{A} \tag{1.58}$$

where $A = s^2$. It is worth to note that the larger is the distance z, the larger is the coherence length and, due to the Fourier transform properties, the smaller is the source size, the higher is the coherence length. From (1.53) and (1.58) it is possible to calculate the coherence volume:

$$V_c = l_c^{long} \cdot A_c \cong \left(\frac{1}{\Delta\Omega}\right)\left(\frac{\lambda}{\Delta\lambda}\right)\lambda^3 \tag{1.59}$$

where $\Delta\Omega = A/z^2$ is the solid angle subtended by the source area A at the point P. For sake of completeness it is important to remember that the van Cittert-Zernicke theorem can be used to derive the MI $J(Q_1, Q_2)$ in the image plane also in the case of an non-gaussian function.

Moreover if one has an object located in a plane intermediate between the source and image planes (see Fig.(1.13)).

π_1 σ π_2

$S=(\xi,\eta)$ $R=(x_0,y_0)$ $Q(x,y)$

Source plane   **Object plane**   **Image plane**
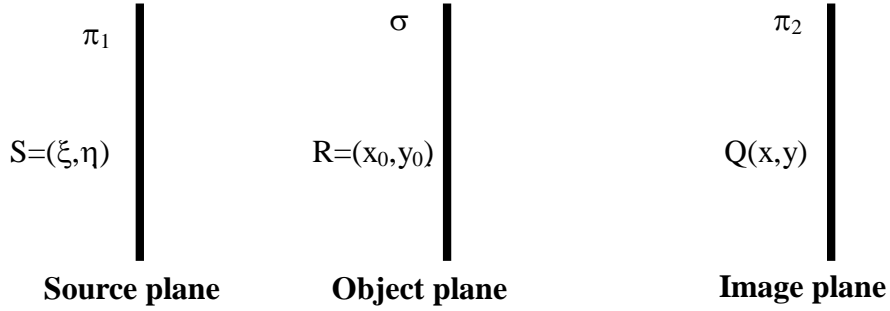
Figure 1.13: *Coordinate of points of the source plane, object plane and image plane following the notation used in the text.*

If the transmission function of the object is T(x,y), one can demonstrate that [Reynolds, 1989]:

$$J(Q_1,Q_2) = \iint J(R_1,R_2) \cdot T(R_1) T^*(R_2) \cdot P_D(Q_1 - R_1) P_D^*(Q_2 - R_2) dR_1 dR_2 \qquad (1.60)$$

where $J(R_1,R_2)$ is the mutual intensity function (as given by (1.55)) obtained by the propagation from the source to the object plane. R_1 and R_2 are two generic points on this latter plane and P_D is the propagator of the system from the object to the image plane.

1.5.5 Spatial resolution and coherence requirements

The intensity distribution for the case of partially transverse coherence on the object plane is most easily obtained by calculating the coherent intensity contribution of every point of the source independently and integrates over the source intensity [Goodman, 1988]. It can be shown that mathematically, this corresponds to a convolution between the *coherent* intensity (1.39) with the *projected* source intensity distribution S on the detector plane:

$$I_D^{tot} = I_D^{coh} \otimes S \qquad (1.61)$$

In the Fourier space one has a simple product:

$$\widetilde{I}_D^{tot} = \widetilde{I}_D^{coh} \cdot \widetilde{S} \qquad (1.62)$$

In practise, the finite size of the source produces a blurring in the image which is very well modelled by the convolution (1.61). The net effect of this convolution is a damping of the CTFs oscillation for high spatial frequencies and $\widetilde{S}$ is often called *damping factor*. An example is reported in Fig. (1.14).

The resolution turns to be limited to a value correspondent to the highest spatial frequency still in contrast. Therefore, according to [Pogany, 1997], a rough estimation of the resolution will correspond to an estimation of the damping factor width and hence of the intensity distribution width S. Assuming for S a Gaussian shape, the following expression was calculated:

$$r_s = s \frac{z_2}{z_1 + z_2} \qquad (1.63)$$

$$\sqrt{\lambda z}\, p$$
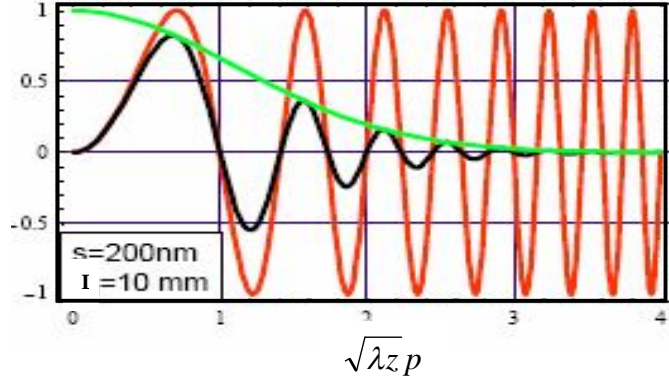
Figure 1.14: The phase CTF (red line) is damped down by the damping factor $\tilde{S}$ (green line). The effective phase CTF (black line) is different from zero only in a finite range of spatial frequency.

where s is the FWHM of the source intensity distribution and expression (1.63) is the projection of s on the detector plane reduced by the magnification. Naturally in calculating the total resolution the finite *Point Spread Function* (PSF) of the detector must be considered. It can be done with another convolution:

$$I_D^{tot} = I_D^{coh} \otimes S \otimes PSF \tag{1.64}$$

Therefore the total damping factor is the Fourier Transform of the convolution between S and the PSF of the detector. If one assumes a Gaussian shape for both of them the convolution will be again a Gauss function with FWHM given by the root mean square of the two FWHM of S and PSF:

$$r_{tot} = \sqrt{\left(s\frac{z_2}{z_1 + z_2}\right)^2 + \left(\frac{PSF}{M}\right)^2} \tag{1.65}$$

45

Note that also the detector PSF was scaled for the magnification M. This is the peculiarity of the *projection microscopy*. If s<<PSF it is convenient to decrease the detector resolution by properly increasing the magnification. In this case the source contribution, if M>>1 (i.e. z_1<<z_2) tends to the source size that is the fundamental limiting factor for projection microscopy. On the other hand if s>>PSF it is convenient to choose z_1>>z_2 (M≈1) to pull down the source contribution. In any case the lower limit for the resolution corresponds to the relevant *numerical aperture* of the optical system [Gori, 1995]. For the waveguide based microscope described in Chapter 4 which is the projection phase contrast microscope used in this thesis, the lower limit for the resolution will be explicitly calculated. For the sake of completeness, in general one should take into account the longitudinal coherence contribution. It can be taken into account introducing a slightly larger effective source size [De Caro, 2008]:

$$s_{\Delta\lambda} = \sqrt{s^2 + \frac{z_1 \Delta\lambda}{\pi^2 \ln 2}} \qquad (1.66)$$

It is worth noting that the chromatic contribution for small defocusing distance D<<D_F is ever negligible, even in the case of a polychromatic source ($\Delta\lambda \approx \lambda$). When weak defocusing condition are not satisfied it can be shown that in the spatial frequency band up to $1/\sqrt{2D\lambda}$ (D ≈ ½D_F) a wavelength spread $\Delta\lambda/\lambda = 10^{-1}$ does not have any practical effect. For bigger defocusing distance, i.e. in holography regime, in general the chromatic contribution could be important and the requirements on the longitudinal coherence become more stringent.

It is worth noting that this simple model is strictly valid for the case of a complete incoherent source of Gaussian shape with FWHM s. As described in Chapter 2 the WG beam has intrinsically a certain degree of coherence, i.e. in principle the points of the source cannot be treated independently and hence expression (1.63) is not strictly valid but represents an upper limit for the contribution of the source in the case of the WG. Nevertheless the formalism continues to reproduces the experimental results if an effective value for s is chosen in order to reproduce the actual coherence length of the beam on the sample.

1.5.6 Simulation program for the direct problem

The analysis of the interference pattern recorded with the WG based propagation phase contrast microscope described in chapter 4 has been made comparing the experimental profiles with theoretical simulations. Exploiting the mathematical formalism discussed above a program realised with Matlab was used to calculate the theoretical profiles. In Fig.(1.15) the different steps of the program are illustrated. The program consists of a main program (boxes 1,2,3,4) where the main calculations are performed. In the first part of the main program (step 1) all the input parameters, like the incident wavelength λ, the length scale l of the object needed for the normalisation, the number n of intervals in which the x-coordinate is divided, the centre and the limits of the sampled window, and the defocusing distance D are defined.

The range of the spatial coordinate x in the real space and f in the reciprocal space is also defined. As a second step of the main program the object is introduced by calling a subprogram where the Fourier transform of the transmission function of the specific sample (step 2a) and the free space propagator in the reciprocal space (step 2b) are defined. Here the wavelength and the defocusing distance D are used. Finally at the step 2 the coherent field at D is calculated in the Fourier space representation. In this space the transmission function T and the propagator are simply multiplied (equation (1.35)) and their product is then transformed back to the real space. Finally in the step 3 the coherent intensity is calculated from the product of the field with its complex conjugate. To include the effect of the finite resolution the model described in section 1.5.5 is applied: the program proceeds to step 4 where (step 4a) the total damping factor J_0 is defined as the Fourier Transform of a Gaussian function of FWHM r_{tot} (equation 1.65) and finally the intensity on the detector plane (equation (1.64)) is calculated as the Inverse Fourier Transform of the product between the total damping factor and the Fourier Transform of the coherent intensity.

1   **Definition of input parameters**

2a   **Object= FT($T(\xi,\eta)$)**

2b   Propagator= $\tilde{P}_z(p,q)=\exp[i\pi(D\lambda/l)p^2]$

2   **Field=IFT(object·propagator)**

3   **Intensity=(Field·conj(Field))**

CORRECTION FOR FINITE RESOLUTION

4a   **J₀=FT(S⊗PSF)**

4   **I$_{detector}$=IFT[FT(Intensity) ·J$_0$]**
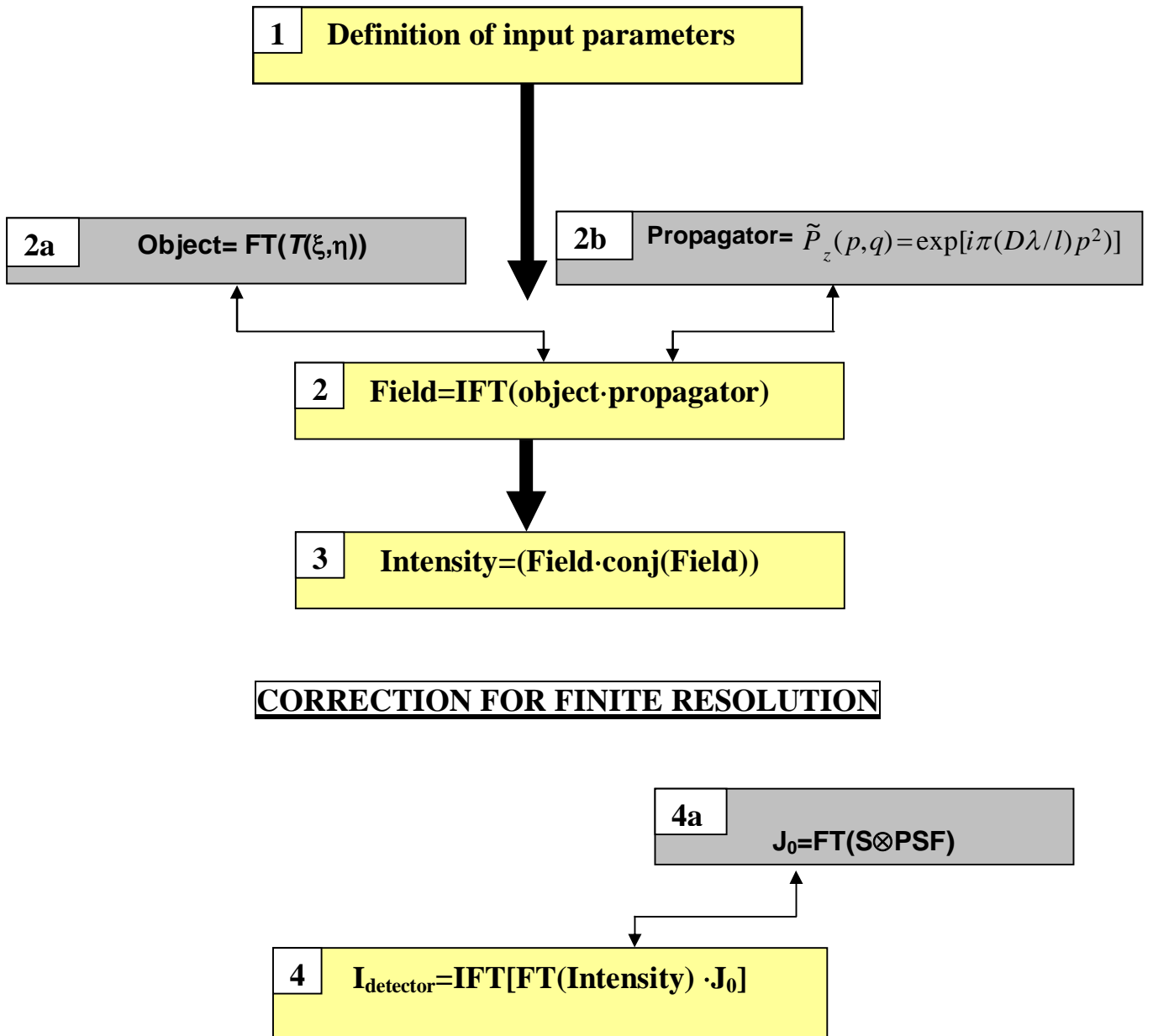
Figure 1.15: Scheme of the simulation program used to calculate the theoretical interference pattern produced by the samples analysed. The different steps are described in the text and the various notations are explained.

2. X-ray waveguide basic theory

Planar and 2D X-ray waveguides (WG) are optical elements of considerable interest both from a fundamental point of view and for their use in microprobe experiments (i.e. micro imaging, micro diffraction, micro fluorescence, etc.). After the first demonstration of the feasibility to provide a sub micrometer beam with planar WG [Feng, 1995; Lagomarsino, 1996] and with 2D WG [Pfeifer, 2002], many different schemes and many applications have been demonstrated. Further investigations of X-ray waveguides are particularly important as they have a prominent position in the recently started discussion of the smallest possible X-ray spots. In fact first Bergemann et al. [Bergemann, 2003] argued that single mode X-ray waveguides provides the smallest X-ray spots with dimensions of around 10 nm. Interestingly Pfeiffer et al. [Pfeiffer, 1999] and Salditt et all. [Salditt, 2008] produced already a one-dimensional waveguide that was operated almost at this limit.

The out coming beam, diffracted at the WG exit, can be exploited for high-resolution X-ray microscopy and micro diffraction imaging [Lagomarsino, 1997; Di Fonzo, 2000] and in coherent X-ray diffraction imaging (CXDI) experiments [De Caro, 2007; De Caro, 2008(2)]. For X-ray microscopy, the nanosized channel is used as a secondary source to magnify an object onto a detector screen, with an attainable resolution limited only by the actual size of the WG channel. On the other hand, with the CXDI technique [Miao, 2002], resolution increase has been demonstrated, in principle bounded only by the fundamental diffraction limit. The degree of coherence of the incident wave is extremely important factor to consider in CXDI experiments. In practice, in most of the experiments, the beam that arrives onto the sample has encountered several optical elements on its path from the source, e.g., monochromators, mirrors, slits, etc.. This leads to a coherence degradation at the sample position. This lack of coherence can severely disturb the convergence of the phase reconstruction process, as recently discussed by Williams *et al.* [Williams, 2007]. In this respect, a waveguide offers one of the best optical elements for producing coherent and divergent beams, both properties being extremely important for CXDI experiments.

WGs have properties that make them worthy of further development and studies: (i) they work over a large energy range, from soft to hard X-rays; (ii) unlike capillaries, which are made of glass, WGs can have different cladding materials that can be optimized for the required energy; (iii) the roughness of the reflecting surfaces can be controlled down to fractions of a nanometre; (iv) WGs can provide beam dimensions from micrometers down to few nanometres; (v) they are relatively easy to fabricate, and quite cheap; (vi) they inherently provide coherent beams, because they are based on the propagation of resonance modes; (vii) multiple WGs can be fabricated close to each other, in order to create interference patterns [Ollinger, 2005].

This chapter is devoted to the basic theory of planar X-ray WG. The basic concepts and equations of the total reflection will be reported in (2.1). Then the propagation of the electromagnetic field in the WG guiding layer will be described, taking into account also absorption (2.2). Moreover the different radiation coupling methods and the corresponding field structure inside the guiding core will be briefly reported (sections 2.3, 2.4 and 2.5). Finally, the self-imaging effect, well know and studied for gratings will be exploited for the WG (2.6 and 2.7).

2.1 Total reflection

As we have seen in section 1.1, the refraction index in the X-ray energy region is usually written as $n(\omega) = 1 - \delta(\omega) - i\beta(\omega)$, where δ and β are given by (1.7). As a typical value $\delta \approx 10^{-6}$ for hard X-ray. Hence the real part of the refraction index is smaller than one. As a consequence for X-rays matter is optically less dense than air or vacuum, a fact which leads to *total reflection in air*.

If we consider a plane wave incident over an interface between two homogeneous media, with index of refraction n_1 and n_2 respectively, the grazing angle of incidence θ_i and the grazing angle of the refracted field θ_r are related through the *Snell law* (Fig.(2.1)):

$$n_1 \cos \theta_i = n_2 \cos \theta_r \qquad (2.1)$$
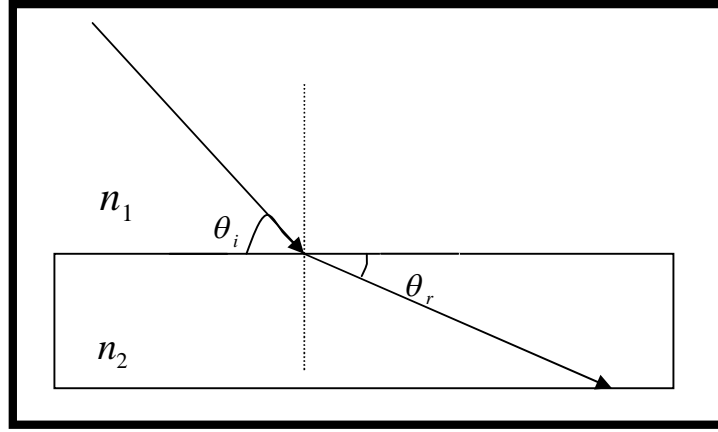
Figure 2.1: *Schematic picture of the Snell law.*

An interesting case is when $n_1 > n_2$ (i.e. $\delta_2 > \delta_1$, as in the case of an interface air-material). In this case it turns out that we have a limiting situation in which $\theta_r = 0$ and the corresponding angle of incidence is called *critical angle*, defined by:

$$\cos \theta_c = \frac{n_2}{n_1} \qquad (2.2)$$

If we discard absorption ($\beta = 0$) for all $\theta_i < \theta_c$ the wave is totally reflected at the interface between the two media. In the case of hard X rays the angles are usually quite small ($10^{-3} rad$) so that (2.2) reads $1 - \theta_c^2/2 \approx n_2/n_1$ and therefore,

$$\theta_c \approx \sqrt{2 \frac{\delta_2 - \delta_1}{1 - \delta_1}} \tag{2.3}$$

In the particular case of an air-material interface $\delta_1 \approx 0$ and $\theta_c \approx \sqrt{2\delta_2}$.

The reflection coefficient, defined as the ratio of reflected to incident intensity [Atwood, 1999], is reported in Figs. (2.2) as a function of the incident angle and for different values of the photon energy in the case of an ideal air-Si (Figs. (2.2a)) and air-Au (Figs. (2.2b)) interfaces. It is worth to note that changing the energy corresponds to change the ratio between β and δ. The ideal case of a unitary reflection coefficient is reached in the limit of small incident angles ($\theta_i << \theta_c$) and high energies ($\beta << \delta$) but in general there is always a penetration in the material.
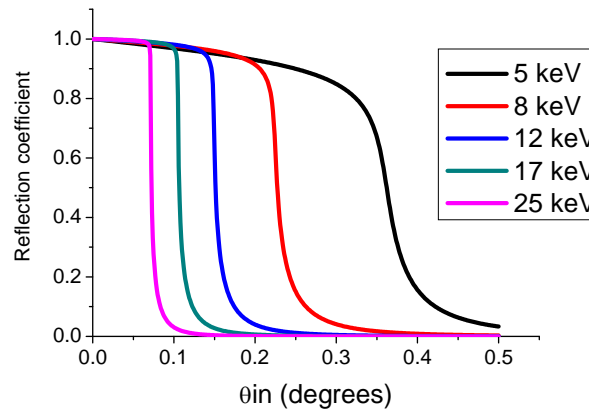
Figure2.2: *Reflection coefficient for an ideal air-Si surface as a function of the incident angle and for different energies of the impinging radiation.*

2.2 Field propagation inside the waveguide

A WG can be depicted as a very narrow channel (typical size of tens to hundreds of nanometres) in which the incoming radiation is trapped by multiple total internal reflections, providing the angle of incidence is less than the critical angle. Thus the basic working-principle of such device is just the total reflection described above (see Fig. (2.3)). The x-ray radiation propagates in the channel in the form of a discrete set of modes called *resonant modes* or *eigen-modes* of the WG, to which corresponds a particular incident angles called *resonant angles.*
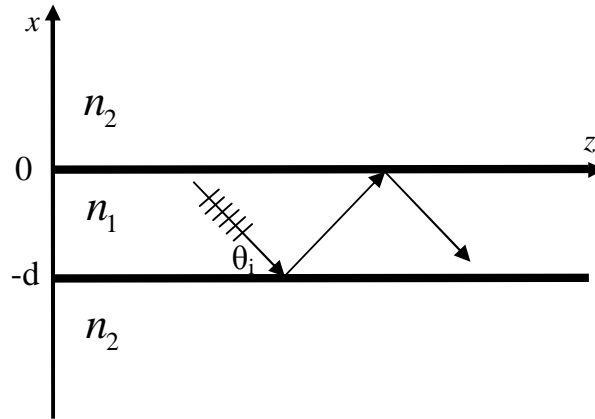
Figure 2.3*: Schematic picture of a waveguide.*

Analytically each mode is a solution of the Helmhotz equation:

$$\nabla^2 V + k^2 n(x)^2 V = 0 \tag{2.4}$$

with proper boundary conditions. In the case of the WG depicted in Fig. (2.3) we have:

$$n(x) = \begin{cases} n_1 & for \quad -d < x < 0 \\ n_2 & elsewhere. \end{cases}$$

(2.5)

For sake of simplicity we treat a planar problem, i.e. $V = V(x, z)$ (this is not a loss in generality in mode description) and we neglect absorption, assuming the refractive index to be real. Finally we look for a solution far enough from the waveguide entrance to assume a solution of the form:

$$V(x, z) = V(x)e^{-i\gamma z}$$

(2.6)

i.e. an invariant cross-section beam [Gori, 1995]. With these approximations equation (2.4) reads:

$$\frac{\partial^2 V(x)}{\partial x^2} + (n^2 k^2 - \gamma^2)V(x) = 0$$

(2.7)

Here γ is the projection of the wave vector of the incident plane wave onto the z-direction,

$$\gamma = n_1 k \cos\theta$$

(2.8)

also known as *propagation constant*. Following [Marcuse, 1974], the solution for $V(x)$ reads:

$$V(x) = \begin{cases} A\exp(-\chi x) & for\ x \geq 0 \\ B\cos(\kappa x) + C\sin(\kappa x) & for\ 0 \geq x \geq -d \\ D\exp[\chi(x + d)] & for\ x \leq -d \end{cases}$$

(2.9)

where A, B, C and D are constants and

$$\kappa^2 = k^2 n_1^2 - \gamma^2$$
$$\chi^2 = (n_1^2 - n_2^2)k^2 - \kappa^2$$

(2.10)

For *Transverse Electric* modes (i.e. modes without the z-component of the electric field) we impose the continuity of V and of dV/dx at the interfaces between the two media. This leads to the *transcendental eigenvalue* equation:

$$\tan(\kappa d) = \frac{2\chi\kappa}{\kappa^2 - \chi^2}$$

(2.11)

With the use of (2.2), (2.8) and (2.10) and some algebra one can rewrite (2.11) as:

$$\tan(\frac{kd \sin\theta - (m-1)\pi}{2}) = \frac{\sqrt{\cos^2\theta - \cos^2\theta_c}}{\sin\theta}$$

(2.12)

The numerator of the right hand side of (2.12) becomes imaginary for $\theta > \theta_c$. Therefore (2.12) has a discrete *finite* set of solutions called *resonance angles* $\theta_m < \theta_c$ one for each value of the integer m, that we can visualize as the intersections of the right and left handed side plots of equation (2.12). As we said before, each solution uniquely represents a *mode* of the WG, specified by its resonance angle θ_m for which the corresponding eigen-mode ψ_m is given by (2.9). In Figs. (2.4) an example of graphical solution of (2.12) and the field distribution for the first three modes are displayed.

In order to obtain an explicit expression for the resonance angles we can take in (2.12) the limit of extreme glancing angles $\theta << \theta_c$ obtaining the *Bragg relation*:

$$m\lambda = 2n_1 d \sin \theta \qquad (2.13)$$

from which

$$\theta_m \cong \frac{m\lambda}{2n_1 d} \qquad (2.14)$$

This approximation is quite strong and it does hold only for lower order modes. As a typical value $\theta_m \approx 10^{-3}$ rad, and therefore we can consider the angles small and adopt the *paraxial approximation* (section 1.5.1).
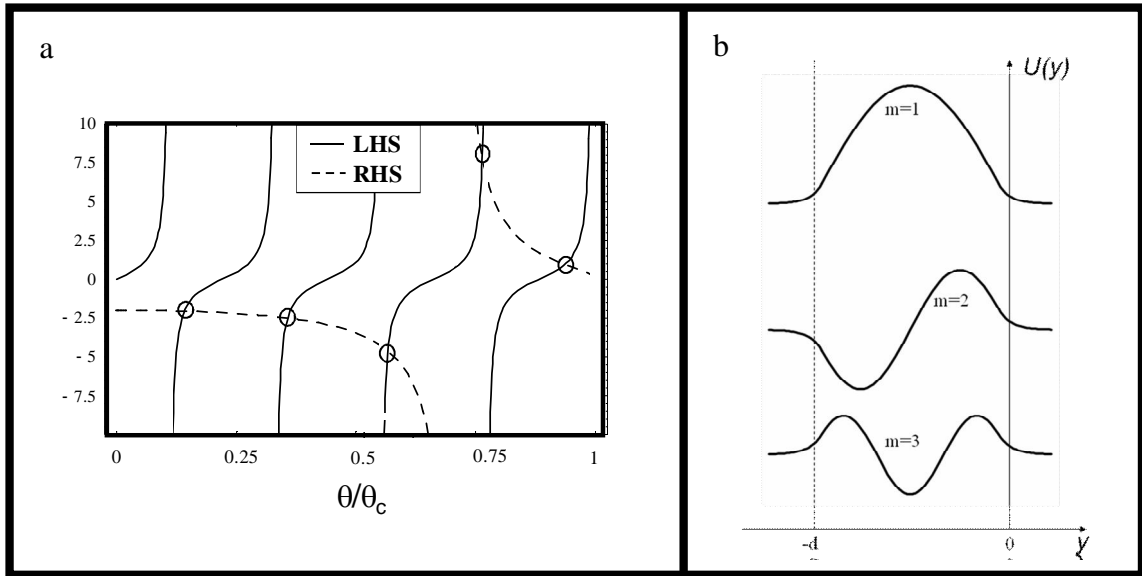
Figure 2.4: *a) Graphical solution of the transcendental eingevalue equation (2.12). The intersections between the two curves represent the resonance angles. In this example a WG with air gap and Si claddings with d= 100 nm and λ= 0.1 nm is considered. b) Corresponding solutions (2.9) for the amplitude distribution inside the air gap guiding layer for m=1, 2, 3.*

A plane monochromatic wave illuminating the entrance aperture of a front coupling waveguide (see section 2.4) excites a set of eigen-modes inside the *air-gap* ($n_1 \approx 1$):

$$U(x,0) = \sum_{m=1}^{m_{\max}} a_m \psi_m(x) \tag{2.15}$$

where $m_{\max}$ is the maximum number of supported modes. We can estimate it dividing the angular range of possible resonance angles θ_c by the separation between adjacent resonance angles calculated from (2.14):

$$m_{\max} \cong \left[\frac{kd \sin \theta_c}{\pi} \right] + 1 \tag{2.16}$$

where $[.]$ means the integer part operator.

The coefficients a_m of the expansion can be estimated using overlap integral:

$$a_m = \frac{\int U(x,0) \psi_m(x) dx}{\sqrt{\int \psi_m^2(x) dx}} \tag{2.17}$$

At the distance z the field profile changes and can be written as

$$U(x,z) = \sum_{m=1}^{m_{\max}} a_m \psi_m(x) \exp(i\gamma_m z) \tag{2.18}$$

where γ_m is the propagation constant (2.8) for the corresponding mode:

$$\gamma_m = k \cos \theta_m \tag{2.19}$$

The transversal wave number k_{xm} and the propagation constant γ_m are related by the dispersion equation:

$$k_{xm}^2 + \gamma_m^2 = k^2 \tag{2.20}$$

with

$$k = 2\pi/\lambda; \qquad k_{xm} = k\sin\theta_m \approx k\theta_m \cong m\pi/d \tag{2.21}$$

$$\gamma_m = k\cos\theta_m \approx k(1 - \theta_m^2/2) \approx k + m^2\pi\lambda/4d^2. \tag{2.22}$$

Expression (2.18) is derived for the field inside the WG guiding layer neglecting the imaginary part of the refraction index, i.e. the absorption. In general absorption is not negligible and leads to a penetration of the modes in the claddings layers with a consequent energy loss for each reflection.

The general case of a tapered WG, i.e. a WG with the entrance gap dimension different from the exit gap dimension and therefore not parallel claddings, is fully treated in Bukreeva et al. [Bukreeva, 2010].

Incidentally one can note that the WG provides also a broad energy filter for the incoming radiation. As described above, the WG works in total reflection conditions, thus the high energy *bremsstrahlung* from the primary source is not reflected and mostly absorbed by the claddings [Pelliccia, 2010]. For instance, if coupled with a Cu target primary source (as in the case of the WG based microscope described in section 4.1), the WG essentially transmits the Cu K$_\alpha$ with low high-energy background.

2.3 Phase space acceptance

Full spatial coherence, the situation in which phase is perfectly correlated at all points transverse to the propagation direction, can be achieved with a spherical wavefront, which we associate with a point source. To estimate "how small is a point source" one can start from the

Heisenberg's uncertainty principle, which can be re-written in the following form [Attwood, 1999]:

$$\Delta x \Delta \varphi \geq \frac{\lambda}{4\pi} \qquad (2.23)$$

where Δx is the modulus of the uncertainty in position and $\Delta \varphi$ in the direction. Identifying the source diameter as $d = 2\Delta x$, and the divergence half angle φ respect to the direction of propagation with the uncertainty $\Delta \varphi$, the follow limiting relationship can be obtained

$$d \cdot \varphi = \frac{\lambda}{2\pi} \qquad (2.24)$$

which determines the smallest source size we can discern. To generate a spatially coherent source one must develop a source that approaches this limit (the correspondent radiation is *diffraction limited*). Equation (2.23) can be interpreted in terms of the *spatial acceptance* Δa and the *intrinsic angular acceptance* $\Delta \varphi$ of the WG. For a generic optical component, the first one can be calculated as the component transmission function integral over its geometrical aperture [Jark, 2004], while the second is the numerical aperture of the optics. In terms of Δa and $\Delta \varphi$, (2.23) can be re-written as

$$\Delta a \Delta \varphi \geq \frac{\lambda}{2\pi} \qquad (2.25)$$

Therefore a planar WG can accept, as a lower limit, a *phase-space* volume given by (2.25). In front coupling scheme (see next section) $\Delta a \approx d$ whose minimum value corresponds to $\Delta \varphi \approx \theta_c$. Moreover the minimum volume in the phase-space is just the coherence volume we introduced in section 1.5.4. Therefore we can state that, under *appropriate conditions*, a WG optic can accept the coherent volume of incoming radiation: one mode of the incoming field is coupled to one mode of the WG.

2.4 Radiation coupling methods

The incident radiation can be coupled into the guiding layer of X-ray WGs in two different ways: resonant beam coupling (RBC) and front coupling (FC). RBC [Marcuse, 1974] takes place in a three layer WG, with the incident beam at grazing angle transmitted by the very thin upper layer and trapped by the intermediate guiding layer (see Fig. (2.5a)); with this scheme the incoming beam of several tens of microns can be compressed down to nanometres dimensions and significant effective gain can be achieved [Jark, 2001]. In the FC scheme (Fig. (2.5b)) the incoming radiation is directly side-coupled with the WG aperture [Pelliccia, 2007]. A variant of the front coupling scheme can be adopted with a reflection of the incoming beam just in front of the WG entrance, at one of the resonance angles (Fig. (2.5c)). In this way only one particular mode could be selected (see next section).
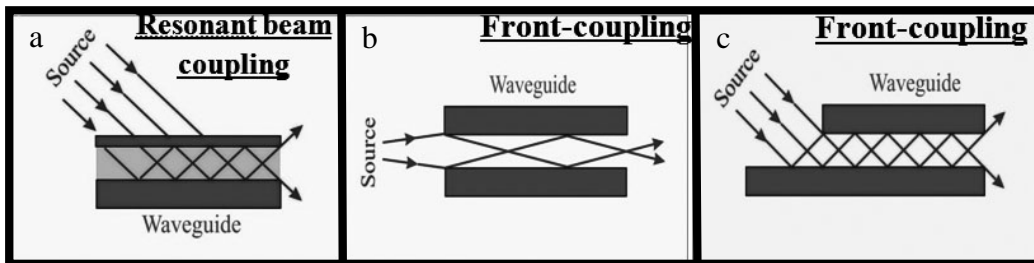
Figure 2.5*: Schematic picture of the possible radiation coupling methods.*

2.5 Mono-modal propagation and mode-mixing

In the general case the field inside the guiding layer has the structure (2.18) which means that actually a finite number of modes weighted by the correspondent coefficient a_m are simultaneously present in the guiding layer. We have to distinguish two cases:

60

i)   *mode mixing*: more than one mode is present in the guiding layer and the wave front changes during the propagation. Therefore the wave front at the WG exit depends on the exact length of the WG. In general, at the generic distance z each mode has different phase shifts, hence the total field has not a completely definite phase i.e. is only partially coherent.

ii)   *mono-modal propagation*: only one mode is present, i.e. all the coefficients a_m in (2.18) are zero except one. The wave front is constant during the propagation in the guiding layer and the produced field at WG exit is fully coherent.

Naturally the most desirable case is the mono-modal propagation and the consequent production of a fully coherent beam. In order to obtain a mono-modal propagation one can fabricate a WG with a sufficiently small guiding layer. From (2.16) $d < \lambda/2n_1\theta_c$ should be sufficient. For example, considering an air-gap WG ($n_1 \approx 1$) with Silicon claddings at 8keV, this means $d < 20nm$. Naturally this case limits the photon flux at the WG exit.

A single-mode selection from a multimode WG (i.e. a WG which can sustain more than one mode) is a more complicated task. First of all, to get a single mode selection using a FC-WG, we need the FC method with the pre-reflection at the WG entrance (Fig. (2.5c)). If this is not the case, the beam will suffer a slit effect at the WG entrance with a consequent *diffraction enlargement* $\approx \lambda/d$ which larger than the angular separation between two adjacent modes (see equation 2.14). As a consequence multimode excitation will occur.

In the general case, necessary but not sufficient condition to obtain mono-modal propagation is that the divergence of the incoming radiation has to be much smaller than the angular separation between two adjacent modes. To go further in details, let us consider a monochromatic source of wavelength λ and a MI with gaussian shape of size s. If z_s is the distance of the source from the WG entrance, the incoming divergence is:

$$\Delta\alpha \approx \frac{s}{z_s} \qquad (2.26)$$

On the other hand the separation between two adjacent modes is:

$$\Delta\theta \approx \frac{\lambda}{2d} \qquad (2.27)$$

where again we assume an air-gap WG ($n_1 \approx 1$). Combining (2.26) and (2.27) one finds the condition:

$$\frac{s}{z_s} < \frac{\lambda}{2d}. \qquad (2.28)$$

It is important to note that this corresponds to a coherent illumination of *twice* the WG entrance:

$$\frac{\lambda z_s}{s} > 2d \qquad (2.29)$$

where the left hand side is the coherence length defined as definite in equation (1.57).

Although one can realize the optimal matching of the incoming field with the vacuum gap, i.e. satisfy (2.28) in FC configuration with pre-reflection and choose $\theta_{in} = \theta_m$, the phase mismatch between the incoming field and eigenmodes at the entrance aperture of the WG can excite more than one mode [Bukreeva, 2010]. In practice we ever have some mode-mixing due to the various imperfection of any real WG such as not perfect flatness of the surface in the guiding layer or non ideal entrance edges.

It is worth noting that in the case of a FC-WG without pre-reflection at the entrance, for which we ever have a multimode excitation inside the guiding layer, the condition (2.29) for coherent illumination become simply

$$\lambda z_s / s > d. \tag{2.30}$$

In this case usually one speaks of *coherent mode mixing*: the field is the overlapping of modes, but in the sum (2.18) only few modes are important, those which corresponds to the selected finite incident angle range. If equation (2.30) is not satisfied, the mode mixing is *incoherent* and all the coefficients a_m are important in (2.18). In practice in this case we will obtain a quasi completely incoherent beam at the WG exit.

It is important to stress that the coherence length as defined in section 1.5.5 is a concept that reduces the complex function MI to a single number, which increases monotonically with the source-WG entrance distance, a simplification that is valid only for Gaussian isotropic coherence functions [Nugent, 2010]. While this may be a reasonable starting point, it can also be a misleading oversimplification, as will be seen in section 4.5.

The different kinds of propagation in the guiding layer described here correspond to different experimental diffraction patterns in the far field region, as we will see in section 4.5.

.

2.6 Self imaging effect

When a monochromatic plane wave is subjected to a transversal periodicity the well-known Talbot effect [Talbot, 1936] takes place. Consider for example a transmitting grating with period D illuminated by a plane wave. Beyond the grating the incident field profile is self-repeated at the propagation distances $z_T = 2D^2 m / \lambda$, known as the Talbot distances, where m is an integer. Moreover other interesting self-imaging effects take place at fractional Talbot distances [Gori, 1995]. The wave field in a WG presents the self-imaging effect as well. This, for a WG in a visible region, was initially noted by Bryngdahl [Bryngdahl, 1973] and explained in more details by Ulrich [Ulrich, 1975]. We put in evidence this phenomenon for WGs working in the x-ray spectral region in a recent paper [Bukreeva, 2011]. The field inside the vacuum gap for symmetric excitation can be written as:

$$U(x,z) = \sum_{m=1}^{m_{\max}} a_m \cos(k_x x) \exp(i\gamma_m z) \qquad (2.31)$$

where respect to the general equation (2.18) we have $\psi_m = \cos(k_x x)$ with $k_x \approx k\theta_m$ which is the transverse spatial frequency and $\theta_m \cong \lambda m/p_x$, $p_x = 2d$. This is the case of the illumination by a plane wave parallel to the z axis (optical axis): only symmetric modes are excited inside the guiding layer and we can define a characteristic distance L_{WG} of the propagation can be introduced [Helfert, 2009]

$$L_{WG} = \frac{d^2}{\lambda} \qquad (2.32)$$

when all modes of the WG arrive in phase, and the input profile of the field is perfectly reconstructed. On the other hand the distance L_{GR} of self-imaging for a periodic phase grating with period D, duty factor 0.5, and phase shift π is equal to (see for x-ray radiation [Weitkamp, 2005])

$$L_{GR} = \frac{\left(D/2\right)^2}{\lambda} \qquad (2.33)$$

We can see that in the case of symmetrical excitation, equations (2.32) and (2.33) give the same self-image distances for the phase grating with period D and for the WG with a air-gap of $d = D/2$. In Figs. (2.6), the field after a grating with period D is compared with the field inside a WG with air-gap $d = D/2$. Computer simulation is based on the parabolic wave equation (PWE) numerical solution [Kopylov, 1995]. The parameters used in this particular case are: period of the grating D = 2d = 200 nm, wavelength λ = 0.154 nm, 0.5 duty cycle, and zero absorption in the cladding material. Virtual transversal periodicity in the WG exists

due to reflecting sidewalls. Note that at fractional Talbot distances $mL/2$ (here m is an odd integer number), the image of the field at the WG entrance is demagnified two times, as in the case of the phase diffraction grating (see Figs. (2.6a) and (2.6b)). Therefore, a suitable choice for the WG length can reduce at one-half the size of the exiting beam. Figure (2.6c) shows the cross section of the electromagnetic field corresponding the two arrows A and B in Fig. (2.6b), respectively, at the odd (dashed curve) and even (solid curve) fractional Talbot distances. As a consequence of the above considerations, a simple multimode WG in case of symmetric excitation can be treated as a virtual phase grating with a duty cycle of 0.5, phase shift π, and period $D = 2d$. A relevant difference in the propagation of guided modes with respect to the free space propagation of the field behind the phase grating, is that propagation of the field in the free space is lossless in the last case; instead, modes propagating in the WG decrease due to multiple reflections; in addition, the WG supports only a finite number of modes m_{max}. In the simulated case $m_{max} = 12$.
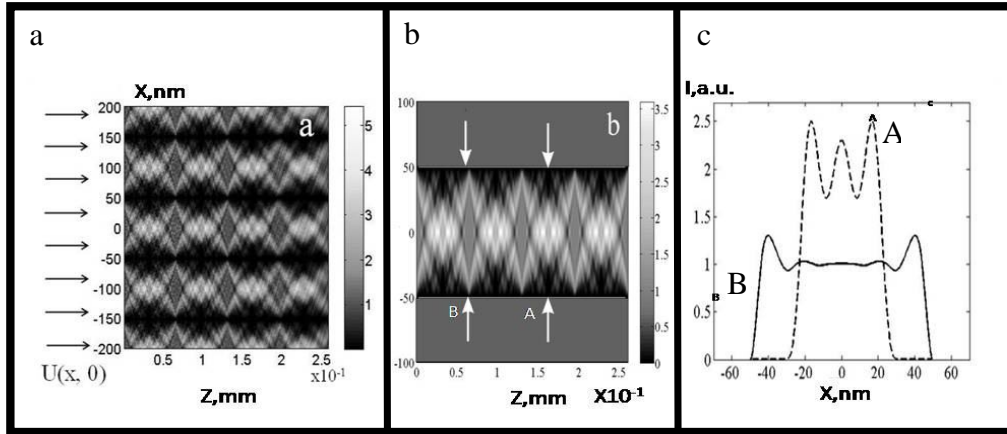
Figure 2.6*: Simulated x-ray intensity distribution (a) behind a phase grating with period D=2d=200 nm, λ=0.154 nm, 0.5 duty cycle and π phase shift and (b) in FC WG with vacuum gap d=D/2. (c) Lateral intensity distribution at odd (dashed line) and at even (full line) fractional Talbot distance.*

2.7 Multimode waveguide with periodic perturbation

Fig. (2.6b) refers to a WG with smooth reflecting sidewalls. If an optical element (for example, a sidewall grating) imposing an additional longitudinal periodicity on the field is introduced, the angular spectrum of the transmitted field is modified. The spectrum is given as the product of two terms, one related to the transversal, the other to the longitudinal properties [Kopylov, 1995; Jahns, 2009]. In the following, a combination of both situations is considered and the imposed periodicities in transverse and longitudinal directions are treated independently [Lohmann, 2005]. The transversal properties depend on the width d of the guiding layer, and the longitudinal ones depend on the modulation period introduced in the WG. The simple plane WG as a virtual transversally periodic grating has a discrete set of spatial frequencies defined in equation (2.31). The longitudinal component of the wave vector in parabolic approximation is quantized:

$$k_z^m = 2\pi \sqrt{\left(\frac{1}{\lambda}\right)^2 - \left(\frac{m}{p_x}\right)^2} \approx 2\pi \left(\frac{1}{\lambda} - \frac{m^2}{z_T}\right),$$

(2.34)

$$m = 0, \pm 1, \pm 2, ...$$

with the Talbot self-image distance $z_T = 2p_x^2 / \lambda$. The sidewall grating imposes additional longitudinal periodicity on the field with period p_z, and according the Montgomery equations, the k vectors of the wave field have to obey the condition [Helfert, 2009; Jahns, 2009]

$$u_z(x) = u_{z+p_z}(x) \Rightarrow u_0(x) = \sum_m A_m \exp(i k_x^m x)$$

(2.35)

The k_x components have the discrete angular spectrum given by

$$k_x^l = 2\pi \sqrt{\left(\frac{1}{\lambda}\right)^2 - \left(\frac{l}{p_z}\right)^2},$$

(2.36)

$$l = \pm 1, \pm 2, \ldots$$

The coefficients A_m depend on the groove shape. The transmitted field has to satisfy the resonance conditions both for the WG and for the grating (equations (2.34) and (2.36)). Mathematically these conditions can be written as:

$$(k_x^m)^2 + (k_z^l)^2 = \left(\frac{2\pi}{\lambda}\right)^2.$$

(2.37)

The modal structure in periodic WGs varies depending on the transversal and the longitudinal periods, as well as on the groove shape of the grating (i.e. on the coefficients A_m in equation (2.35)). Correspondingly, choosing the parameters appropriately, it is possible to suppress some modes, resulting in selective space filtering of the field passing through the structured WG. Because of the small value of resonance angles for the WG, the period of the sidewall grating can be significantly large with respect to the wavelength. In Fig. (2.7a), coherent mode mixing in a simple planar WG with a air-gap $d = 100$ nm and cladding Au layer is shown. The WG is illuminated with a plane monochromatic wave with a wavelength of 0.1 nm and the wave vector parallel to the optical axis. In Fig. (2.7b), the distribution of intensity is shown for a planar WG with the same parameters as in Fig. (2.7a) but with the additional longitudinal periodicity (structured WG) created with a step-like (Ronchi) grating on the sidewalls of the guiding layer. The grating has a period equal to the fractional Talbot distance $d^2/\lambda = 110$ µm and a duty cycle of 0.3. The calculations show that the *structured* WG with given parameters preserve low order symmetric modes of the planar WG. It is interesting to compare the results obtained when the WG is illuminated by a plane wave with the case of incoherent illumination. This case is reported in Fig. (2.7c) and (2.7d) which show the distribution of intensity in the guiding layer for the normal WG (Fig. (2.7c)) and the

67

structured WG (Fig. (2.7d)) illuminated by a spatially incoherent beam provided by an incoherent x-ray source of size $s = 15$ μm located at the distance $z_s = 1$mm from the WG. The WG was tilted at the angle $\alpha \approx \lambda/2d \approx 5 \times 10^{-4}$ rad (order of the angular width of the WG mode) with respect to the optical axis. In this case, a large set of modes are incoherently excited in the guiding layer. In fact, the coherence length $\lambda z_s / s$ of the incoming x-ray beam at the entrance aperture of the WG is ≈ 6.7 nm, much less than the width of the guiding layer (100 nm). In the simulation, the incoherent source is taken as the sum of elementary radiators with random phases. The obtained quasi-incoherent field is the average over many realizations of the random process. Fig. (2.7d) shows that, unlike the usual planar WG which transmits the partially coherent beam for a long distance, the periodic WG works as a filter for the coherent part, allowing only coherent radiation and low order symmetric modes to be transmitted.
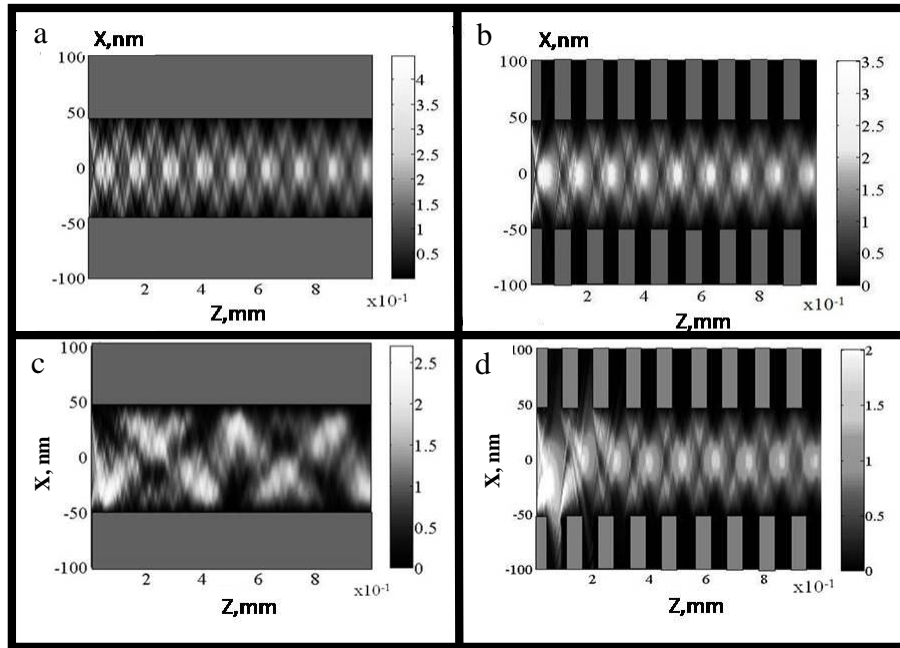
Figure 2.7: *Intensity distribution in the guiding layer of the WG for coherent source ((a) plane WG, (b) structured WG) and for incoherent source (asymmetric excitation; (c) plane WG (d) structured WG). PWE numerical solution.*

This feature can be particularly useful for imaging with x-ray laboratory sources whenever coherence is critical for image quality. Moreover, modes filtering by the WG can be crucial, also in CXDI experiments with synchrotron radiation when optical elements used for beam focusing can corrupt the degree of coherence of the field impinging on the sample.

3. Waveguide fabrication

The present chapter is devoted to the description of the physical requirements and the technological steps to be afforded to get a working one dimensional (1D) WG. The principal peculiarity of the designed WGs is that they are air-gap WGs. This is a distinct factor with respect to the WGs elsewhere produced and it allows a much higher efficiency i.e. it allows to minimize the beam intensity losses during the propagation in the guiding layer. However it imposes additional fabrication problems. In order to justify the choice of the used materials and technological processes, the chapter will start with some consideration about the benefits of the air-gap guiding layer with respect to other possible choices (3.1). Therefore the fabrication processes for simple and structured 1D WG will be described (3.2 and 3.3). Moreover some details about the fabrication problems will be reported in paragraph 3.4.

3.1 Air guiding layer

The fabrication of air guiding layer FC-WG leads an important improvement of the WG performances in term of *efficiency*. In general the efficiency of an optical element is defined as the ratio between the transmitted photons flux (= number of photons per unit time) by the optics and the incident photon flux on the optics. In our case, the efficiency can be written as:

$$\varepsilon = \frac{F_{wg}}{F_{inc}} \leq 1 \qquad (3.1)$$

where F_{wg} is the flux at the WG exit and F_{inc} the incident flux. On the same coupling condition, in order to maximize the efficiency one has to minimizes the following kind of intensity losses which occur during the propagation in the guiding layer:

1- Reflected intensity losses due to *absorption in the claddings materials.*
2- Intensity losses due to *absorption during propagation in the guiding layer medium.*
3- Reflected intensity losses in specular direction due to *interfaces roughness.*
4- Intensity losses in specular direction due to *scattering during the propagation in the guiding layer medium.*

It is obvious that the choice of air guiding layer minimizes the effects 2 and 4. To go further in details, some numerical examples are reported for the case of absorption in the following table. The absorption during the propagation in a 4 mm long guiding layer is reported for 8 and 17 keV, comparing air with other common materials used as guiding layer (see the corresponding references).

	Air	PMMA [Kohlstedt, 2008, Pfeiffer, 2002]	C [Salditt, 2008]
8 keV	4.75%	95.1%	97.9%
17 keV	0.77%	28.4%	36.0%

Effect 1 and 3 are present in any real reflective optics. In particular, the roughness problem will be discussed in section 3.4.

3.2 Fabrication process

The fabrication of 1D air gap WG consists essentially in an evaporation of two shoulders on a cleaned Si wafer. The process can be resumed in three steps. For clarity a side-view picture for each step (X-rays propagation direction perpendicular to the sheet) is reported:

1. The cleaned Si wafer is mounted on a metallic holder in order that its central part is masked.
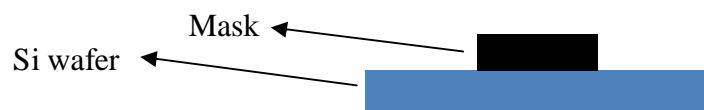

2. Few hundreds nanometres of the selected material (Cr or Au) are evaporated by electron gun evaporation. The actual technology permits in principle the control of the evaporated layer depth down to 0.1 nm.
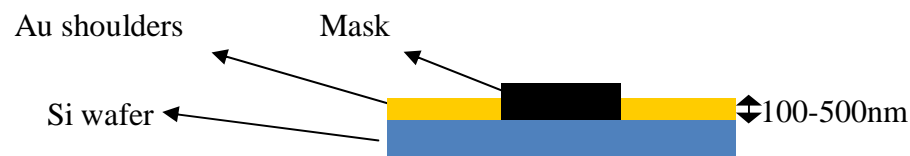
3. The obtained Si wafer with two identical shoulders and another cleaned Si wafer are closed like a sandwich with a little (just the necessary) mechanical pressure in a steel vice.
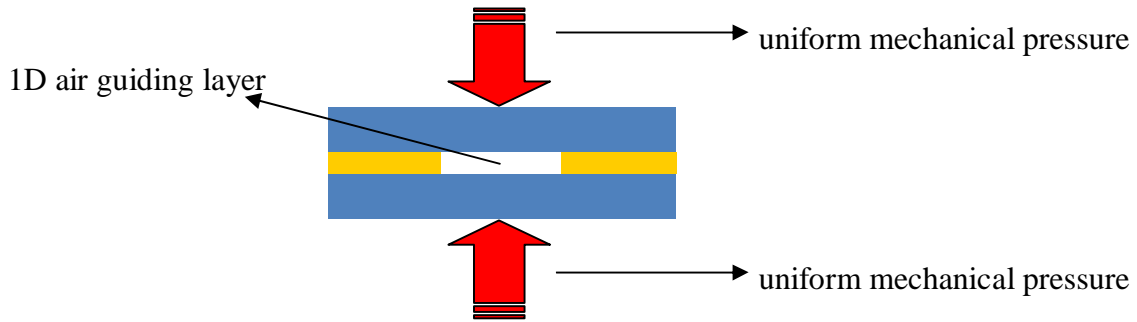
The choice of Cr or Au for the shoulders is due to the relative softness of these materials. Naturally the process does not permit to control the fabrication quality to nano-scale dimensions and does not guarantees the production of a working WG. All the processes except the evaporation are not repeatable process on nano-scale dimension. Till now the probability to find a working guiding layer was about 60%. In Fig. (3.1) a photo of the final device is reported.
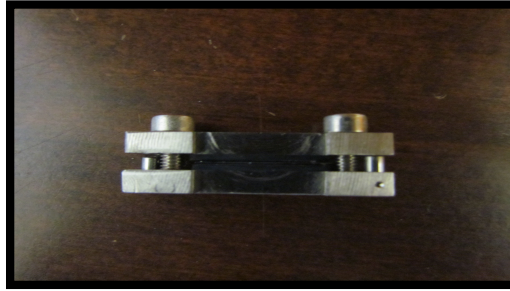

Figure 3.1: Photo of the final device. It is easy to distinguish from the outside to the inside(in the vertical direction): the steel vice, a rubber gasket, the Si wafers. Between them in the central part, the entrance gap of guiding channel is located.

3.3 Structured waveguide fabrication process

The fabrication process for the structured WG requires a preliminary treatment of the cleaned Si wafer before the simple fabrication process described in the previous section could start. As described in section 2.7, we want to impose an additional periodicity on the field inside the guiding layer. The simple way to do this is to fabricate a sidewall grating on the reflecting cladding walls. Despite the very narrow nano scale (100-500 nm) width of the guiding channel, the period of the grating is much larger than the wavelength and has a characteristic value of about 100 μm. Therefore, the realization of such a grating on the Si wafer does not present significant technological difficulties with the standard tools for micro- and nanofabrication. It can be resumed in three steps. In this case pictures depict wafers from the top (X-rays propagation direction in the sheet, perpendicular to the wafer longer side).

1. A protective mask which reproduces the negative of the grating profile is optically aligned to the cleaned Si wafer.

unprotected wafer stripes
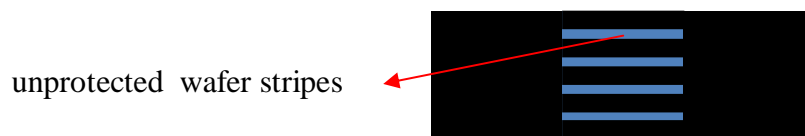
2. In order to obtain the desired grating, the masked Si wafer is treated with Reactive-ion etching (RIE) process. High-energy ions from an Oxygen plasma attack the unprotected wafer surface and react with it, eating the material and forming holes in correspondence of the unprotected Si stripes. A deep of about 2-3 microns is enough to obtain the desired side-wall grating effect. Typical dimensions of the grating structure are reported in the picture below.

"holes"   100μm   200μm   incoming X-ray radiation
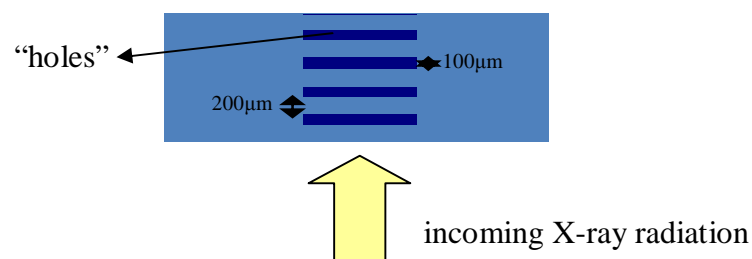
3. In order to obtain a good confinement of the radiation inside the guiding layer also for high order modes, 20 nm of Gold are deposed upon them by thermal evaporation.
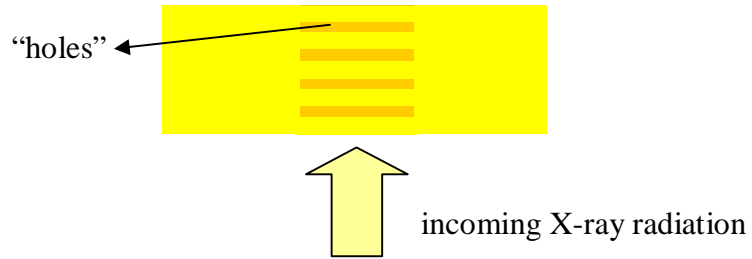
In Fig. (3.2) a Scanning Electron Microscope (SEM) image of the grating fabricated on the Si wafer is reported. At the moment, the first generation of structured WG is under test.
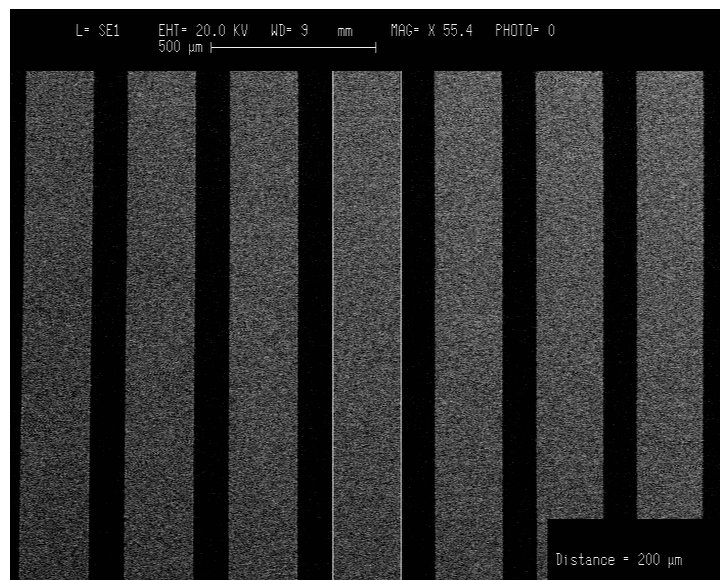
Figure 3.2: *SEM image of the side wall grating fabricated by RIE process on the Si wafer. The hole-stripes 100 µm wide separate the 200 µm wide zones of smooth Si. The X-rays travel in the left-right direction.*

3.4 Fabrication troubles

Roughness requirements

The surface roughness is a critical parameter for all reflective optics and especially for X-ray WG in which, as reported before, usually one has multiple reflections.

If the interface is ideally smooth and flat, the incident angle is equal to the reflected one and the reflected intensity can be found in the specular direction with respect to the incident one. Usually this is called *specular reflection*. This leads to the reflection coefficient defined in section 2.1 and reported in Fig. (2.2). In the real situation a certain surface roughness is always present and in the x-ray energy range ($\lambda \approx 0.1$ nm), it is a very critical parameter. The effect of roughness is to scatter part of the impinging radiation out of the specular direction, thus to decreases the actual reflected intensity. In the simple model proposed in [Croce, 1976] and [Sinha, 1988], valid for grazing incident angles, the specular reflectivity from a rough surface is estimated by multiplying the reflection coefficient for a *Debye-Waller* factor:

$$\Gamma = \exp(-2\Delta^2 k_i^2) \qquad (3.2)$$

where $k_i = k \sin \theta_i$ is the projected wavevector along the direction perpendicular to the surface and Δ represents the root mean square of the vertical interface roughness:

$$\Delta = \sqrt{\frac{1}{n} \sum_n \delta_n^2} \qquad (3.3)$$

where δ_n is the vertical distance between two different surface planes and the sum runs over all the possible vertical distances. In Fig. (3.3), the reflectivity curves for the air-Si interface at fixed energy and for different values of Δ are reported. It is clear that in order to minimize the intensity losses one has to reduce as much as possible the value of Δ. For this reason smoothed Silicon wafers ($\Delta \approx 0.2 - 0.3$ nm) are used as cladding walls in producing 1D

77

WG. If this might be useful, in order to obtain a good confinement of the radiation inside the guiding layer also for high order modes, some tens of nanometers of Gold is deposited upon them by thermal evaporation. This is the case of the structured WG. Generally evaporation process is preferable with respect to galvanic growth, when the preservation of the substrate smoothness is desirable. The root mean square of the vertical interface roughness Δ in the case of galvanic growth is around 20-25 nm, too big to produce an usable X-ray beam from the WG.
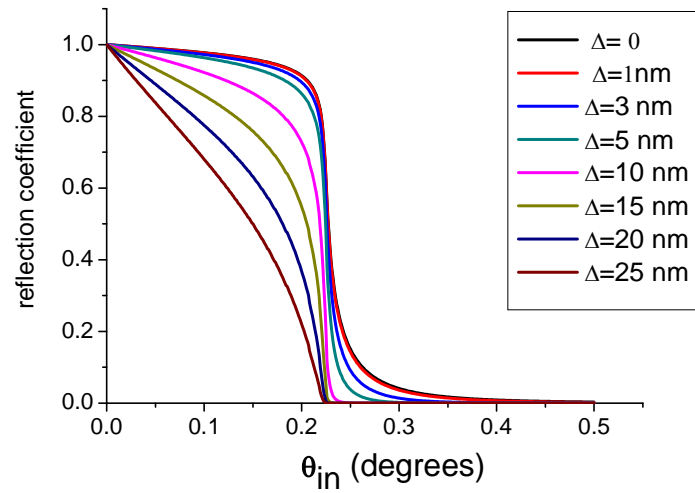
Figure 3.3*: Reflection coefficient for the air-Si interface as a function of the gracing incident angle for different values of the root mean square of the vertical interface roughness. The energy is fixed at 8 keV.*

Clamping problem

As reported in the description of the fabrication process (section 3.2), in order to complete the fabrication of the WG, one has to close the two prepared Si wafers one against each other. In general, the problem of facing two smooth surfaces with nanometric precision is not a trivial problem. Several solutions were explored in order to face the two Si wafers of the WG. For example there are different kind of wafer bonding procedures (see for example [Elwenspoek, 1998]) but the simplest method to face two Si wafers is press both wafers one against each

other by mean of a steel vice. The first successful front coupling x-ray WG [Pelliccia, 2007] was closed by using this method. The drawback is the big dimensions of the steel vice, which does not allow short WG-sample distance. However it is necessary to assure a uniform pressure along the Si wafers. In order to maintain a uniform pressure along the wafer using a small vice, a thin rubber gasket is inserted between the steel and each Si wafers.

Cleaning procedure

Another critical factor to obtain a working air gap X-ray WG is the cleaning of the Si wafers used to make the device. In the case of 1D WG we want to obtain a thin air guiding layer (100-500 nm) between two Si wafer. Therefore nothing bigger than few tens of nanometres has to lie on the surface of the Si wafers used to make the WG.

The fabrication procedure starts from pre-cut and lapped Si wafers covered with resist on both sides. The cleaning procedure is the first stage performed on them and it can be resumed in three steps:

1- Removal of the Si dust from the edges of the wafer
2- Removal of the Resist from both sides of the wafer using hot acetone
3- A final cleaning using Isopropyl alcohol vapours

A major difficulty lies in handling the pieces of silicon whom edges, after the first step, have to remain dust free and so completely untouchable.

4. Waveguide based microscope and beam characterization

The chapter is dedicated to the description of the WG-based propagation phase contrast microscope used to realize the experiments presented in next chapters. The microscope setup and the corresponding optimal configuration will be described in section 4.1. Particular attention will be dedicated to the choice of the distances which optimize the microscope performance in terms of resolution. In particular it will be emerge that a coherent illumination of the WG entrance gap is necessary. In sections 4.2, 4.3 and 4.4 a brief description of some crucial experimental issues will be reported. In particular the evaluation of the experimental distances will be discussed in details. In section 4.5 the characterization of the WG beam will be described. Experimental results will be shown in a variety of configurations and coupling schemes with laboratory source. The results obtained will be explained and commented. Finally in section 4.6, the experimental demonstration of the necessity of a coherent illumination of the WG entrance gap in order to obtain the best resolution, will be reported.

4.1 Waveguide based microscope setup and configuration

In order to realize high resolution waveguide-based imaging experiments, the appropriate experimental setup was build up at the X-ray laboratory of the Institute for Photonic and Nanotechnology (CNR, Rome). In general, many technical and practical requirements and constraints have to be considered to get sub-micrometer resolution in a standard laboratory. The basic experimental setup for waveguide-based imaging of test objects and biological samples is presented in the scheme of Fig.(4.1). The X-ray radiation is produced by a micro-source (NOVA 600, Oxford Instruments) with Cu anode and nominal source size of 15 µm.

Therefore the transmitted radiation by the WG, which provides also a broad energy filter for the incoming radiation (see section 2.2), is the Cu K_α line with a low high-energy background [Pelliccia, 2010].
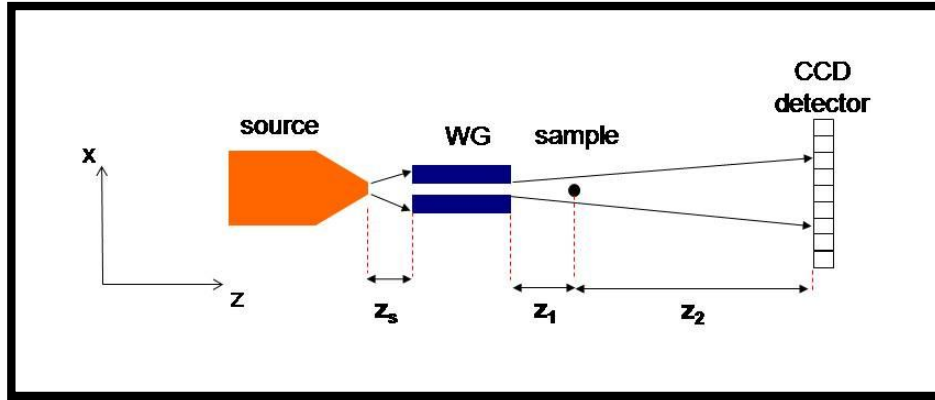
Figure 4.1: *Scheme of the WG-based propagation-phase contrast microscope. The significant distances are reported.*

This fact allows neglecting the chromatic contribution to the spatial resolution (see section 1.5.5). The primary source is pre-aligned with a CCD-based detector with nominal pixel size of 12.3 µm and measured Point Spread Function (PSF) of about 36 µm. In order to align the WG and the sample between the primary source and the detector, two alignment stages are necessary. The WG alignment stage ("main" stage) needs to fulfill some technical requirements. It is made up by 3 "big" translations x,y,z (range in the order of some centimeters) and a rotation stage in the plane x,y mounted over the "big" translations. This rotation must have a minimal step in the order of 10 µrad ($\approx \Delta\theta_m/10$). Moreover an x,y translation above the rotation is necessary in order to align the WG entrance on the rotation axis. A second stage must be implemented right behind the first one to allow for positioning of samples that are supposed to be illuminated by the WG beam. Furthermore, it is necessary to fabricate all the mechanical pieces in order to minimize the encumbrance and permit to put the sample as close as possible to the WG exit.

In configuring the WG based microscope one has to choose three distances:

1- The primary source-WG entrance distance (z_s)
2- The WG exit - sample distance (z_1)
3- The WG exit - detector distance ($z_1 + z_2$)

The proper choice of these distances is essential to obtain the best resolution in our measurements. The total distance $z_1 + z_2$ cannot be too large, essentially for intensity reasons. The gain in resolution that one obtains incrementing $z_1 + z_2$ (both the square terms under square root in equation (1.65) are inversely proportional to $z_1 + z_2$) is too small respect to the loss in intensity during the propagation to the detector ($\propto 1/(z_1 + z_2)^2$). In our particular case $z_1 + z_2 \approx 30$ cm. This value assures that an exposure time on the order of 100 s is enough to get sufficient contrast with our source and detector.

As anticipated in section 1.5.5, if $s \ll PSF$, in order to minimize the spatial resolution (1.65) one has to choose $z_1 \ll z_2$. To go further in details, in order to *completely* neglect the detector contribution in equation (1.65), the following condition should be satisfied:

$$\left(s \frac{z_2}{z_1 + z_2} \right)^2 \gg \left(PSF \frac{z_1}{z_1 + z_2} \right)^2 \tag{4.1}$$

that can be considered satisfied if

$$\frac{s}{PSF} \gg \frac{z_1}{z_2} \tag{4.2}$$

In the case of interest here, typical values for s and PSF give $s/PSF \approx 10^{-2}$. With $z_2 \approx 30$cm, z_1 has to be on the order of fraction of millimeter. Normally, due to the encumbers of the alignment stages and of the sample holder, the minimal value for z_1 is around 1 mm and this

is the choice was made to obtain the best resolution. It is worth noting that for $z_1 = 1$ mm, $z_2 = 30$ cm, $s = 200$ nm and $PSF = 18 \mu$m, the source and the detector contributions to the resolution (square root of left and right side of (4.1), respectively) are comparable. We already have demonstrated in Pelliccia et al. [Pelliccia, 2010] that such X-ray WG based microscope can provide phase contrast images at spatial resolution of few hundred nanometers, both from inorganic low-Z samples, from high-Z nanopatterned samples, and from biological samples, using either microfocus or standard x-ray laboratory sources.

Finally one has to optimize the distance z_s. In order to maximize the photon flux at the WG entrance, one can choose z_s as small as possible. This was the choice made in the work presented in [Pelliccia, 2010]. In practice, minimizing z_s one maximizes the WG angular geometrical acceptance and hence the photon flux at the WG exit. But in this way all the angles till the critical one will be selected, with a consequent considerable degradation of the coherence of the WG exit beam. The net effect is a worse in the obtainable resolution, as it will be demonstrated in section 4.6.

Therefore the best choice for z_s is the value for which the WG entrance gap is coherently illuminated. In the case of a Gaussian shape for the MI it is the value for which condition (2.34) (or (2.35) for FC-WG without pre-reflection at the entrance) are satisfied. In this way one can select a small incident angle range around the *first* resonance angle. It is the smallest resonance angle and then the most distant from the critical one. Therefore this choice assures to minimize the penetration in the claddings. Moreover the first resonance angle corresponds to the minimum number of reflections during the propagation in the guiding layer and then in correspondence of it the intensity losses due to multiple reflections are minimized. In addition, at the first resonance the two exit beams are intrinsically overlapped. This produces a further increment in the usable intensity at the WG exit.

Finally it is important to stress that using a single planar WG, one gets high magnification and high resolution only in one direction. For instance, in the measurements presented in the next chapters, the WG is vertically aligned and then high resolution microscopy is realized only in the horizontal direction. In this case the two different magnification values (the vertical and the horizontal one) will be specified. In order to obtain 2D high resolution WG based

microscopy, the alignment of two planar WG in cross configuration is necessary. The WG cross configuration was already successful used at synchrotron radiation facilities (see for example [De Caro, 2008(2); Giewekemeyer, 2011]. Its implementation in a common laboratory is under processing.

4.2 Lower limit for the resolution

Suppose to choose z_1 so small that the detector contribution to the spatial resolution (1.65) becomes completely negligible. In this limit the expression (1.65) gives:

$$\lim_{z_1 \to 0} \sqrt{\left(s \frac{z_2}{z_1 + z_2} \right)^2 + \left(\frac{PSF}{M} \right)^2} = s \qquad (4.3)$$

Therefore the WG exit aperture dimension represent the lower limit for the WG based microscope resolution. It seems appropriate to take up a more suitable diffraction-based point of view and connect the result expressed by (4.3) with the numerical aperture (NA) of the imaging system. For a lens less imaging system the NA is defined as the maximum angle with respect to the optical axis at which light can be detected [Nugent, 2010]. The corresponding resolution of the system is:

$$r_{NA} \approx \frac{\lambda}{2NA}. \qquad (4.4)$$

For the WG based microscope, the numerical aperture relevant for image formation in the best condition in which one can completely neglect the detector contribution is determined by the opening angle of the wave diffracted from the waveguide exit aperture, i.e. the divergence of the waveguide beam α_{WG}. Therefore [Giewekemeyer, 2010]

$$r_{NA} \approx \frac{\lambda}{2NA} = \frac{\lambda}{\alpha_{WG}} \approx \frac{\lambda}{\lambda/s} = s \qquad (4.5)$$

Expression (4.5) represents the result of expression (4.3) reached starting from a more fundamental point of view. It is worth to note again that s will not be exactly the physical dimension of the WG exit gap but the dimension that reproduces the divergence (or the coherence length) of the WG beam on the sample.

4.3 Instabilities and measures repeatability

As for all experimental setup, our microscope is subjected to some instabilities which waste the repeatability of a single measure producing an uncertainty on the measured intensity. The supposed origin of such instabilities is the thermal electronic noise of the detector, the thermal oscillations of the primary source and the mechanical vibrations of the entire setup.
In order to pull down this uncertainty on the measured intensity, the average intensity value of several identical measurements can be calculated as done for the measurements presented in chapter 5.

4.4 Uncertainty on the measured distances

It is very important to estimate the error on the distances measurements z_1, $z_1 + z_2$ and the corresponding magnification M. The magnification can be evaluated in two independent ways:

-   Indirectly, from a direct measurement of the distances z_1 and $z_1 + z_2$,
-   Directly, from a direct measurement of the magnification of a known distance.

In the first case the magnification is evaluated using expression (1.34):

$$M = \frac{z_1 + z_2}{z_1}.$$
(4.6)

The corresponding error calculated using the standard propagation error theory is:

$$\delta_M = \sqrt{\left(\frac{\delta_{z_1+z_2}}{z_1}\right)^2 + \left(\frac{z_1 + z_2}{z_1^2}\delta_{z_1}\right)^2}.$$
(4.7)

The distance z_1 and the total distance $z_1 + z_2$ have to be measured with a common rule. In the best cases, using particular accuracy, one obtains a measurement with an error of 0.3 mm for both z_1, $z_1 + z_2$. In this situation, for a fixed total distance $z_1 + z_2 = 269$ mm, the error (4.7) is dominated by the second term under the square root and for the relative error one obtains:

$$\frac{\delta_M}{M} \approx M \frac{\delta_{z_1}}{z_1 + z_2} \approx M \cdot 0.00112.$$
(4.8)

Therefore the relative error δ_M / M increases linearly with the magnification value. This leads to a good evaluation for M < 60 (δ_M / M <7%). Unfortunately we are interested to bigger magnification values. Nevertheless this is the procedure for a preliminary rough estimation for the magnification and the corresponding distances.
In the second case one has to perform a direct measurement of the magnification. It can be done measuring the enlargement on the detector plane of a known dimension on the object plane. The used expression for the measured magnification and the correspondent error will be:

$$M_m = \frac{N_p \times \Delta_p}{\Delta\eta}$$
(4.9)

$$\delta_{M_m} = \sqrt{\left(\frac{\Delta_p}{\Delta\eta}\delta_{N_p}\right)^2 + \left(\frac{N_p \times \Delta_p}{\Delta\eta^2}\delta_{\Delta\eta}\right)^2} \qquad (4.10)$$

where N_p is the number of pixels on the detector, Δ_p the pixel size dimension and then $N_p \times \Delta_p$ is the enlarged dimension on the detector plane. $\Delta\eta$ is reference dimension on the object plane. It is a known displacement of the sample. In practice one has to perform a known displacement of the sample using the motorized sample stage and then measure how it enlarges on the detector plane. In this case the problem arises from the very small field of view one has for big magnification values. For example, fixing again the total distance to $z_1 + z_2 = 269$ mm, if $M \approx 45$ and then $z_1 \approx 6$ mm, the field of view allows to visualize a displacement $\Delta\eta = 10$ µm on the object plane and (4.10) gives $\delta_M = 3$ ($\delta_M/M \approx 7\%$). Instead, if $M \approx 207$ and then $z_1 \approx 1.3$ mm, the effective field of view on the sample will be on the order of few microns. Therefore at such big magnification values the displacement $\Delta\eta$ cannot be larger than few microns and will become comparable with the error $\delta_{\Delta\eta}$ due to the motorized sample stage ($\delta_{\Delta\eta} \approx 0.5$ µm). This fact strongly affects the absolute error (4.10) on the measured magnification and produces a relative error which is too big to make the measurement (4.9) acceptable. For instance, with $z_1 + z_2 = 269$ mm, $z_1 \approx 1.3$ mm, $M \approx 207$, $\Delta\eta \approx 2$ µm, the absolute error is $\delta_M = 52$ and the relative one $\delta_M/M \approx 25$ %. The use of a piezo motor should overcome the problem, lowering the error $\delta_{\Delta\eta}$ at least of one order of magnitude.

The strategy to partially overcome the problem is to perform the measurement (4.9) at a distance z_1 with sufficient field of view. Once obtained from (4.9) the magnification one can obtain the correspondent value for the distance z_1 by inverting (4.6):

$$z_1 = \frac{z_1 + z_2}{M_m} \qquad (4.11)$$

$$\delta_{z_1} = \sqrt{\left(\frac{\delta_{z_1+z_2}}{M_m}\right)^2 + \left(\frac{z_1+z_2}{M_m^2}\delta_{M_m}\right)^2} \qquad (4.12)$$

Once fixed this best estimation z_1^{best}, one can use it as a "starting position" and reaches all the others z_1 positions using the motorized sample alignment stage that assures movements Δz with an absolute error $\delta_{\Delta z} = 0.5$ µm. Therefore

$$z_1 = z_1^{best} + \Delta z \qquad (4.13)$$

$$\delta_{z_1} = \delta_{z_1^{best}} + \delta_{\Delta z} \qquad (4.14)$$

It results $\delta_{z_1^{best}} \gg \delta_{\Delta z}$ and hence $\delta_{z_1} \cong \delta_{z_1^{best}}$ for each z_1. Using (4.11) and the total distance $z_1 + z_2$, the best estimation for the various magnification values can be obtained from the well known

$$M^{best} = \frac{z_1 + z_2}{z_1'}. \qquad (4.15)$$

The corresponding error is

$$\delta_{M^{best}} = \sqrt{\left(\frac{\delta_{z_1+z_2}}{z_1}\right)^2 + \left(\frac{z_1+z_2}{z_1^2}\delta_{z_1}\right)^2} \qquad (4.16)$$

This is the procedure used to evaluate the distances and corresponding magnifications for the microscopy measurements presented in chapter 6.

In the case of a test sample, i.e. a known object, one can improve the distances evaluation comparing the measured intensity profile with the correspondent calculated simulation. Therefore a series of simulations are performed at fixed total distance $z_1 + z_2$ (the value obtained using the rule) and varying the distance z_1. The z_1 value and the corresponding magnification which optimize the superposition between the experimental and the simulated data are taken as best estimations (z_1^{best}, M^{best}). For resolution reasons, it is convenient to perform this optimization at the smallest z_1 distance. A rigorous evaluation of the error on z_1^{best}, M^{best} is not a trivial problem in this case. A number of simulations corresponding to the case we facet experimentally show that a variation of 4% around the value chosen for M^{best} induces a variation of 0.5% on the intensity maxima and a variation of ≈ 400 nm ($\approx$ twice the microscope resolution for the smallest z_1) in the evaluation of the test structure size dimension. Therefore it seems reasonable to take $\delta_M / M \approx 4\%$, that corresponds to an error of about 50 µm on z_1^{best}. Again, once fixed this best estimation z_1^{best}, one can use it as a "starting position" and reaches all the others z_1 positions using the motorized sample alignment stage. This is the procedure used to evaluate the distances and corresponding magnifications for the test pattern measurements presented in chapter 5.

4.5 Characterization of the guided beam

In order to test the fabrication process described in the previous chapter and to control the quality of the produced devices, some analysis on the WG exit beam are necessary. Sufficiently far from the WG exit ($>> d_{ex}^2 / \lambda$, where d_{ex} is the WG exit gap dimension), the intensity at the detector can be considered as the Fourier transform of the intensity at the exit aperture of the WG. In Fig. (4.3a) the measured intensity pattern for an air-gap WG with Si

claddings without pre-reflection at the entrance is reported in the case of coherent illumination of the entrance gap (see equation (2.30)). The intensity distribution $I(\theta_i, \theta_{ex})$ is presented in the coordinate system where the abscissa θ_i is the grazing-incidence angle of the incoming beam and the ordinate θ_{ex} is the exit angle of radiation at the terminal part of the WG. One can see a swallow-tail-like distribution with bright spots in correspondence of the resonant condition $\theta_i = \theta_m$ arranged along two lines separated by an exit angle which is $\theta_{ex} = \theta_i(1 \pm d_{in}/d_{ex})$ [Bukreeva, 2010] where d_{in} is the entrance gap dimension and d_{ex} the exit gap dimension of the WG (in the case of a constant-gap WG $d_{in} = d_{ex}$). In Figs.(4.3b) and (4.3c) the procedure for the estimation of the corresponding exit gap dimension is reported. The diffraction pattern from the coherent illuminated WG (Fig.(4.3a)) is anti-Fourier transformed (Fig.(4.3b)). It can be shown that Fig.(4.3b) represents the autocorrelation function of the WG exit field and that its wide in correspondence of the first resonance (Fig.(4.3c)) is roughly twice the exit gap dimension (see appendix 2).

In Figs. (4.4) the calculated patterns for air-gap WGs with Si claddings and pre-reflection at the entrance are shown in the case of coherent illumination of the entrance gap for three different values of the ratio $\Omega = d_{in} / d_{ex}$. These calculated diffraction patterns are taken from the work by Burkeeva et al. [Burkeeva, 2010]. It is worth noting that in the case of FC-WGs with pre-reflection at the entrance negative incident angles are not allowed and hence the corresponding non-zero intensity incident angle range is half the case of FC-WG without pre-reflection at the entrance.

In Figs. (4.5) some measured diffraction patterns from different fabricated devices are reported. Also in these cases a coherent illumination of the WG entrance gap is realized.

The case of an incoherent illumination for a no-tapered WG is reported in the calculations of Fig. (4.6). It is easy to note that the visibility of the "resonances" spots is degraded with respect to the previous cases. As reported in section 2.5, for the same WG, it depends on the value of the coherence length of the incoming radiation with respect to the WG entrance gap dimension. If one assumes a Gaussian shape for the MI the coherent illumination of the entrance gap is reached if equation (2.29) (or (2.30) for WGs without pre-reflection at the entrance) is satisfied, i.e. if the source is far enough from the WG entrance gap, but in general
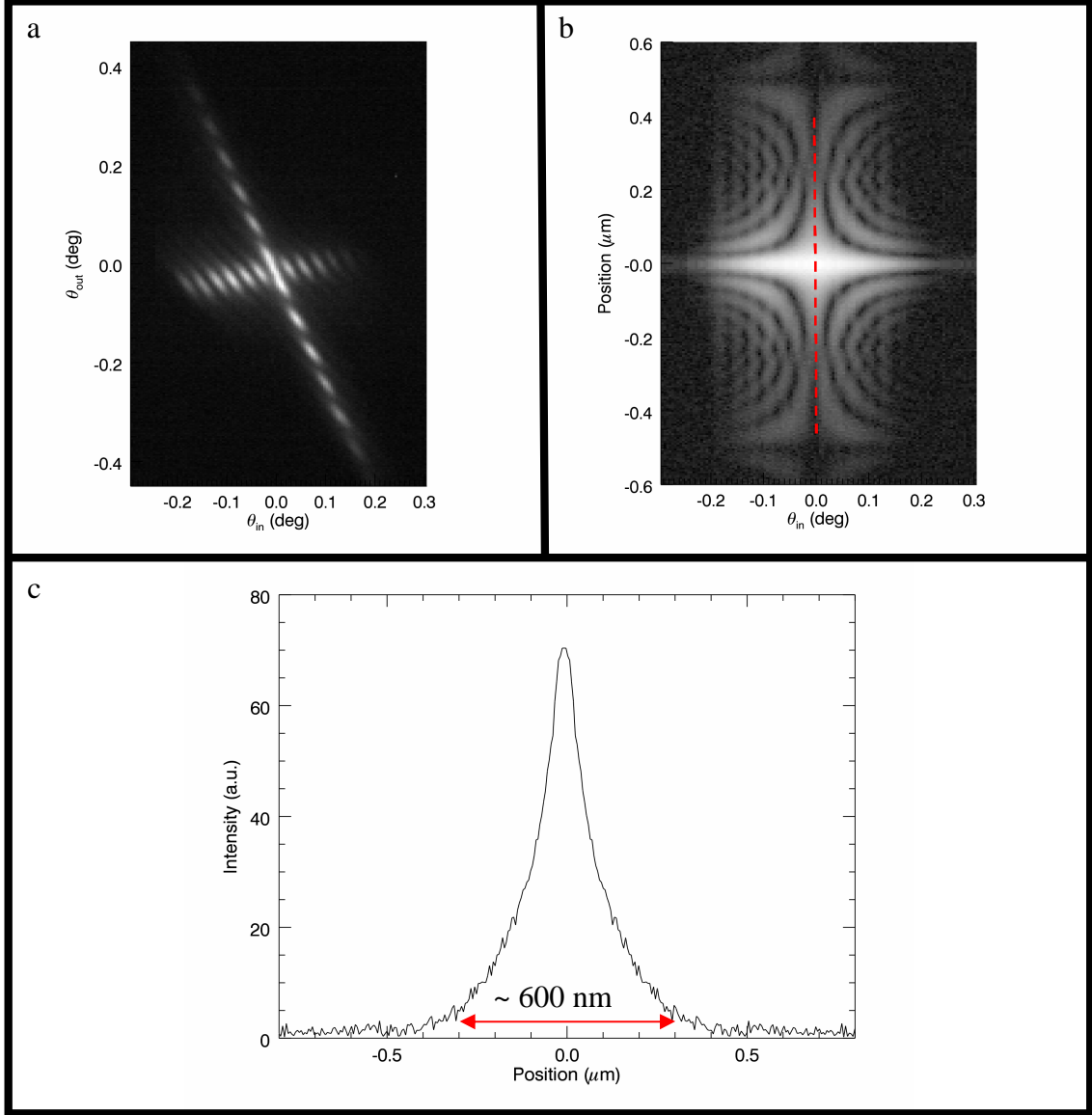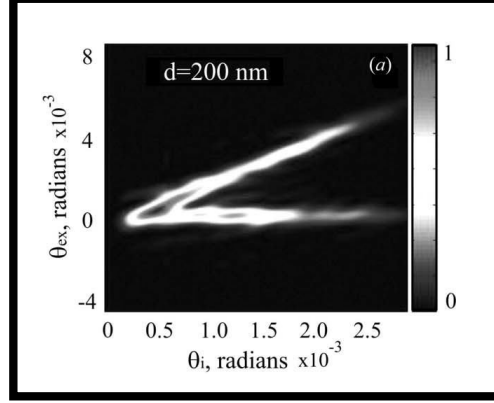
Figure 4.3*: a) Measured diffraction pattern from a Si vacuum gap WG. The entrance gap is coherently illuminated and the resonances spot are clearly visible. b) Autocorrelation function of the WG field obtained by the Inverse Fourier Transform of the measured diffraction pattern. c) Cross section of the autocorrelation function in correspondence of $\theta_{in}=0$ (first resonance angle, red dashed line in Fig.(4.3b)). The corresponding wide is about twice the physical dimension of the WG rectangular exit gap (see appendix2). In this case angles are reported in degrees. The obtained value is in accord with the thickness of the evaporated Cr shoulders (see the fabrication process described in the previous chapter).*
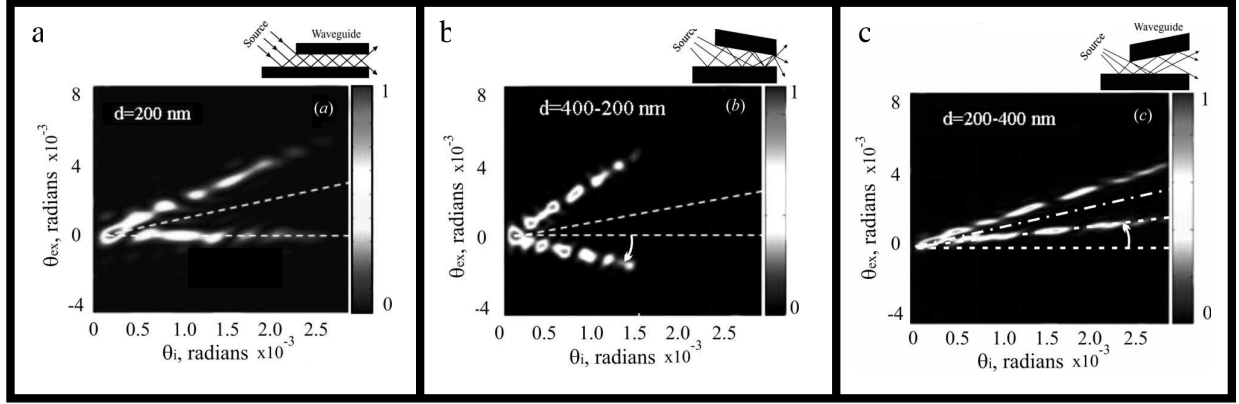
Figure 4.4*: Simulated diffraction pattern from a vacuum-gap Si WGs with pre-reflection at the entrance and (a) constant-gap,(b) converging-gap and (c) diverging-gap. The length of the WGs is L = 4 mm. The indicated parameter Ω is defined as d_{in}/d_{out}. The reported simulations are taken from the work by Inna et al. [Bukreeva, 2010].*
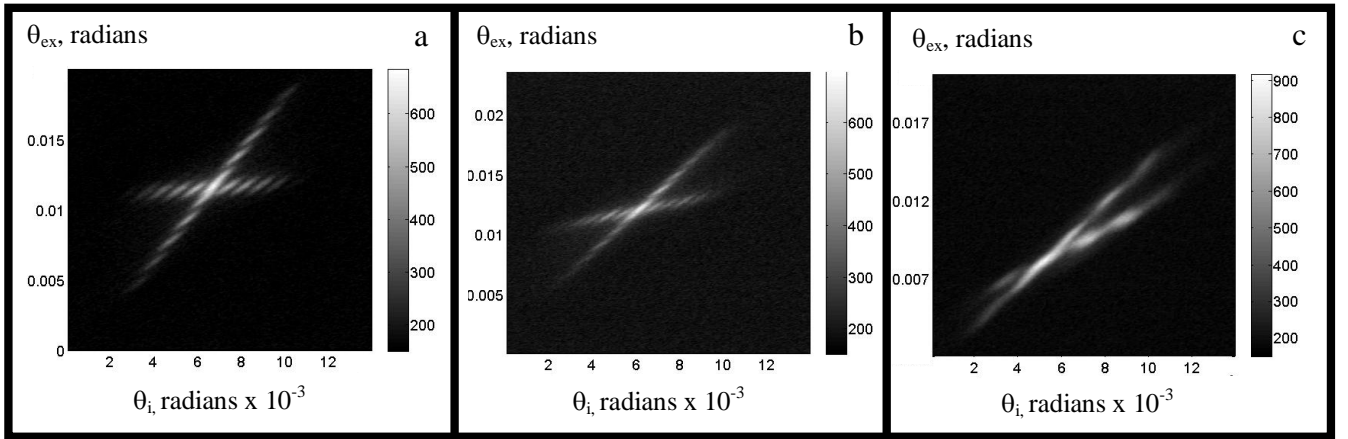

Figure 4.5*: Measured diffraction pattern from a vacuum-gap Si WGs with (a) constant-gap ($\Omega\sim1$), (b) diverging gap ($\Omega<1$), (c) and very diverging gap ($\Omega<<1$).*

Figure 4.6: *Simulated diffraction pattern from a no-tapered WG ($d_{in}=d_{ex}=d=200$ nm) in the case of inchoerent illumination of the entrance gap. A strong mode mixing makes the resonances spots almost not visibles.*

the value of coherent length at the WG entrance gap is not a monotone function of the source – WG entrance distance. Interesting this is the case we had observed experimentally.

The diffraction patterns from the same WG for different primary source-WG entrance distance z_s ($z_s=$ …) are reported in Figs. (4.7a-c). The respective intensity oscillations along one of the two tails are reported in Figs. (4.7d-f). In Fig. (4.8) the measured average value for the fringes visibility as a function of z_s is reported. The resonance spots visibility do not simply increases with z_s but presents an oscillation. This fact is predictable from van Cittert-Zernicke theorem if one assumes for the source intensity distribution function a truncated shape. In particular it is possible to show that for the simple case of a step function, one will obtain a sinc function [Attwood, 1999]. Therefore the coherence length stops to be a linear function of the source-WG entrance distance and will start to oscillate. The method used here to characterize the coherence length of the primary laboratory source on a generic plane with respect to a particular length scale (the WG entrance gap dimension) could be the starting point for the implementation of a WG-based interferometer for the characterization of the coherent properties of the beam from a laboratory X-ray source, for which the common values
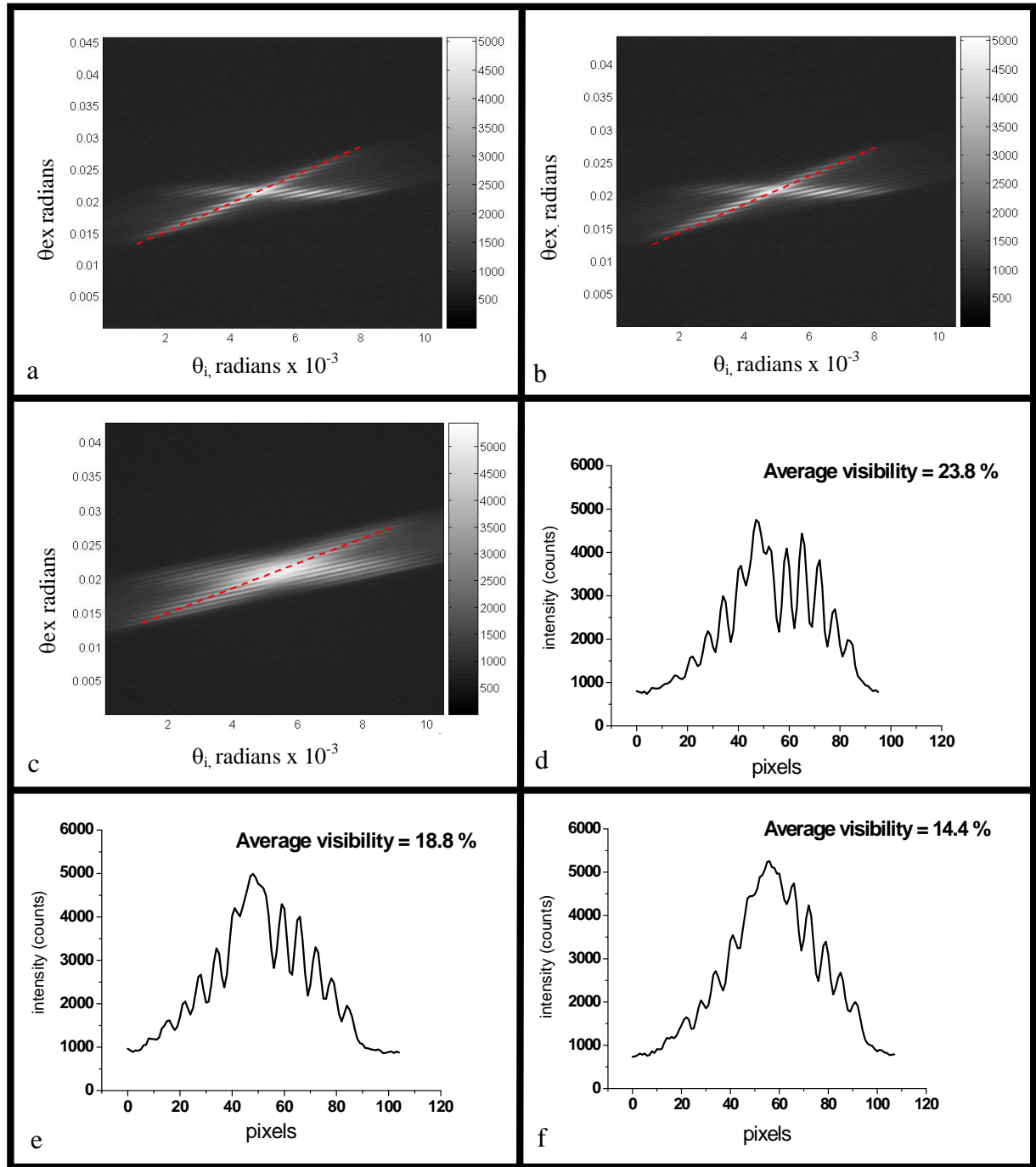
Figure 4.7*: a-c) Diffraction patterns from vacuum-gap Si WG for different primary source - WG entrance distance z_s : a) $z_s = 2.9$ cm b) $z_s = 1.9$ cm c) $z_s = 1$cm. d-f) Corresponding intensity oscillations along one of the two tails (as indicated by the red dashed line).*

for the coherence length at few centimeters from the source itself are usually $< 1\mu m$. The results shown in Fig. (4.8) suggest that the best source-WG entrance, among the choosen distances, distance is $z_s \approx 3$ cm because it correspond to the best compromise between intensity and coherence length at the WG entrance.
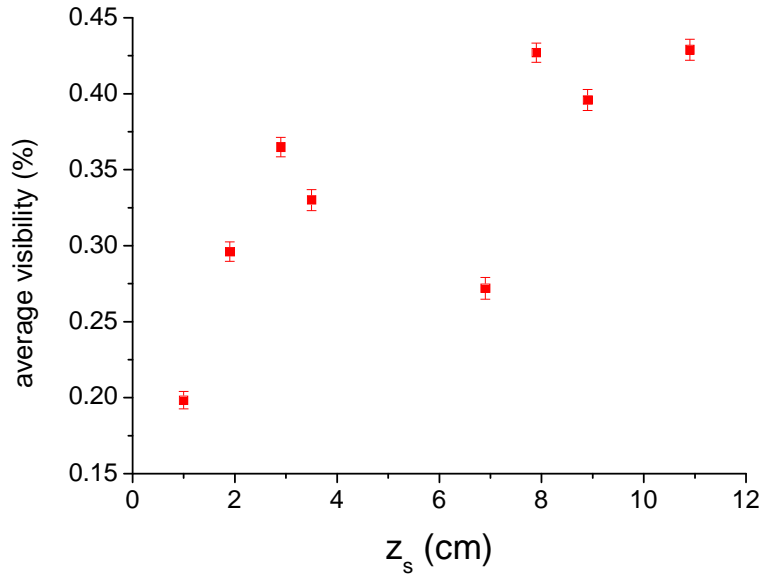
Figure 4.8*: Average visibility of the resonance spots as a function of the primary source- WG entrance distance z_s. The error bar are calculated propagating the error on each measured intensity ($\propto 1/\sqrt{N}$) on the visibility (see expression (1.46)) by the use of the standard propagation theory.*

In order to estimate the source MI function using the van Cittert-Zernicke theorem, the measurement shown in Fig. (4.8) has to be improved by incrementing the number of the z_s distances at which the measurement of the visibility is realized.

4.6 Coherent illumination of the waveguide entrance and resolution

The optimization of the distance z_s was explained before. It has to be chosen to have the coherence length of the impinging radiation large enough to realize a coherent illumination of the WG entrance gap. Otherwise many angles will be selected, with a consequent considerable degradation of the WG beam coherence which leads to an effective deterioration of the spatial resolution (1.65) as explained in section 1.5.5. Now the experimental demonstration of this fact is reported.

Two imaging measurements were realized using the WG based microscope on an Au test structure made up of five gold stripes. The used WG was a FC-WG without pre-reflection with a 300 nm gap (it is the WG analyzed in the measurements of Figs. (4.3), (4.7) and (4.8)) . The gold stripes of the test structure are 580 nm thick, 1.08 µm wide and separated one from each other by 810 nm. A SEM image of this structure is reported in Fig.(4.9a). The description of the gold test pattern fabrication process can be found in appendix 1. Together with the measurements, a numerical calculation was realized for comparison. The gold test structure was imaged using the same $z_1 + z_2$ and z_1 distances but two different primary source - WG entrance distances z_s (look at Fig. (4.1)). The corresponding intensity profiles and numerical calculations are reported in Figs (4.9b) and (4.9c).

In both cases the image of the test pattern is acquired with $z_1 = 1,2$ mm and $z_1 + z_2 = 269$ mm and hence a magnification equal to 224. The acquisition time was 100 s. At this z_1 distance the effective field of view was about 1.5 µm and a scan of the structure in the WG beam was necessary. Therefore each measured intensity profile (red dots) is the result of a collage of nine intensity profiles. Moreover, in order to minimize the effect of the microscope instabilities, each intensity profile was obtained as the average of 5 intensity profiles: $I = \sum_{i=1}^{5} I_i / 5$. Moreover each single intensity I_i was obtained integrating the corresponding normalized and background corrected measured intensity on the detector on 20 pixels in the vertical direction. More details about the data analysis will be reported for analogous measurements presented in chapter 5.

In the first measure (Fig.(4.9b)), $z_s = 3$ cm and the WG entrance gap is coherently illuminated. In the second measure (Fig.(4.9c)) $z_s = 1$cm and then the WG entrance gap is incoherently illuminated. The simulation program (see section 1.5.6) take into account the finite resolution of the microscope using equation (1.65), i.e. assuming an incoherent source of dimension s. Interesting, the optimal agreement with the calculations is obtained for s = 200 nm in the first case (coherent illumination of the entrance gap) and for s = 300 nm in the second case (incoherent illumination of the entrance gap). In this last case many modes are simultaneously excited and the source can be considered almost incoherent. Therefore equation (1.65) which is, as reported in section 1.5.5, strictly valid only for incoherent sources, can be used with s = 300 nm, which is the physical dimension of the exit gap (see the measurement reported in Figs. (4.3)). In this case the accordance with the experimental data is almost perfect. Moreover, in the case of coherent illumination of the WG entrance gap, Fig. (4.9b) shows that equation (1.65) and the corresponding model described in section 1.5.5 can be still used but with an efficacy value $s' = 200$ nm $< s$. In this case the accordance is not perfect but still good.

This results experimentally prove that the (partially) coherence of the WG beam which one can obtain with the coherent illumination of the entrance gap, leads to an effective improvement of the microscope resolution.
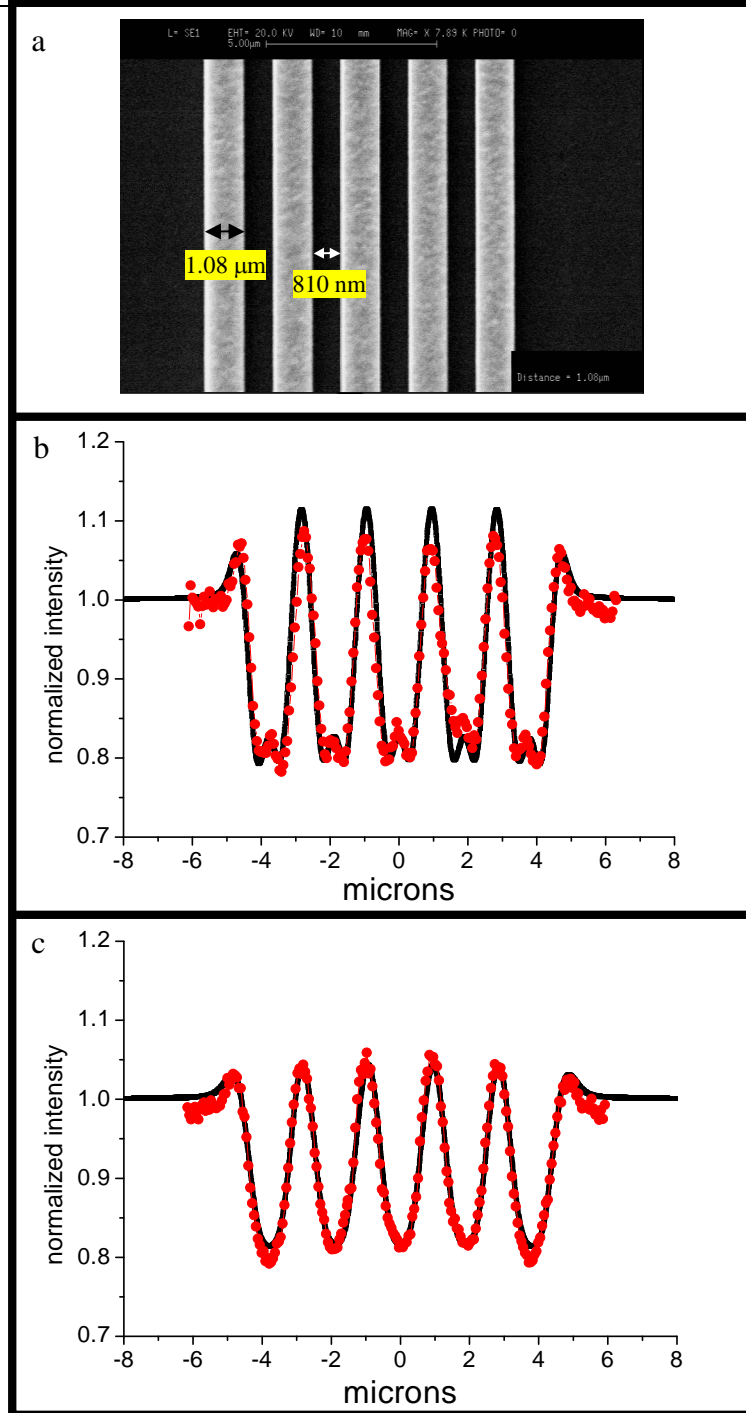
Figure 4.9*: a) SEM image of the Au test structure. b) measured intensity profile (red dots) in the case of coherent illumination of the WG entrance gap over imposed with the calculation (black line) with s = 200 nm c) measured intensity profile (red dots) and corresponding calculation (black line) for the case of incoherent illumination of the WG entrance gap. In this case the optimal accord with the calculation is obtained using s = 300 nm, which is the estimation for the physical dimension of the WG exit gap reported in Fig. (4.7).*

5. Quantitative hard X-ray phase retrieval with laboratory sources

In absorption imaging a very simple and linear relationship exists between image contrast and the absorption coefficient (see section 1.3). On the contrary a simple connection between the real part of the index of refraction δ, or the phase shift φ (1.13) introduced by the sample, and the intensity in a phase contrast image does not exist. The problem to obtain the phase of the wave front from the measurement of the image intensity is a well known and common problem in optics. One of the earliest strategies proposed to solve such inverse problem has been *holography*, introduced by Gabor [Gabor, 1948]. A hologram is simply a propagation phase contrast image registered in the Fresnel or Fraunhofer region, where the phase effects, if visible, modulates the intensity distribution. A holographic reconstruction is a method which permits the extraction of the object transmission function phase and amplitude from the hologram.

High energy X-ray holography and other X-ray phase-retrieval techniques have become a subject of interest only recently with the advent of high energy synchrotron sources which provide the necessary coherence to image these phase effects and recover structural information from the scattered photons. It is expected that the advent of the X-ray free electron laser sources will stimulate further holography and any other coherent X-ray method. Nevertheless the cost and the accessibility of these facilities limit the applicability of these methods in fields such as medicine and industrial processing. As a consequence there is still need of transferring these methods in common laboratory setup.

In this chapter holographic reconstructions of a test object are presented. The reconstruction of the object transmission function in amplitude and phase is approached starting from phase contrast imaging measurements realized in the laboratory by the use of the WG. The presented results demonstrate the possibility to transfer X-ray coherent methods from large

synchrotron radiation facilities to common X-ray laboratories, thanks to the implementation of WG assisted imaging.

5.1 In-line holography fundamental concepts

Holography is a two-step wavefront reconstruction method. In the first step, a hologram is recorded on the detector because of the interference of the scattered wave by the object E_s and the reference (unscattered) wave E_R:

$$I_H = \left| E_s + E_R \right|^2 \tag{5.1}$$

If the two waves have nearly the same direction of propagation, one speaks of *in-line holography*. The interference pattern (5.1) contains information about the phase and amplitude distribution of the object. There is no difference between the terms "hologram" and "phase contrast image" here. However the term holography must be preferred if one wants to underline the possibility of quantitative reconstruction of the wavefront in the object plane. Moreover it is important to note, as reported in section 1.5.3, that in holography one uses only the information contained in the illumination cone of the impinging beam on the sample.

In the second step some suitable algorithm is applied to measurements in order to retrieve the object transmission function in amplitude and phase.

5.2 Experiment

In order to realize the holography reconstructions, two Au test patterns were imaged. The Au test patterns were fabricated with the procedure described in appendix 1. A SEM image of both the gold structures is reported in Fig. (5.1a) and (5.1b), marking the significant dimensions. In particular the period of the "big" structure is 1.890 μm and the period of the "small" structure is 965 nm. The total distance between the WG exit and the CCD detector $z_1 + z_2$ was fixed at 269 mm. The distance z_1 between the WG exit and the test sample was equal to 1.2 mm for the case of the "big" structure and to 1.7 mm in the case of the "small" one. In the following table the corresponding values for the Fresnel distance, Fresnel number, coherence length on the sample, magnification and spatial resolution (1.65) calculated using an effective dimension of the incoherent source equal to 200 nm, are reported:

Au structure	z_1 (mm)	D (mm)	D_F (mm)	N_F	l_c (μm)	M	r_{tot} (nm)
"big"	**1.20**	**1.19**	**23.2**	**19.5**	**0.92**	**224**	**210**
"small"	**1.70**	**1.69**	**6.0**	**3.6**	**1.31**	**158**	**230**

The measured intensity profiles (red dots) are reported in Figs. (5.1c-d) superimposed on the corresponding numerical calculations (black continuous line).

Due to the limited field of view on the sample plane at such small distances a scan of the sample in the WG beam was necessary to image the full sample. Therefore the measured intensity profiles reported here are collages of many intensity profiles. Moreover, in order to minimize the effect of the microscope instabilities (see section 4.3) each intensity profile is the average of five measurements: $I = \sum_{i=1}^{5} I_i / 5$. In Figs. (5.2) the principal steps done on each measurements in order to obtain the collages of Fig.(5.1c-d) are reported. The acquisition time for each measurements was 100 s. On these measurements an holographic approach reconstruction will be attempted using two different methods.
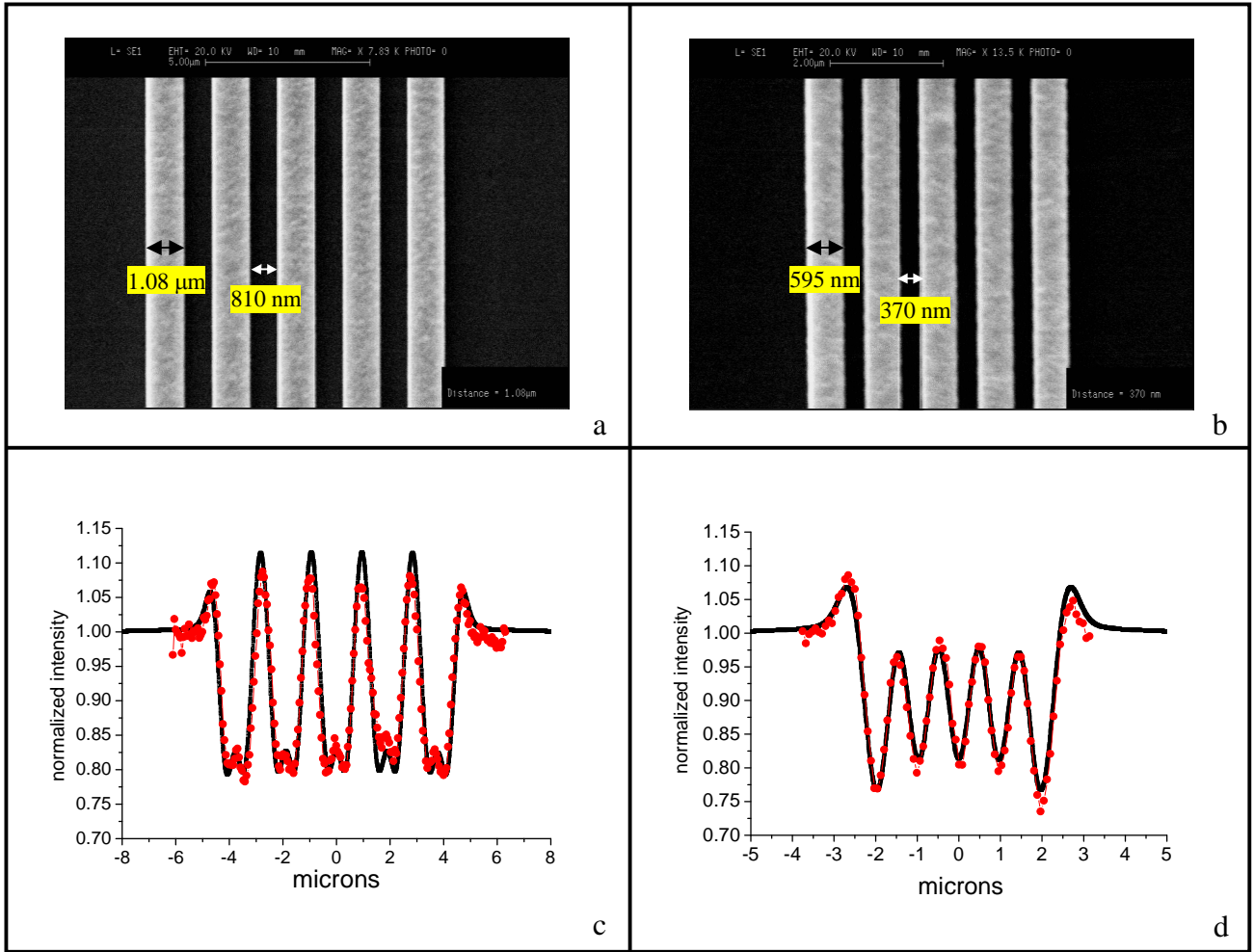
Figure 5.1: *a) and b) SEM images of the test structures with the significant distances. c) measured intensity profile (red dots) for the "big" structure at z_1=1.2 mm, over imposed to the corresponding analytical calculations (black continuous line). d) measured intensity profile (red dots) for the "small" structure at z_1=1.7 mm, over imposed to the corresponding analytical calculations (black continuous line). In both cases the horizontal axis are normalized respect to the correspondent magnification.*
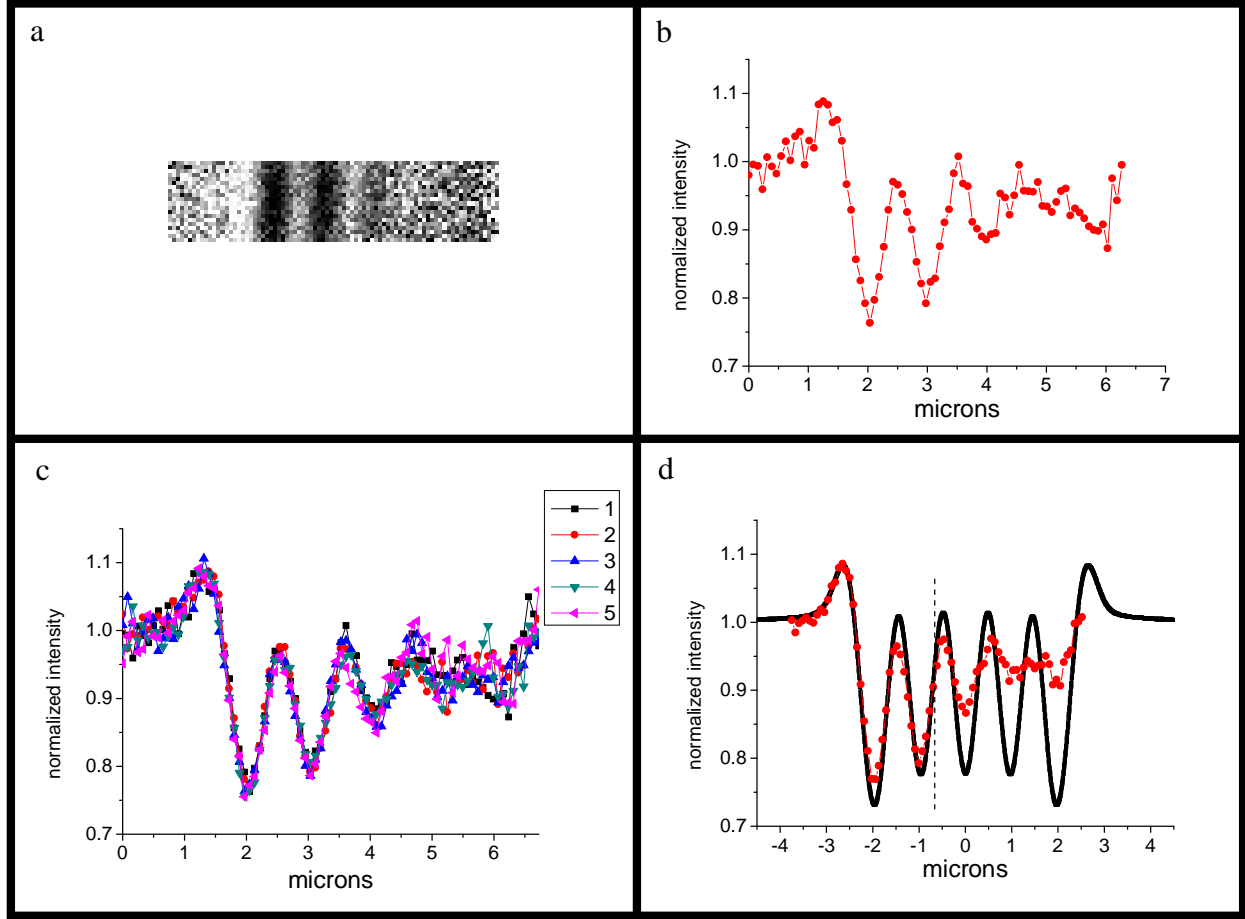
Figure 5.2: Example of data analysis. a) measured intensity as registered by the CCD camera, b) corresponding intensity profile obtained as the mean value in the vertical direction, i.e. on 20 pixels. c) five aligned intensity profiles from five identical measurements. d) average intensity profile (red dots) obtained from the profiles of Fig.(5.2c) over imposed with the corresponding calculation. The dashed line indicates where the measure was cut. It is the first step of the collage reported in Fig. (5.1d).
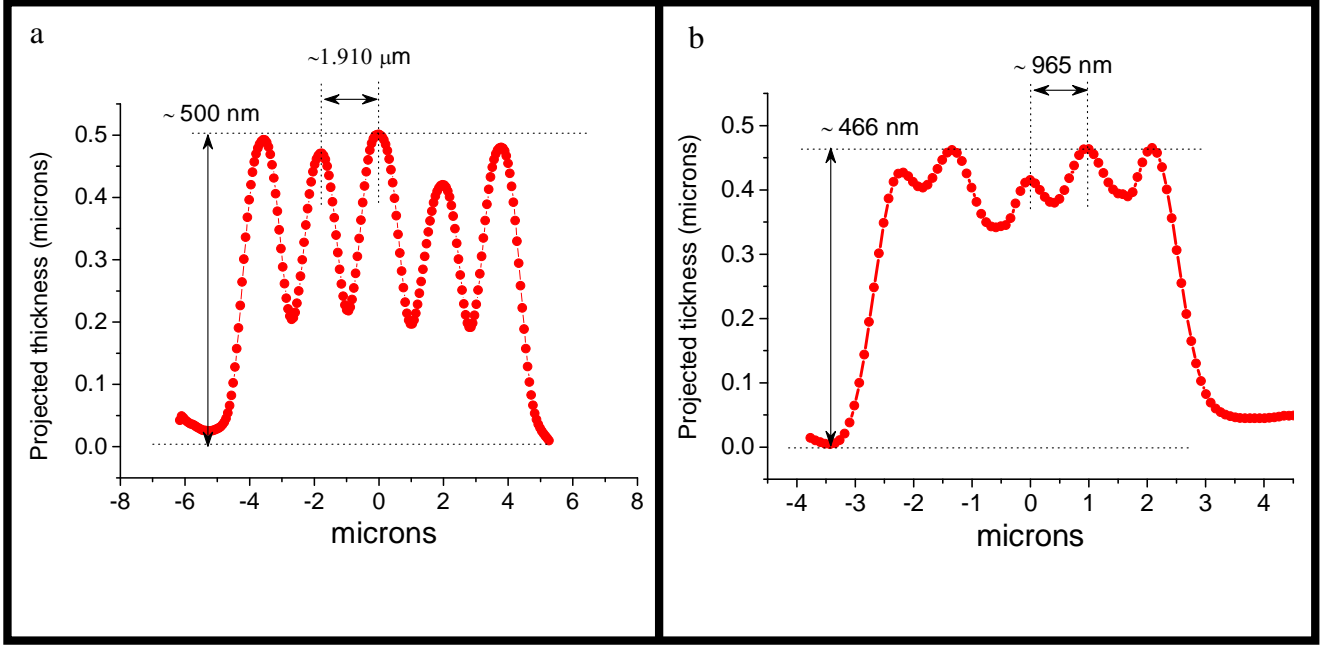
5.3 Reconstruction of the projected thickness

The method proposed by Paganin et al [Paganin, 2002] allows the simultaneous phase and amplitude extraction from a single defocused image of a homogeneous object. In this case the thickness of the sample in the transversal direction x respect to the optical axis z (see Fig.(4.1)) can be reconstructed. The expression used to calculate the thickness T(x) is:

$$T(x) = -\frac{1}{\mu} \log_e \left(F^{-1} \left\{ \mu \frac{F\left\{M^2 I(Mx, z_2)\right\}}{z_2 \delta \, k_x^2 / M + \mu} \right\} \right) \tag{5.2}$$

where μ is the linear absorption coefficient, F and F^{-1} indicates the Fourier Transform and the Inverse Fourier Transform respectively, M is the magnification, I is the measured normalized intensity, δ is the deviation from 1 of the real part of the refraction index of the homogeneous sample, z_2 the sample-detector distance and k_x is the conjugated variable to x.

In Figs. (5.3) T(x) is reported as obtained from expression (5.2) for the Au test patterns described in the previous section. The measured normalized intensities I used in equation (5.2) were the corresponding measured intensity profiles reported in Figs.(5.1). No *a priori* information on the samples has been used, except the assumption that both the test patterns are homogenous and mono-elemental. It is interesting to note that the periodicity of the used gold test structures is very well reconstructed in both cases (the error is ~10nm). The value of the reconstructed thickness is in both cases less than its true value, estimated from SEM equal to 580 nm. Moreover both the reconstructions produce a non-zero thickness also in the region between adjacent stripes. This is due to the limited resolution (~ 200 nm), which is in both cases comparable with the stripes separation distance (= 810nm and 370 nm, respectively). Naturally, the results for the "big" structure are more satisfactory. For further details on the method see [Paganin, 2002].

Figure 5.3: Projected thickness from expression (5.2) of the gold test patterns. a) Projected thickness reconstruction for the "big" structure. b) Projected thickness reconstruction for the "small" structure. In both cases the periodicity is very well reproduced but not the absolute value of the thickness.

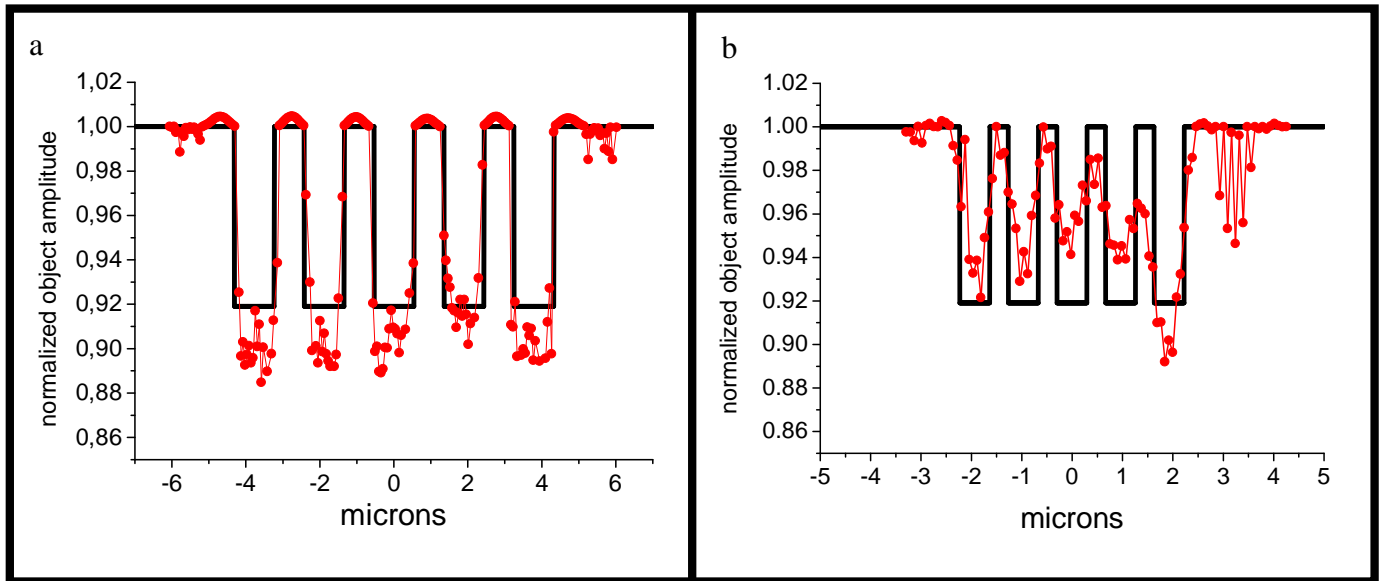## 5.4 Reconstruction using iterative phase retrieval method

The reconstruction of the object density from intensity acquisition under coherent illumination has been demonstrated by a number of authors. The pioneering works in this field were made by Sayre [Sayre, 1952], Gerchberg and Saxton [Gerchberg, 1972] and Fienup [Fienup, 1978; Fienup, 1982]. Impressive results were obtained in recent years ([Miao, 2002], [Robinson, 2003], [Williams, 2003]). Here the basic idea of the Gerchberg-Saxton algorithm is used on the measurements reported in Fig. (5.1c) and (5.1d). It is an iterative method that assumes that the object's extension in space is limited, so that the transmission function is only different from unity in a region called *support* of the object. One iteration step of the

algorithm is depicted in Fig. (5.4). The algorithm starts from the known measured normalized intensity as recorded by the detector (in our case, the used intensities are the ones in Fig. (5.1c) and (5.1d)). From the measured normalized intensity it is possible to calculate the amplitude of the wave field but not the phase, which is lost. In classic crystallography this is called *phase problem*. Therefore, an arbitrary phase distribution is associated to this calculated amplitude from the measured normalized intensity and the corresponding field is then back-propagated in object plane. In the object plane the support constraints are applied: the phase is set to zero and the amplitude to unity outside the support. This modified field is then propagated to the detector plane obtaining a new phase and amplitude distribution. Here the phase distribution is kept while the amplitude distribution is exchanged again with the known amplitude from the measured normalized intensity (which is the constraint in the detector plane). This circle of back-propagation, application of the constraints in the object plane (i.e. the support), forward propagation and application of the detector plane constraints (i.e. the recorded intensity) makes one iteration step and it is repeated until the reconstruction converges to a constant field distribution.
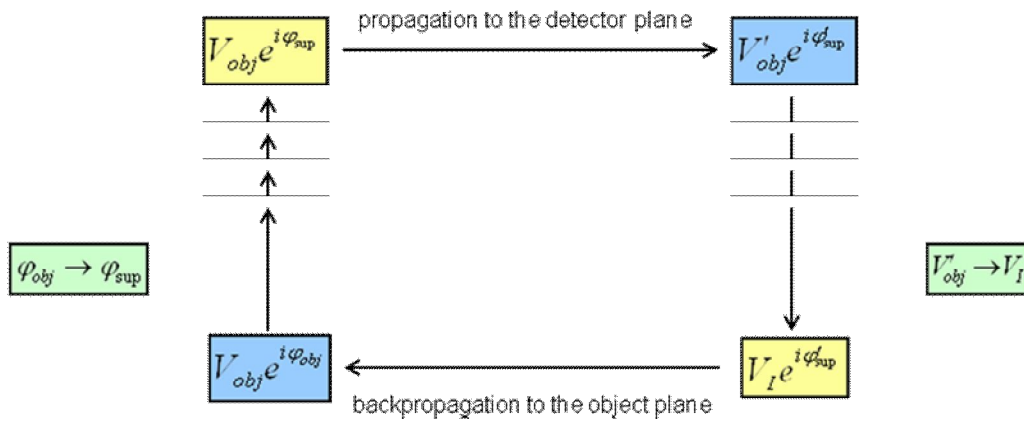
Figure 5.4: Conceptual layout of a generic step of the iterative phase retrieval algorithm used to obtain the holographic reconstructions reported in Fig. (5.5).

The original Gerchberg-Saxton algorithm was only defined for two function related to each other by a Fourier transform. Fienup generalized it to a wide class of transformations [Fienup, 1980; Fienup, 1986] like the particular case of the Fresnel transformation which is the case of interest here. The algorithm has been used to study the possibilities of high energy X-ray holographic reconstruction using iterative methods in a common laboratory by the implementation of the WG-based phase contrast microscope described in the previous chapter. In our experimental case, the corresponding reconstructions of the object amplitude are reported in Fig. (5.5a) and Fig. (5.5b) for the measured normalized intensity of Fig (5.1c) and (5.1d). It is important to stress that in this case the *a priori information* is not on the homogeneous composition of the test sample but on an estimate of its total dimension.

Figure 5.5: *Reconstructed object amplitude using an iterative phase retrieval algorithm on the measurements reported in Fig.(5.1c) and (5.1d) for (a) the "big" structure" and (b) the "small" structure. In both cases the reconstruction (red dots) is over imposed with the modulus of the ideal transmission function (black continuous line) used to calculate the simulated intensity profile of Figs.(5.1c) and (5.1d).*

In principle the algorithm requires a completely coherent beam on the sample and a beam dimension larger than the sample itself. As a consequence the algorithm for the phase retrieval does not converge to a significant result and the analogous reconstruction for the object phase cannot be accomplished.

5.5 Conclusions

As it is evident, the obtained holographic reconstructions cannot be considered completely satisfactory. The object transmission function cannot be reconstructed within a reasonable error with this experimental setup. Nevertheless the results obtained are able to reproduce some significant features of the test sample, at least qualitatively and are extremely promising in view of a better, optimized microscopy setup. Many improvements have to be made principally in two directions: on the computer codes which perform the holographic reconstruction starting from the measurements, in addition the measurement process it must be optimized, improving the stability and the efficiency of the geometry. Usually holographic amplitude/phase retrieval methods can be confidently applied when the coherence of the incoming beam is large enough and the sample is fully illuminated. Therefore artefacts in the reconstruction are reduced when the beam coherence is improved. In principle one can approach this situation increasing the primary source - WG entrance distance (z_s) and the WG exit-sample distance (z_1). As a consequence also the total distance z_1+z_2 should be increased, in order to exploit the magnification effect and to keep the resolution near its lower limit (see section 4.2). Then a problem of intensity produced from the primary source arises. Actually the presented measurements on a test sample are going to be repeated at the X-ray laboratory of the School of Physics at Monash University (Melbourne, Australia). Here the primary source is a Cu rotating anode with estimated brilliance equal to 10^{13} photons/s/mm^2/mrad^2/(0.1% bandwidth) at Cu-K$_\alpha$ radiation energy, four orders magnitude bigger than the standard microfocus source used till now. Therefore the mentioned distances could be increased and the object illumination conditions improved. This should bring to an improvement of the holographic reconstruction results reported above.

6. Investigation of human hair internal structure

The outermost layer of mammalian hair fibres is called cuticle. The cuticle protects the core of the fibre against physical and chemical stress and leads the hair appearance. For this reasons cuticle is a major concern for the textile and the cosmetic industries. The structure and some of the properties of the cuticle and of the whole hair fibre have been extensively studied by electron microscopy like TEM, SEM and AFM. However, these techniques require many chemical and invasive treatments. Therefore, there is still need for a less invasive structural probe. For this reason, x-ray phase contrast imaging experiments have been carried out on human hair samples using the x-ray WG based phase contrast microscope. After a brief overview of the hair structure and in particular of the cuticle structure (sections 6.1 and 6.2) the experiments motivations (sections 6.3) and the simple and non-invasive sample preparation (sections 6.4) will be pointed out. In section (6.5) the measurements results from the direct observation of a human hair cuticle scales is reported. In section (6.6) the imaging measurements on some whole hair shafts are reported and in section (6.7) the same hair sample before and after water sorption and colour treatment are compared. Finally in section (6.8) some conclusions about the potentialities of the used technique in studying the properties of the hair and especially of the hair cuticle are reported.

6.1 Human hair structure overview

Morphologically, a fully formed human hair fibre is 15-120 µm in diameter [Kaswell, 1953; Randebrook, 1964] (however, since the cross section of a hair is elliptical, the term diameter is not totally accurate [Bogaty, 1969]) and contains three different major units or structures, the medulla, the cortex and the cuticle. In Fig. (6.1) they are indicated in a schematic representation of the cross section of a human hair fibre. All these structures are composed of dead cells, which are mainly filled with keratin protein. Therefore hair is biologically dead and it receives no further assistance from the root which created it. In the central region of the hair is located the medulla. It is 5-10 µm in diameter and is composed of loosely packed cells leaving a series of vacuoles along the fibre axis. The cortex makes up the bulk of the hair strand and contains the major part of the fibre mass. It is a closely packed assembly of keratin micro fibrils aligned along the fibre axis. At the hair surface we find the cuticle, a 5-10 microns-thick protective covering consisting of layers of flat overlapping scale-like cells. Cortex and cuticle are present in all mammalians hair.
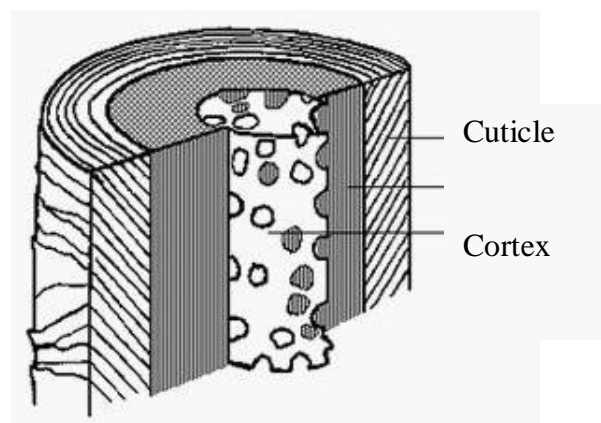
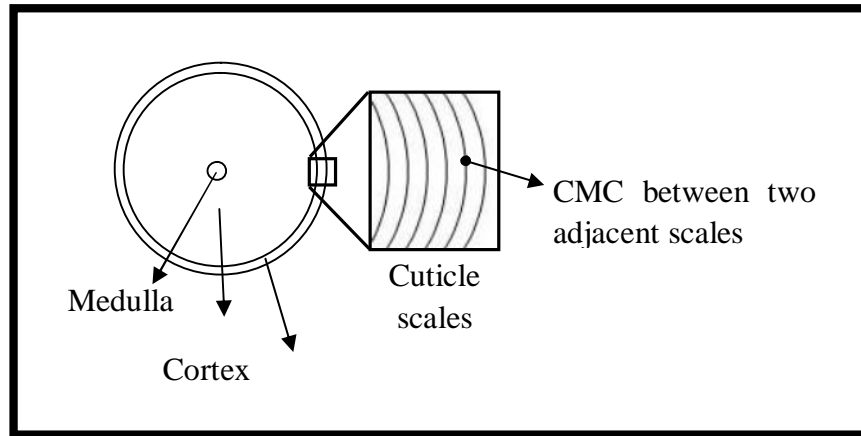*Figure 6.1*: *Schematic representation of the cross section of a human hair fibre.*

Finally, there are other two components that all the mammalians hairs have in common. In non-chemically damaged hair, the cuticle is covered by an invisible tiny layer of protective fatty acids sometimes called F-layer. The F-layer is water resistant: when wet, damaged hair with no F-layer can increase in weight by up to 200%, whereas virgin hair increases in weight by only 12-18% [Pantene web-site]. The other "lipid" component is the Cell Membrane Complex (CMC) that glues or binds the cells together both in the cuticle and in the cortex and, with other non-keratin components, forms the major pathway for diffusion into the fibres [Robbins, 2002].

6.2 Human hair cuticle structure

The cuticle is the fibre's external envelope. The flat overlapping cells forming it are called scales. They are stacked over each other and point forward the tip end of the hair fibre, like shingles on a roof so that the cuticle is made up of 3 (near the end of the fibre) to 10 (near the scalp) thicknesses of cells. Scales are colourless, 50 to 70 microns long, 5 to 10 microns wide and *no more than one micron thick* [L'Oreal web-site]. Each scale has a laminar sub-structure. The existing knowledge of this sub-structure derived from TEM investigation is summarized in the work by Swift & Smith [Swift, 2001].

It is important to note that between adjacent scales (see Fig.(6.2)), the CMC glues them together and it is, in turn, made up of three layers: two thin layers of lipids called β layers (3 nm thick) separated by the δ layer (roughly 18 nm thick) [Kreplak, 2001]. Interestingly, the inner and the outer β layers do not contain the same type of fatty acid and only the outer β layer seems to ensure smoothness of intercellular sliding between cuticle scales and it is identified as the weak point for cuticles delamination [Smith, 2005].

Figure 6.2: Another schematic representation of the cross section of a human hair fibre. The cuticle scales and the CMC between each scale are pointed out.

6.3 Experiment motivations

As reported before the hair appearance is leaded by the quality of its surface. A health cuticle with each scales well closed over each other and covered by the F-layer permit hair reflect light and shine and assure the protection on the fibre core. The success of a cosmetic product is based on the way it interacts with the biological substrate. Therefore know the structure of hair surface is important because it determines how hair interacts with hair care products. Moreover the starting hair structure affects the choice of ingredients for a formula, the levels of ingredients in a formula and the way in which the ingredients are deposited on the hair. Till now the principal way of investigation of human hair was electron microscopy techniques which show either surfaces (SEM and AFM) or very little thin films (TEM). They assure resolutions of few nanometres but imply complex and invasive sample preparation, especially for TEM and SEM investigation (see for example the "TEM methods" in [Swift, 2001] or the "experimental" section in [Smith, 2005]).

114

For their intrinsic penetration ability, X-rays allow a not destructive investigation of thick samples. While there have been some spectroscopic ([Merigoux, 2003]) or scattering studies ([Kreplak, 2001], [Busson, 1999], [Krepalk, 2002]) at synchrotron radiation facility, to our knowledge there is not any x-ray imaging results especially revealing, both at synchrotron radiation facility and in standard laboratory.

6.4 Sample preparation, experimental setup and methods

Fibre samples were mounted on the sample holder without any kind of preparation, just few minutes after the cutting from the scalp. This fact makes the realized measures very interesting respect to the precedent investigations based on electron microscopy techniques. The sample holder applies to the fibre a small tension, just the necessary to maintain it straight during the measure. The realized measures are PPCI measurements realized with the WG based microscope described in section 4.1. They are both measures on the air-hair edge (section 6.5) and scan measures on the bulk of the fibre (section 6.6 and 6.7). In this last case the hair was successively wet or coloured for a comparison by touching the hair with a wet or coloured tampon, without removing it from the sample holder.

As discussed in the previous chapter, the WG based microscope configuration which leads to the best resolution corresponds to choose z_s such that $l_c > d_{gap}$, i.e. a coherent illumination of the WG entrance gap and $z_1 << z_2$. Fixed the total distance to $z_1 + z_2 \approx 270$ mm, $z_1 << z_2$ means z_1 on the orders of few millimetres (i.e. as small as possible in compatibility with the sample holder encumbrance). At such small z_1 distance the effective horizontal field of view on the sample is very small, on the order of few microns (refer to Fig. (4.1) for the distances). In order to improve the field view, an incident angle slightly different respect to the first resonant angle was selected ($\Delta\theta_{in} \approx 5 \times 10^{-4}$ rad). In this way the two guided beams, perfectly over imposed in the first resonance, starts to separate one from each other, leading to an effective improvement in the field of view on the sample. This choice increments the mode

mixing in the WG beam with a consequent degradation of the produced beam coherence, but, in this "microscopy modality", the benefits of a "large" field of view on the sample were evaluated more important than the coherence properties of the beam. The opposite choice has been made in the previous chapter, where the coherence properties of the beam on the sample are essential in order to reconstruct the object transmission function.

## 6.5 Direct observation of cuticle scales

Fig. (6.3a) shows the phase contrast image of the air-hair edge as registered by the CCD camera. As usual, the registered intensity is normalized respect to the incident beam and background corrected. The exposure time is 100 s. The WG-hair distance is $z_1 = 2$ mm and the total distance WG-CCD is $z_1 + z_2 = 269$ mm. The corresponding magnification (1.34) was $M \approx 134$ and the estimation for the horizontal spatial resolution (see expression (1.65)) is $r_{tot} \approx 200$ nm. The defocusing distance (1.32) is $D \approx 2$ mm, $< D_F$ if details of the order of $1 \mu m$ are assumed. In Fig. (6.3b) the corresponding intensity profile (red dots) is reported. It is obtained by integrating the registered intensity in the vertical direction. A calculated intensity profile is over imposed for comparison (black continuous line). The simulated object transmission function is reported in Figs. (6.3c) and the correspondent significant distances and values for the real and imaginary part of the refraction index in the scheme of Fig. (6.3d). In this model the "secondary" intensity oscillations, i.e. the intensity oscillations after the principal one due to the air-hair transition, are supposed to be produced by a step-like refraction index variation with a periodicity on the order of 1.4 µm. The used values for the refraction index are compatible with the keratin dominant composition of the hair fibre.
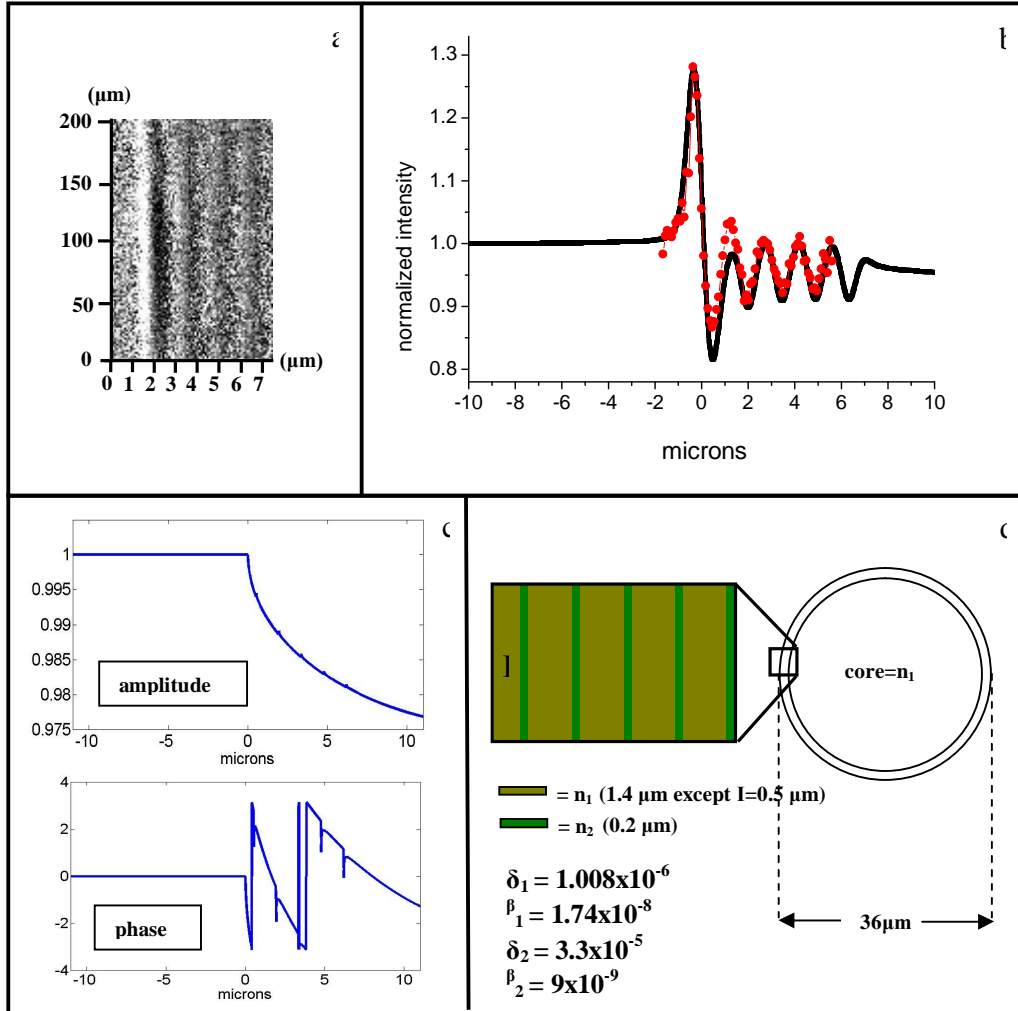
Figure 6.3*: a) Phase contrast image of the air-hair edge as registered by the CCD camera. The vertical and the horizontal axis are normalized with respect to the corresponding magnification (M=7.3 and M=134, respectively). b) Corresponding intensity profile (red dots-measure; black continue line- calculation). The horizontal axis scale is normalized with respect to the horizontal magnification (M=134).The estimated resolution is 240 nm. c) Amplitude and phase of the object transmission function. The projection approximation is assumed. d) Scheme of the simulated object. The significant distances and the values of the real and imaginary part of the simulated refraction index are reported.*

A number of hair samples from two different individuals were imaged with similar parameters, showing that the technique allow an immediate visualization of the hair cuticle scales alignment quality. Some examples are shown in Figs. (6.4). It is worth noting that in the same hair it is possible to find both regions with a good quality and regions with a bad quality of the cuticle scales alignment.
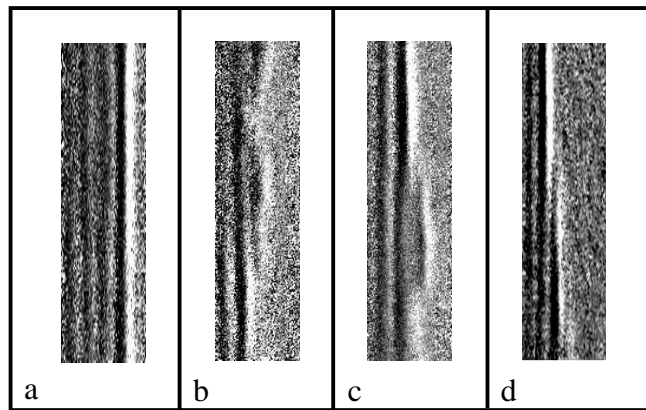

Figure 6.4: *Qualitative evaluations of hair edge. a) Hair edge with a good quality of the cuticle scales alignment. b) and c) bad quality of the scales alignment. d) edge transition region from one scale to another. The tip end of the outer scale can be recognized in the middle of the recorded image.*

6.6 Direct observation of the human hair shaft

In order to image the full hair shaft, the scan of the hair sample in the WG beam is necessary. The scan step dimension and the exposure time for each step are respectively 3 μm and 100 s. From each intensity profile a 3 μm wide (normalized with respect to the magnification) column is cut and used to compose a collage of images. In Fig. (6.5a) the collage corresponding to the hair sample of the measurement reported in Fig. (6.3) is shown. The corresponding intensity profile, obtained integrating the registered intensity distribution in the vertical direction is reported in Fig.(6.5b). It is interesting to note that far from the hair-air

interface ("principal edge") the fringes become less and less visible and at about 10 μm from the principal edges one can suppose to enter in the cortex zone. This fact is more evident in the scan measure reported in Fig. (6.6). In this case the recording distances are $z_1 = 4$ mm and $z_1 + z_2 = 292$ mm. The corresponding horizontal magnification is $M \approx 73$ and the estimation for the horizontal spatial resolution is $r_{tot} \approx 310$ nm. The scan parameters were the same as above. The change in the visibility of the intensity oscillations at about 10 μm (dashed line) from the principal edges is clearly visible. Moreover around the central part one can distinguish another edge indicated by the arrows, corresponding to a diameter on the order of 5 μm, probably due to the presence of the *medulla*.
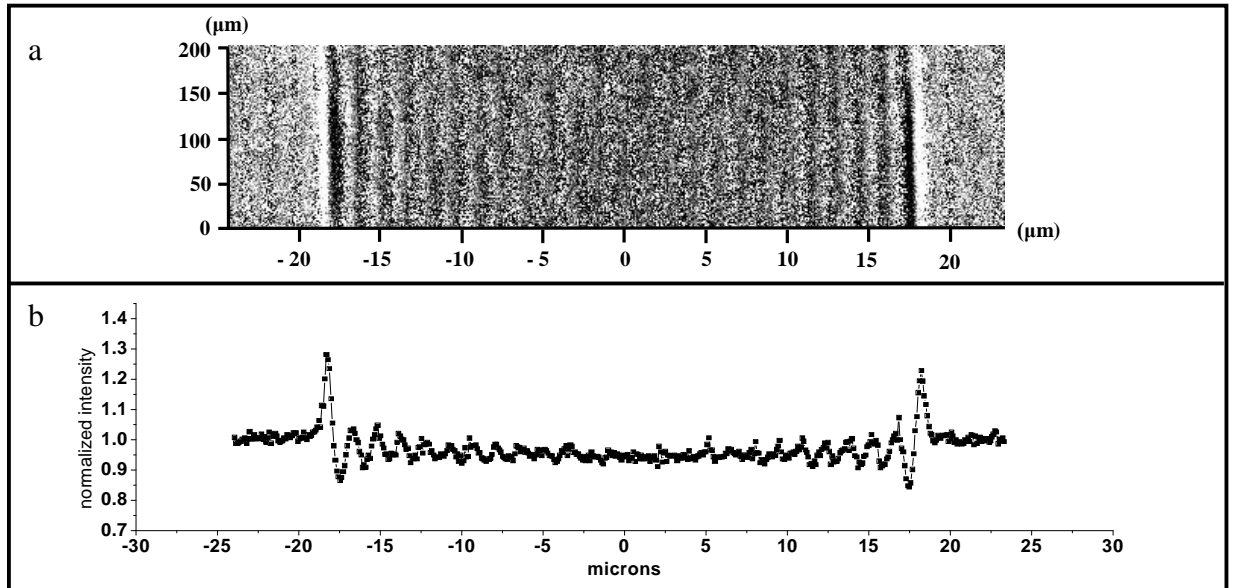
Figure 6.5: *a) Human hair shaft as collages of acquired images by the CCD camera. The recording distances and the acquisition time for each step of the scan was the same of the single measure reported in Fig.(6.3). The vertical and the horizontal axis are normalized with respect to the respective magnification (M=7.3 and M=134, respectively). The single image of the collage has 3x200 μm normalized dimensions. b) Corresponding intensity profile, obtained integrating the CCD intensity collage in the vertical direction (120 pixels).*
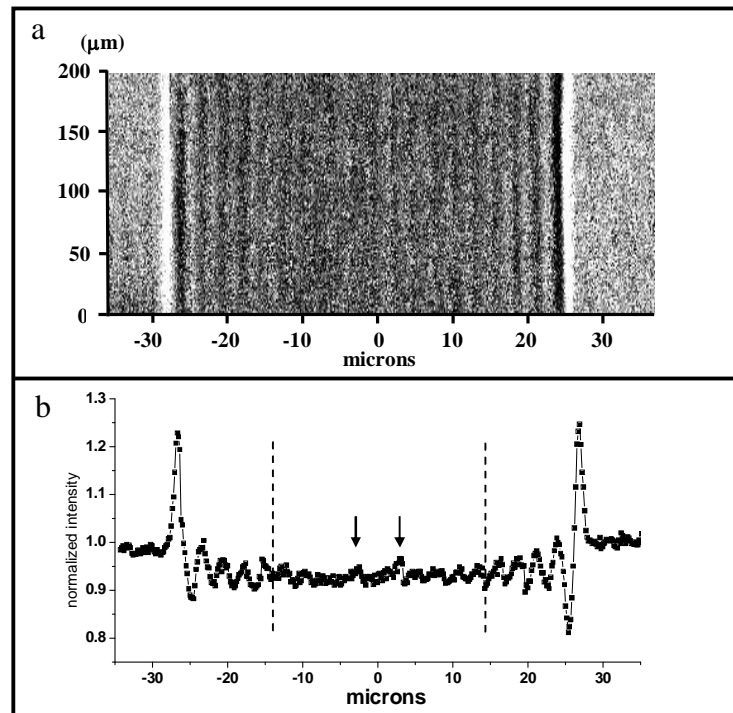
Figure 6.6: a) Human hair shaft as collages of acquired images by the CCD camera and b) corresponding intensity profile (M=73, resolution≈ 310 nm). The change in the fringes structure possibly due to the transition cuticle-cortex at about 10 microns from the principal edges is indicated by the dashed lines. Moreover around the central part it is possible to distinguish another edge indicated by the arrows, corresponding to a diameter on the order of 5 μm, probably due to the presence of the medulla.

6.7 Direct observation of hair swelling

Swelling studies were performed extensively on the human hair fibre. In particular hair swelling assessments have been extremely valuable for providing information about chemical alterations to human hair [Robbins, 2002]. For example Klemm et al. [Klemm, 1965] have described a swelling test to assess hair damage by permanent waves and bleaches.

120

In general the problem can be simplified asserting that a an health and "virgin" hair (virgin respect to cosmetic treatments) has its cuticle scales well closed over each other and covered by the lipid and water resistant F-layer and then will not allow the penetration of water or other solutions in the inside of the fibre. Some quantitative evaluations are reported in [Pantene web-site]: when wet, damaged hair can increase in weight by up to 200%, whereas virgin hair increases in weight by only 12-18%. It is obvious that swelling studies cannot be approached with electron microscopy techniques. In order to demonstrate the possibility to realize such studies with the WG based microscope, the observation of the water swelling of an hair fibre was measured both for a virgin hair and for a many years-chemically treated hair. In Figs.(6.7) the collage and the corresponding intensity profile are reported just before (Fig. (6.7a)) and after (Fig. (6.7b)) the water absorption by the many years-chemically treated hair ($z_1 = 3.2$ mm, $z_1 + z_2 = 269$ mm, horizontal magnification $M \approx 84$ and spatial resolution $r_{tot} \approx 290$ nm, exposure time for each scan step 100s). The measured percentage increment of the diameter dimension due to the water absorption is $\approx 40\%$ (from 45.5 µm to 64 µm). The same kind of measure for the virgin hair is reported in Figs. (6.8). In this case the measured increment in the diameter dimension is only $\approx 3.5\%$ (from 35.9 µm to 37.2 µm). As expected the virgin hair is quasi water resistant. On the contrary the "ruined" hair allow water to penetrate into the fibre core very easily. It is worth noting that in both cases the edge fringes dimension and visibility remain close to the value before the water absorption. The quantitative measurement of this fact for the ruined hair is reported in Figs. (6.7c) and (6.7d). This is in accord with the hypothesis that the water pass through the CMC between adjacent cuticle scales without modify their structure.

In order to prove the same behaviour for colorant cosmetic products, the measurements were repeated both on a ruined and virgin hair using a red colorant cosmetic solution of a famous trademark. The same results have been reached: the diameter of the virgin hair remain almost the same while the ruined hair diameter increment its dimension (from 51 to 69 µm, $\approx +35\%$): also the colorant solution penetrates into the core of the ruined hair. Moreover in this case the first edge fringe, i.e. the fringe that corresponds to the transition air-hair, changes its visibility. On the contrary, the "inner" edges fringes remain almost the same. The corresponding quantitative measurement of this fact is reported in Figs. (6.9).
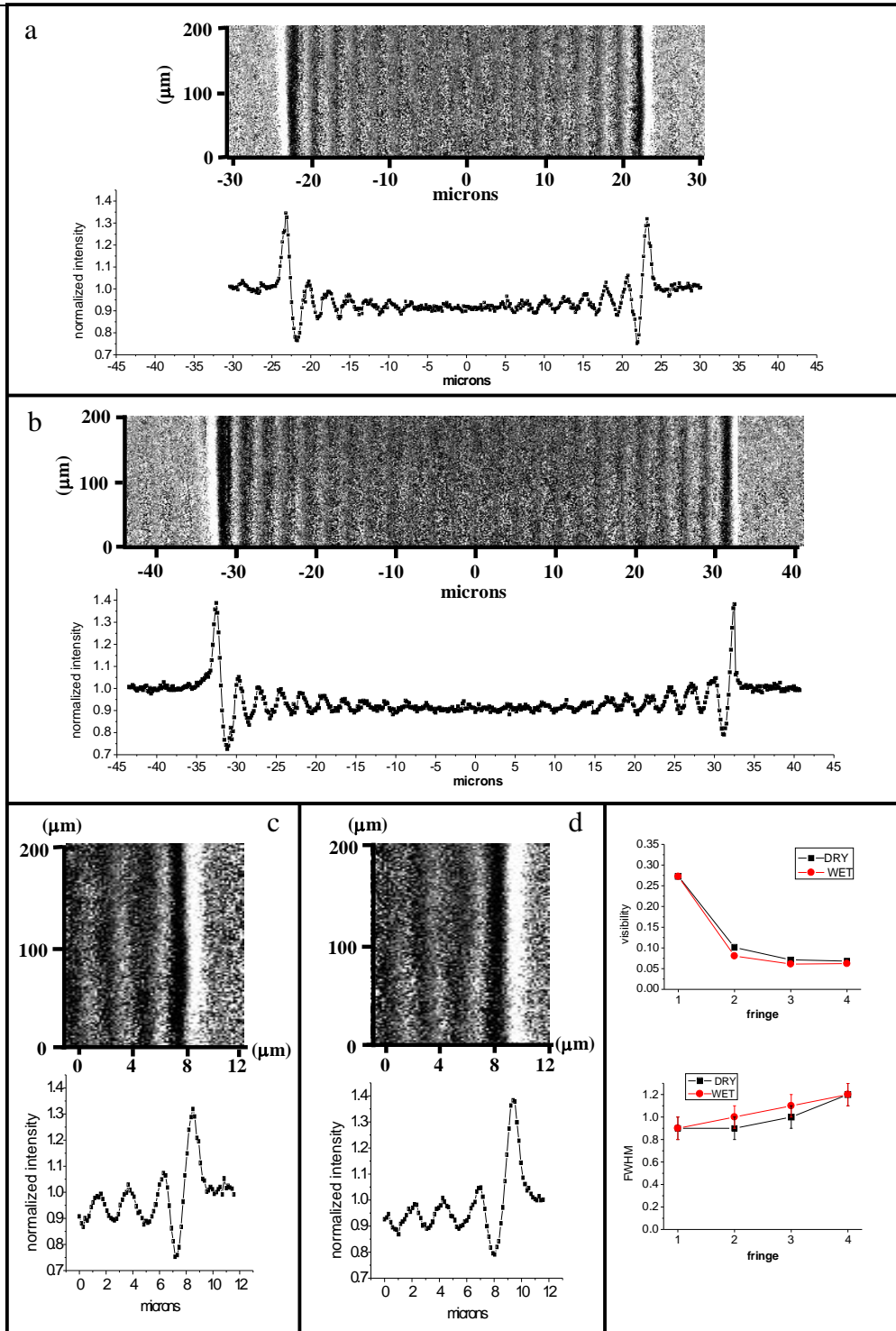
Figure 6.7*: Water sorption from an hair ruined by many years of cosmetic treatments. a) Hair shaft as collages of acquired images by the CCD camera and its corresponding intensity profile before the water sorption and (b) after the water sorption. c) Edge fringes from a single measurement before the water sorption and (d) after the water sorption. e) quantitative evaluation of fringes visibility and FWHM for the dry and the wet case (black dots and red dots respectively).*

Probably, part of the colorant solution remains on the hair external surface and therefore the refraction index variation in correspondence of the air-hair transition becomes less steep, with a consequent reduction in the corresponding fringe visibility.
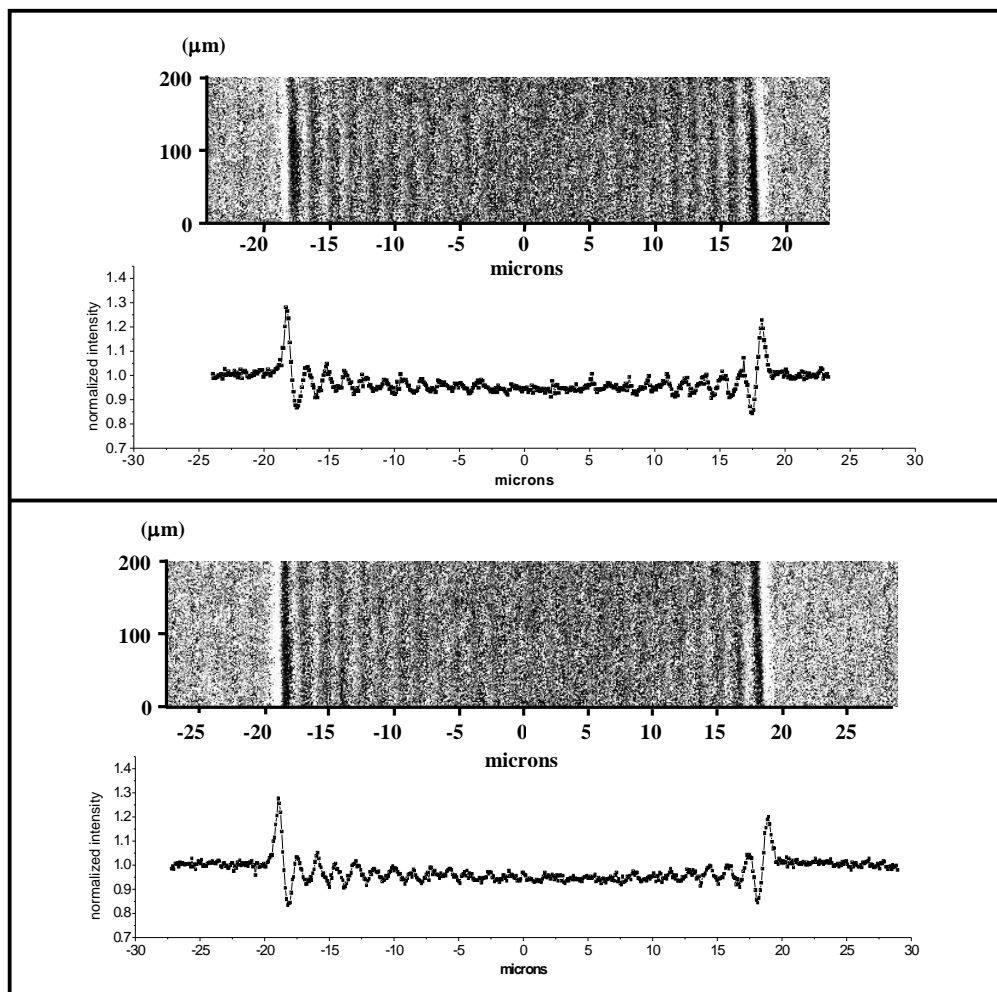
Figure 6.8*: Water sorption from a health hair which is "virgin" respect to cosmetic treatments. a) Before the water sorption and (b) after the water sorption. The measured diameter remains almost the same.*
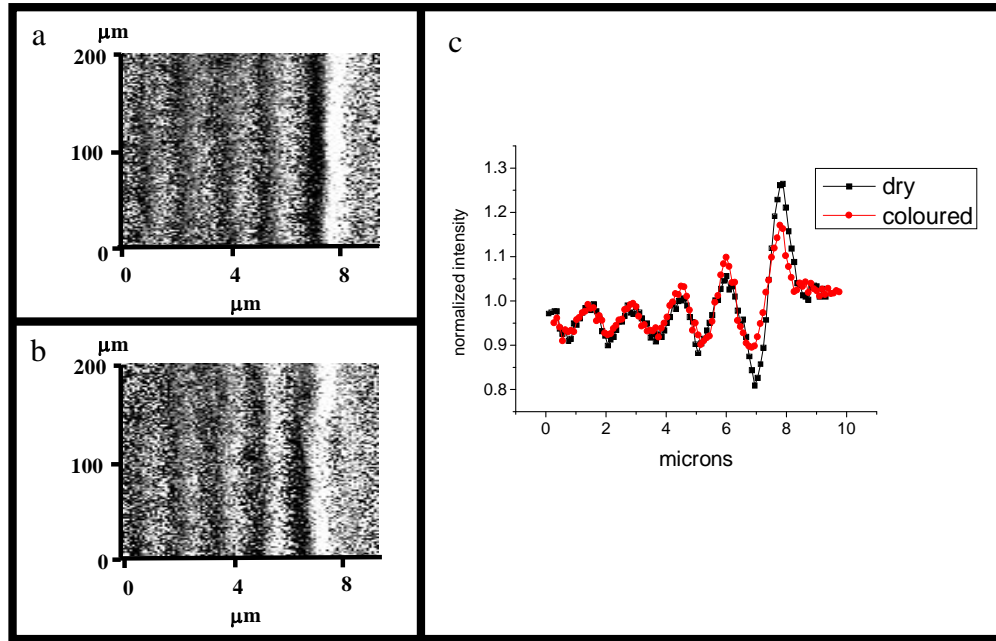
Figure 6.9: a) Edge region of the dry hair and b) edge region of the coloured hair as recorded by the CCD detector. Both measurements are a collage of two measures from two adjacent scan steps. The distances and the exposure time were the same in both cases ($z_1 \sim 2mm$, $z_1+z_2= 269mm$, $M=131$, $t=100s$). c) Corresponding intensity profiles. All the fringes remain almost the same but not the first one, i.e. the one which corresponds to the hair-air transition. Its visibility changes from $\sim 22\%$ to $\sim 16\%$.

6.8 Conclusions

The measurements reported in this chapter confirm that the PPCI technique allows the investigation of the internal structure of biological specimen. Moreover the use of the WG allow resolutions down to few hundreds nanometers which are impossible to get using a standard laboratory source. For instance in Fig. (6.10) the phase contrast image of a human hair recorded without the implementation of the WG is reported. In this case the source

dimension is given by the dimension of the Cu target of the microfocus source, i.e. $\approx 15\ \mu m$, and the estimated spatial resolution is $\approx 10\ \mu m$. The gain in resolution and contrast due to the implementation of the WG is evident. Extension to 2-D high resolution imaging using two planar WG in cross configuration is as well in progress. The expected exposure time is proportional to the resolution increase (in 1D), i.e. an increase a factor 10 moving from 1D to 2D high resolution imaging, for a given Signal-to-Noise, ratio is expected [Pelliccia, 2010]. 2D WGs have been also fabricated [Pfeiffer, 2002] and their optimization for laboratory x-ray sources is in progress. Finally, as it has previously reported, the problem of a limited field of view on a macroscopic sample can be overcome by the mean of a scan.

The results shown on the human hair cuticle structure look very interesting, but are indeed puzzling. If the fringes are secondary fringes from the hair-air transition, they would also occur in the air (outside the hair). Moreover the fringes occur even when the air-hair edge is not illuminated. These facts seem to exclude the possibility that the fringes are secondary fringes from the hair-air transition.

On the other hand, it seems premature to say that the fringes correspond to the scales that constitute the cuticle, mainly because of the sizes. As a matter of fact it is well accepted in the scientific community that the layers of cells that constitute it are much thinner and the average value generally reported is ~ 0.5 um.

A possible source of error could be the used values for the hair refraction index that was impossible to find in literature for the hard X-ray case and hence was roughly evaluated starting from the keratin composition in terms of raw elements. Moreover possible improvement of the experimental setup could be in the development of a sample holder which allow the control of the applied tension on the hair sample. Another relevant factor could be the control of the environment humidity. Finally, it must be remembered that the imaged hair samples in the presented work was not subjected to any kind of chemical or physical treatment and was imaged just few minutes after the cutting from the scalp.
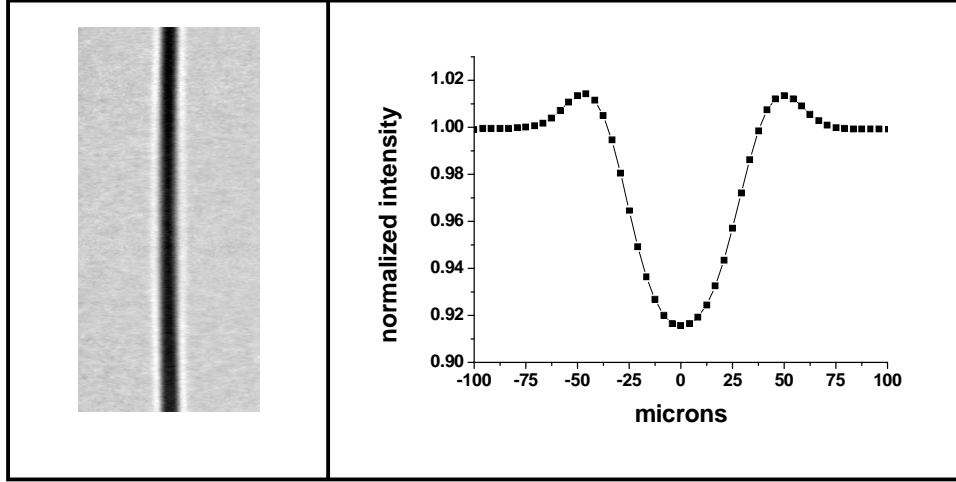
Figure 6.10: *a) Recorded image by the CCD camera and (b) corresponding intensity profile of a human hair using the projection microscope without the implementation of the WG. The used distances are $z_1 = 15$ cm, $z_1 + z_2 = 42$ cm. The magnification and resolution are ≈ 2.8 and ≈ 10 μm respectively. The hair diameter evaluated using a known movement of the motorized sample stage is ≈ 65 μm.*

Conclusion

X-ray phase contrast imaging is nowadays an established technique used to investigate the inner structure of materials in various scientific areas. The problem remains the limited applicability of such technique in a common laboratory setup. The work of the present thesis has been developed within this framework. The activity was focused on the Propagation based Phase Contrast Imaging technique implemented by the use of the X-ray WG optics.

When and why phase contrast is preferable respect to the standard absorption technique was clarified in the first part of Chapter 1, while the fundamental concepts and equation of the propagation based method was described in section 1.5.5. In Chapter 2 the WG basic theory was reported. Particularly fascinating is the possibility to use the WG as a coherent filter exploiting the self imaging effect as described in sections 2.6 and 2.7. The fabrication process for planar X-ray WG was described in Chapter 3. The adjustments of the various steps necessary to obtain a working air guiding layer with a dimension of few hundred nanometers were not a trivial issues. In Chapter 4 the WG based phase contrast microscope built up at the X-ray laboratory of the Institute for Photonics and Nanotechnology of Rome was described. Particular attention was focused on the choices made on the geometrical configuration of such a microscope. Very interesting are the measurements reported in sections 4.5 and 4.6 about the dependence of the resonance spots visibility and the microscope resolution on the quality of the WG entrance gap illumination. A first step forward to transfer X-ray coherent methods from large scale synchrotron radiation facilities to standard laboratory setups was made in Chapter 5. To our knowledge, no holography reconstruction results with such small resolution have ever been obtained in a standard laboratory. Finally in Chapter 6, very interesting measurements on human hair fibers were reported.

Summarizing, the principal goals reached till now are:

- The elaboration of a working fabrication process for planar front-coupling X-ray WG production (Chapter 3).

- The construction and the optimization of a WG based Propagation Phase Contrast microscope able to reach sub-micrometer resolutions (Chapter 4).

- The implementation of holographic reconstructions of test samples in a standard laboratory setup (Chapter 5).

- The demonstration of the applicability of the technique to the investigation of the inner structure of biological samples (Chapter 6).

A lot of work has to be making starting from these results.

The fabrication process allowed to build the structured WG described in section 2.7. The test of such innovative X-ray WGs optics is actually in progress. Moreover the basic ideas of the process will be utilized in order to fabricate a Neutron waveguide.

The built up microscope will be implemented with two planar WGs in cross configuration in order to realize 2D high resolution Phase Contrast Imaging experiments.

The measurements performed on the test samples which leads to the holographic reconstruction results reported in Chapter 5 will be repeated using a more brilliant primary source in order to improve the coherence properties of the beam imping on the sample.

Finally the measurements on human hair fibers reported in Chapter 6 will be repeated on more samples from different individuals in order to confirm the exceptional results obtained.

Appendix 1

Au test pattern structures fabrication process

Two different Au test structures were imaged during this thesis work. In chapter 4, an Au test structure was imaged in order to evaluate the effect of the X-ray beam degree of coherence at the WG entrance on the obtainable microscope resolution (section 4.6). Moreover in chapter 5 the same Au structure and another similar one were used in order to test the possibility to realize holographic reconstruction in a standard laboratory. Here the fabrication process of the structures will be briefly described. Some pictures, not in scale, are added in order to clarify each step of the process.

1- The Au structure are fabricated on a thin (100 nm) Si_3N_4 membrane. The first treatment is the evaporation of 10 nm of Au on the whole membrane in order to assure the electrical contact necessary for the successive Galvanic growth:

Au

Si_3N_4 membrane

10 nm
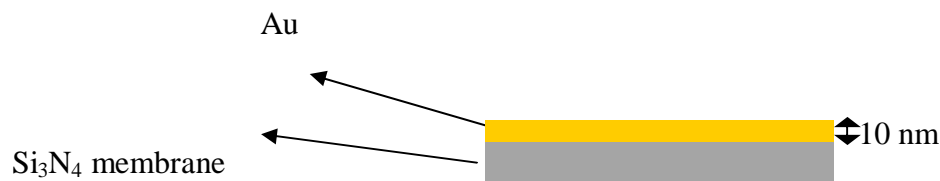
2- Then a 600 nm thick electronic resist is spun over it:

electronic resist

Au

600 nm

Si₃N₄ membrane
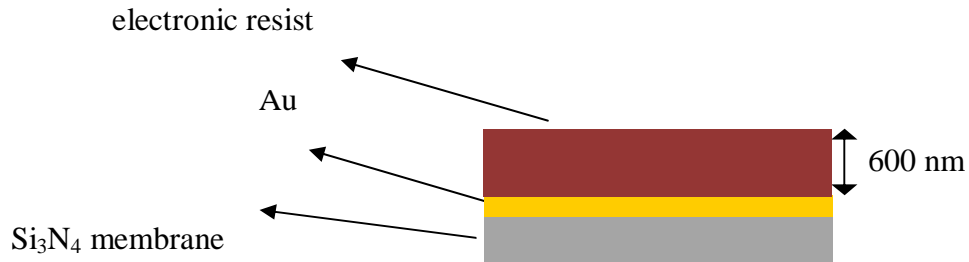
3- The test pattern figure is transferred on the resist by *electron beam lithography*:

Electron beam

electronic resist

Au

600 nm

Si₃N₄ membrane
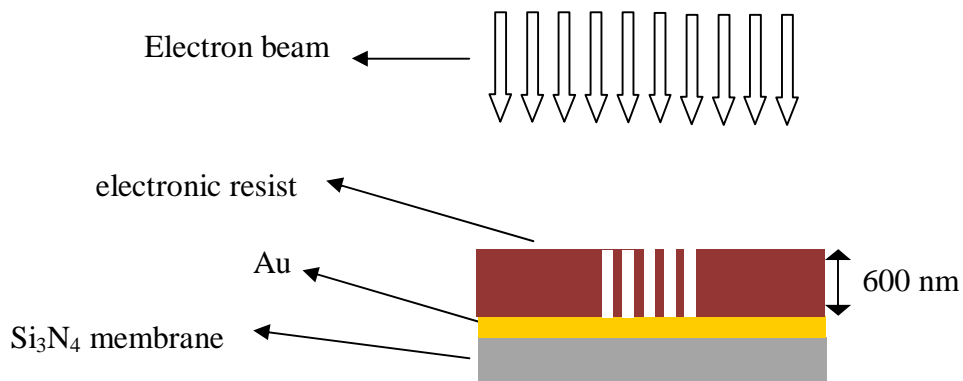
4- Therefore the structures are produced by an Au galvanic growth process. The galvanic process has been calibrated in order to obtain an Au thickness close as possible to the 600 nm resist thickness but not larger than it. The result of this calibration process is shown in Fig. (A1.1). The values of the thickness were measured using a suitable SEM measurement. As a consequence a galvanic growth time of 100 s was chosen. The corresponding measured Au structures thickness value is 580 nm as reported before.
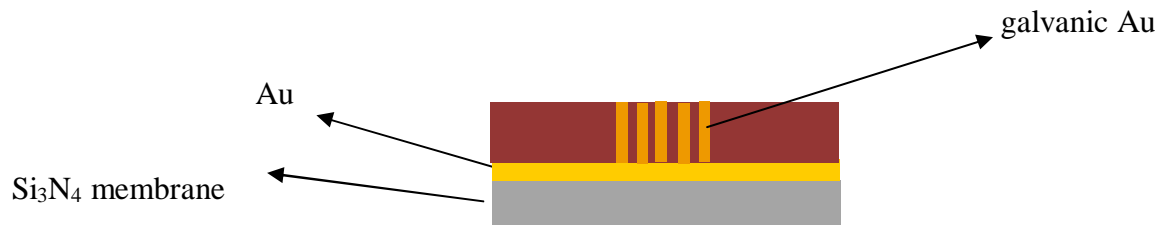
5- Finally the Resist is removed using hot acetone.
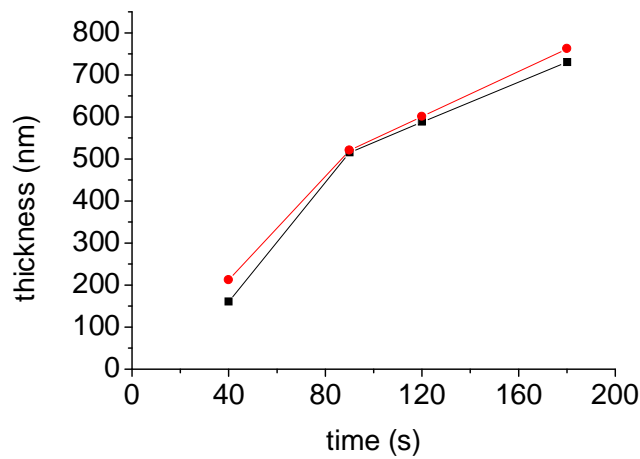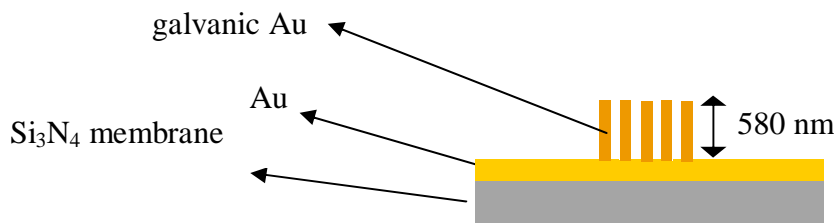
Figure A1:Preliminary galvanic growth calibration for both structures. The results suggested a galvanic growth time of about 100 s in order to obtain an Au thickness < 600 nm but close as possible to this value.

Appendix 2

WG exit gap dimension and WG exit field autocorrelation function

In section 4.5 a possible procedure to measure the WG exit gap dimension is briefly described (see Figs. (4.3)). Here the relation between the WG exit gap dimension and the width of the corresponding *autocorrelation function* of the exit field is explained. Let us denote the intensity of the diffraction pattern in the far-field from the WG (Fig. (4.3a)) with $\left|\tilde{V}(u)\right|^2$, where $\tilde{V}(u)$ is the FT of the field $V(x)$ at the WG exit. Naturally $\left|\tilde{V}(u)\right|^2$ is the accessible measurement.

For the inverse FT of $\left|\tilde{V}(u)\right|^2$ one has:

$$FT^{-1}\left[\left|\tilde{V}(u)\right|^2\right] = FT^{-1}\left[\tilde{V} \cdot \tilde{V}^*\right] = FT^{-1}\left[\tilde{V}\right] \otimes FT^{-1}\left[\tilde{V}^*\right] = V(x) \otimes -V^*(-x) \qquad \text{(A2.1)}$$

where FT^{-1} indicates the inverse FT operation, * denotes the complex conjugate and the theorem of convolution is applied. Therefore the inverse FT of the intensity at the detector plane $\left|\tilde{V}(u)\right|^2$ is equal to the so called autocorrelation function of the field $V(x)$ at the WG exit plane (see Fig.(4.3b)). Now assume for the amplitude of the field $V(x)$ in correspondence of the first resonance angle, a rectangular shape with same dimension of the WG exit gap. Therefore, equation (A2.1) gives, as a result of the convolution operation between two

identical rectangles [], a triangle (Fig.(4.3c), in first approximation) which dimension is twice the rectangle dimension of the WG exit gap.

Appendix 3

Preliminary two dimensional results

In order to obtain a two dimensional guided beam two air gap WG were aligned in cross configuration (see Fig. (A3.1)) in front of the Ultra Bright X-ray rotating anode source (Rigaku) located at the School of Physics of Monash University (Melbourne, Australia). The estimated brilliance is equal to 10^{13} photons/s/mm^2/mrad^2/(0.1% bandwidth) at Cu-K$_\alpha$ radiation energy, four orders magnitude bigger than the standard microfocus source used in Rome. The detector is a Medipix single photon without shot noise detector (pixels size = 55 µm). The distances are: source-WG1 = 120 cm, WG1- WG2 = 4,5 cm, WG2- detector = 75 cm.
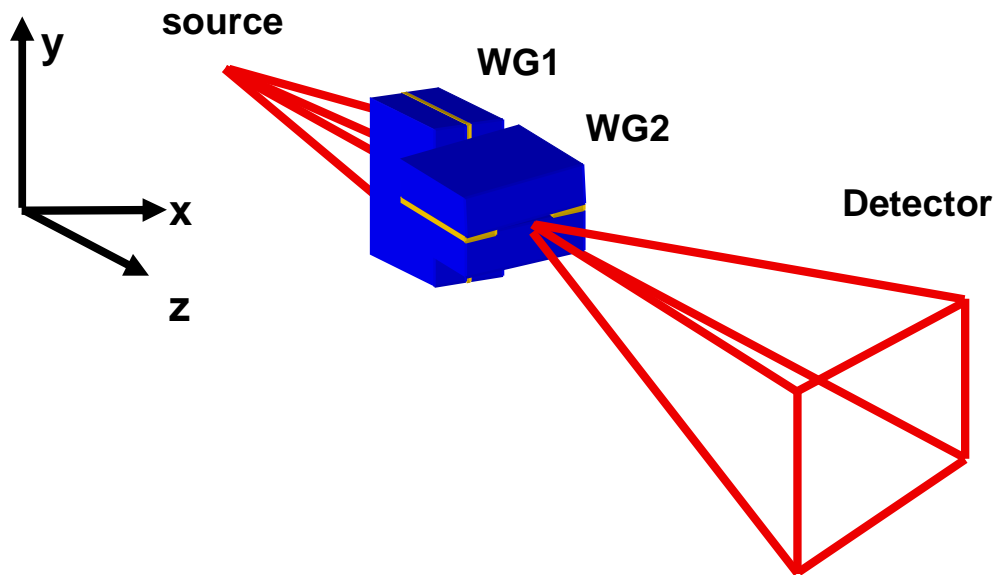
Figure A3.1*: Schematic layout for for the two dimensional WG- based microscope. The WGs are aligned in cross configuration in order to obtain a two dimensional guided beam.*

In Figs. (A3.2) the intensity on the detector is reported with a preliminary analisys of the recorded intensity. The acquisition time was 21 hours with a mean photon flux of 1 photon every 10 seconds. This very low value does not allow the allignement of a sample in the two dimensional guided beam.
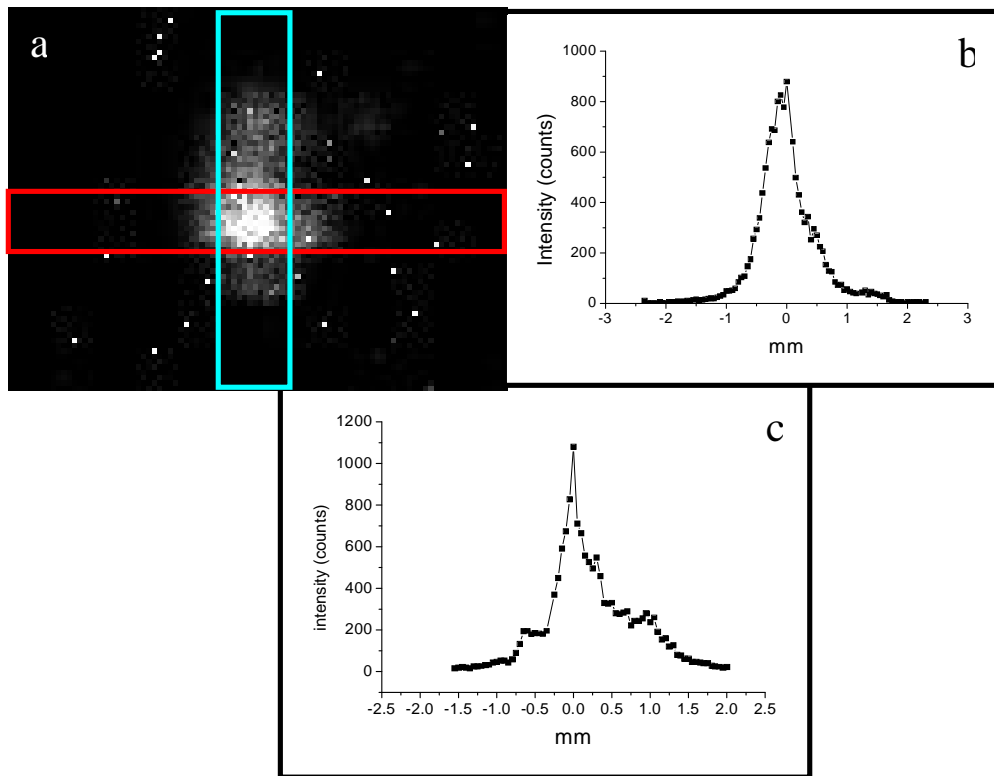
Figure A3.2: *a) Recorded intensity on the detector after 21 hours exposure time. b) Mean value over 10 pixels in vertical direction (red rectangle in a)). c) Mean value over 10 pixels in horizontal direction (blu rectangle in a). In both case the distances on the detector plane are reported in millimetres.*

It is important to stress here that the experimental setup does not allow the optimization of the experimental distances. Both the source- WG1 distance and the WG1-WG2 distances are too big to obtain an usable flux from the WGs.

Bibliography

[Arfelli, 2000]: F. Arfelli, Nucl. Instrum. Methods Phys. Res. Sect. A – Accel. Spectrom. Detect. Assoc. Equip. **454**, 11, (2000).

[Arfelli, 2000(2)]: F. Arfelli, V. Bonvicini, A. Bravin, G. Cantatore, E. Castelli, L. Dalla Palma, M. Di Michiel, M. Fabrizioli, R. Longo, R.H. Menk, A. Olivo, S. Pani, D. Pontoni, P. Poropat, M. Prest, A. Rashevsky, M. Ratti, L. Rigon, G. Tromba, A. Vacchi, E. Vallazza, and F. Zanconati, Radiology **215**, 286, (2000).

[Attwood, 1999]: D. Attwood, *Soft X-Rays and Extreme Ultraviolet Radiation*, Cambridge University Press, (1999).

[Bergemann, 2003]: Bergemann, C., Keymeulen, H. & van der Veen, J. F., Phys. Rev. Lett. **91**, 204801, (2003).

[Bogaty, 1969]: Bogaty, H.J.J. Soc. Cosmet. Chem. **20**, 159, (1969).

[Bonse & Hart, 1965]: U. Bonse e M. Hart, Appl. Phys. Lett. *6*, 155, (1965).

[Born, 1987]: M. Born & E. Wolf, *Principles of Optics*, Pergamon Press, Oxford (1987).

[Bryngdahl, 1973]: O. Bryngdahl, J. Opt. Soc. Am. **63**, 41 (1973).

[Bukreeva, 2010]: I. Bukreeva, D. Pelliccia, A. Cedola, F. Scarinci, M. Ilie, C. Giannini, L. De Caro and S. Lagomarsino, J. Synchrotron Rad. **17**, 61, (2010).

[Bukreeva, 2011]: I. Bukreeva, A. Cedola, A. Sorrentino, D. Pelliccia, V. Asadchikov, S. Lagomarsino, Optics Letters **36** (14), 2602, (2011).

[Busson, 1999]: B. Busson, P. Engstro, and J. Doucet**,** J. Synchrotron Rad., **6**, 1021, (1999).

[Cazaux, 1997]: J. Cazaux, J. of Microscopy **188**, 106.

[Chapman, 1997]: D. Chapman, W. Thomlinson, R.E. Johnston, D. Washburn, E. Pisano, N. Gmur, Z. Zhong, R. Menk, F. Arfelli, and D. Sayers, Phys. Med. Biol. **42**, 2015, (1997).

[Chapman, 2006]: H.N. Chapman, *Nature Phys.* **2**, 839 (2006).

[Cloetens, 1997]: P. Cloetens, M. PateyronSalome, J.Y. Buffiere, G. Peix, J. Baruchel, F. Peyrin, and M. Schlenker, J. Appl. Phys. **81**, 5878, (1997).

[Cloetens, 1999]: P. Cloetens, W. Ludwig, J. Baruchel, D. Van Dyck, J. Van Landuyt, J. P. Guigay, and M. Schlenker, Appl. Phys. Lett., **75**, 2912 (1999).

[Cloetens, 1999(2)]: PhD Thesis, (1999).

[Cowley, 1995]: J.M. Cowley, *Diffraction Physics*, North Holland, Amsterdam, (1975).

[Croce, 1976]: P. Croce and L. Nevot, Revue Phys. Appl. **11**, 113, (1976).

[David, 2007]: C. David, T. Weitkamp, F. Pfeiffer, A. Diaz, J. Bruder, T. Rohbeck, A. Groso, O. Bunk, M. Stampanoni, and P. Cloetens, Spectrochim. Acta Part B – At. Spectrosc. **62**, 626, (2007).

[Davis, 1995]: T.J. Davis, D. Gao, T.E. Gureyev, A.W. Stevenson, and S.W. Wilkins, Nature **373**, 595, (1995).

[De Caro, 2007]: De Caro, L., Giannini, C., Cedola, A.,Pelliccia, D., Lagomarsino, S. & Jark, W., Appl. Phys. Lett. **90**, 041105, (2007).

[De Caro, 2008]: L. De Caro, A. Cedola, C. Giannini, I. Bukreeva and S. Lagomarsino, Phys. Med. Biol. **53,** 6619, (2008).

[De Caro, 2008(2)]: De Caro, L., Giannini, C., Pelliccia, D., Mocuta, C., Metzger, T. H.,Guagliardi, A., Cedola, A., Bukreeva, I. & Lagomarsino, S., Phys. Rev. B, **77**, 081408, (2008).

[Di Fonzo, 2000]: Di Fonzo, S., Jark, W., Lagomarsino, S., Giannini, C., De Caro, L.,Cedola, A. & Muller, M., Nature **403**, 638, (2000).

[Elwenspoek, 1998]: M. Elwenspoek and H. Jansen, *Silicon Micromachining,* Cambridge University Press, (1998).

[Feng, 1995]: Y.P. Feng, S.K. Sinha, E.E. Fullerton, G. Grubel, D. Abernathy, D.P. Siddons and J.B. Hastings, Appl. Phys. Lett. **67**, 3647, (1995).

[Fienup, 1978]: J. R. Fienup, Opt. Lett. **3**, 27, (1978).

[Fienup, 1980]: J. R. Fienup, Opt. Lett. **19**, 297, (1980).

[Fienup, 1982]: J. R. Fienup, Appl. Opt. **21** (15), 2758, (1982).

[Fienup, 1986]: J. R. Fienup, and C. Wackerman, J. Opt. Soc. Am. A **3**, 1897, (1986).

[Gabor, 1948]: Gabor, D., Nature **161**, 777f, (1948).

[Gerchberg, 1972]: R.W. Gerchberg and W.O. Saxton, Optik **35**, 237, (1972).

[Giewekemeyer, 2010]: K. Giewekemeyer, H. Neubauer, S. Kalbfleisch, S. P. Krüger, and T. Salditt, New Journal of Physics **12**, 035008, (2010).

[Giewekemeyer, 2011]: K. Giewekemeyer, S. P. Kr¨uger, S. Kalbfleisch, M. Bartels, C. Beta, and T. Salditt, Physical Review A **83**, 023804, (2011).

[Goodman, 1988]: J. Goodman, *Introduction to Fourier Optics*, McGraw-Hill, New York, (1988).

[Gori, 1995]: F. Gori, *Elementi di ottica,* Accademica, Roma (1995).

[Grunzweig, 2008]: C. Grunzweig, F. Pfeiffer, O. Bunk, T. Donath, G. Kuhne, G. Frei, M. Dierolf, and C. David, Rev. Sci. Instrum. **79**, 053703, (2008).

[Helfert, 2009]: S. F. Helfert, B. Huneke, and J. Jahns, J. Eur. Opt. Soc. Rapid Pub. **4**, 09031, (2009).

[Hirano, 1999]: K. Hirano and A. Momose, Jpn. J. Appl. Phys. **2** (38), 1556 (1999).

[Hooper, 2009]: S.B. Hooper, M.J. Kitchen, M.L. Siew, R.A. Lewis, A. Fouras, A.B.T. Pas, K.K. Siu, N. Yagi, K. Uesugi, and M.J. Wallace, Clin. Exp. Pharm. Physiol. **36**, 117, (2009).

[Ingal, 1995]: V.N. Ingal and E.A. Beliaevskaya, J. Phys. D – Appl. Phys. **28**, 2314, (1995).

[Jacobsen, 1990]: C. Jacobsen, M. Howells, J. Kirz, S. Rothman, J. Opt. Soc. Am. A **7** (10), 1847, (1990).

[Jahns, 2009]: J. Jahns and A. W. Lohmann, Appl. Opt. **48**, 3438 (2009).

[Jark, 2004]: W. Jark and S. Di Fonzo, *J. Synchrotron Rad.* **11**, 386 (2004).

[Jark, 2001]: Jark, W., Cedola, A., Di Fonzo, S., Fiordelisi, M., Lagomarsino, S., Kovalenko, N.V., Chernov, V.A., Appl. Phys. Lett. **78**, 1192, (2001).

[Jheon, 2006]: S. Jheon, H.S. Youn, H.T. Kim, G.H. Choi, and J.K. Kim, Microsc. Res. Tech. **69**, 656, (2006).

[Kaswell, 1953]: Kaswell, E.R. Textile Fibers, Yarns and Fabrics, p.52, Reinhold, New York (1953).

[Khon, 1997]: V.G. Khon, Physica Scripta **56**, 14, (1997).

[Klemm, 1965]: Klemm, E. et al., Proc. Sci. Sect.T.G.A. **43**, 7, (1965).

[Kohlstedt, 2008]: Kohlstedt, S. Kalbfleisch T. Salditt, M. Reiche U. Gösele E. Lima P. Willmott, Appl. Phys. A **91**, 7, (2008).

[Kopylov, 1995]: Y. V. Kopylov, A. V. Popov, and A. V. Vinogradov, Opt. Commun. **118**, 619 (1995).

[Kottler, 2007]: C. Kottler, F. Pfeiffer, O. Bunk, C. Grunzweig, J. Bruder, R. Kaufmann, L. Tlustos, H. Walt, I. Briod, T. Weitkamp, and C. David, Phys. Status Solidi A – Appl. Mater. Sci. **204**, 2728, (2007).

[Koyama, 2005]: I. Koyama, A. Momose, J. Wu, T.T. Lwin, and T. Takeda, Jpn. J. Appl. Phys. Part 1 – Regul. Papers Brief Commun. Rev. Papers **44**, 8219, (2005).

[Kreplak, 2001]: L. Kreplak, C. Mèrigoux, F. Briki, D. Flot, J. Doucet, Biochimica et Biophysica Acta **1547**, 268, (2001).

[Krepalk, 2002]: L. Krepalk, A. Franbourg, F. Briki, F. Leroy, D. Dallè and J. Doucet, Biophys. Acta **1547**, 268, (2002).

[Lagomarsino, 1996]: S. Lagomarsino, W. Jark, S. Di Fonzo, A. Cedola, B. Mueller, P. Engstrom and C. Riekel, J. Appl. Phys. **79**, 4471, (1996).

[Lagomarsino, 1997]: Lagomarsino, S., Cedola, A., Cloetens, P., Di Fonzo, S., Jark, W.,Soullie´, G. & Riekel, C., Appl. Phys. Lett. **71**, 2557, (1997).

[Lak, 2008]: M. Lak, D. Neraudeau, A. Nel, P. Cloetens, V. Perrichot, and P. Tafforeau, Microsc. Microanal. **14**, 251, (2008).

[Lewis, 2003]: R.A. Lewis, C.J. Hall, A.P. Hufton, S. Evans, R.H. Menk, F. Arfelli, L. Rigon, G. Tromba, D.R. Dance, I.O. Ellis, A. Evans, E. Jacobs, S.E. Pinder, and K.D. Rogers, Br. J. Radiol. **76**, 301, (2003).

[Lindaas, 1994]: PhD Thesis, (1994).

[Lindaas, 1996]: S. Lindaas, B. Calef, K. Downing, M. Howells, C. Magowan, D. Pinkas, and C. Jacobsen, in XRM '96.

[Lohmann, 2005]: A. W. Lohmann, H. Knuppertz, and J. Jahns, J. Opt. Soc. Am. A 22, 1500 (2005).

[L'Oreal web-site]:

http://www.hair-science.com/_int/_en/topic/topic_sousrub.aspx?tc=ROOT-HAIR-SCIENCE^PORTRAIT-OF-AN-UNKNOWN-ELEMENT^WHAT-WE-DO-SEE&cur=WHAT

[Marcuse, 1974]: Marcuse, D., *Theory of Dielectric Optical Waveguides.* Academic Press, New York and London, (1974).

[Mayo, 2003]: S.C. Mayo, T.J. Davis, T.E. Gureyev, P.R. Miller, D. Paganin, A. Pogany, A.W. Stevenson, and S.W. Wilkins, Opt. Express **11**, 2289, (2003).

[Merigoux, 2003]: C. Merigoux, F. Briki, F. Sarrot-Reynauld, M. Salomé, B. Fayard, J. Susini and J. Doucet, Biochim. Biophys. Acta **1619**, 53, (2003).

[Miao, 1999]: J. Miao, P. Charalambous, J. Kirz, D. Sayre, Nature **400**, 342 (1999).

[Miao, 2002]: Miao, J. W., Ishikawa, T., Johnson, B., Anderson, E. H., Lai, B. &Hodgson, K. O., Phys. Rev. Lett. **89**, 088303, (2002).

[Mizutani, 2007]: H. Mizutani, Y. Takeda, A. Momose, and T. Takagi, Neurosci. Res. **58**, 184, (2007).

[Momose, 1995]: A. Momose, T. Takeda, and Y. Itai, Acad. Radiol. **2**, 883, (1995).

[Momose, 1995(2)]: A. Momose and J. Fukuda, Med. Phys. **22**, 375, (1995).

[Momose, 2005]: A. Momose, A. Fujii, H. Kadowaki, and H. Jinnai, Macromolecules **38**, 7197, (2005).

[Momose, 2006]: A. Momose, W. Yashiro, Y. Takeda, Y. Suzuki, and T. Hattori, Jpn. J. Appl. Phys. Part 1 – Regul. Papers Brief Commun. Rev. Papers **45**, 5254, (2006).

[Nesterets, 2004]: Y.I. Nesterets, T.E. Gureyev, D. Paganin, K.M. Pavlov, and S.W. Wilkins, J. Phys. D – Appl. Phys. **37**, 1262, (2004).

[Nesterets, 2006]: Y.I. Nesterets, P. Coan, T.E. Gureyev, A. Bravin, P. Cloetens, and S.W. Wilkins, Acta Crystallogr. Sect. A **62**, 296, (2006).

[Nugent, 1996]: K.A. Nugent, T.E. Gureyev, D.F. Cookson, D. Paganin e Z. Barnea, Phys. Rev. *77* (14) 2961, (1996).

[Nugent, 2010]: K.A. Nugent, Advances in Physics, **59** (1), 1, (2010).

[Olivo, 2001]: A. Olivo, F. Arfelli, G. Cantatore, R. Longo, R.H. Menk, S. Pani, M. Prest, P. Poropat, L. Rigon, G. Tromba, E. Vallazza, and E. Castelli, Med. Phys. **28**, 1610, (2001).

[Olivo, 2007]: A. Olivo & D. Speller, Phys Med Biol **52**, 6555, (2007).

[Olivo, 2011]: A. Olivo, K. Ignatyev, P. R. T. Munro, and R. D. Speller, APPLIED OPICS **50** (12), 1765, (2011).

[Ollinger, 2005] Ollinger, C., Fuhse, C., Jarre, A. & Salditt, T., Physica B, **357**, 53, (2005).

[Paganin, 2002]: D. Paganin, S.C. Mayo, T.E. Gureyev, P.R. Miller, and S.W. Wilkins, Journal of Microscopy **206**, 33, (2002).

[Pagot, 2003]: E. Pagot, P. Cloetens, S. Fiedler, A. Bravin, P. Coan, and J. Baruchel, J. Hartwig and W. Thomlinson, Appl. Phys. Lett. **82**, 3421, (2003).

[Pantene web-site]: www.pantene.com/en-us/hair-science/Pages/hair-structure-science.aspx

[Pavlov, 2004]: K.M. Pavlov, T.E. Gureyev, D. Paganin, Y.I. Nesterets, M.J. Morgan, and R.A. Lewis, J. Phys. D – Appl. Phys. **37**, 2746, (2004).

[Pelliccia, 2007]: Pelliccia, D., Bukreeva, I., Ilie, M., Jark, W., Cedola, A., Scarinci, F., Lagomarsino, S., Spectrochim. Acta B **62**, 615, (2007).

[Pelliccia, 2010]: D. Pelliccia, A. Sorrentino, I. Bukreeva, A. Cedola, F. Scarinci, M. Ilie, A.M. Gerardino, M. Fratini, and S. Lagomarsino, OPTICS EXPRESS **18** (15), 15998, (2010).

[Perrichot, 2008]: V. Perrichot, L. Marion, D. Neraudeau, R. Vullo, and P. Tafforeau, Proc. R. Soc. Lond. B – Biol. Sci. **275**, 1197, (2008).

[Pfeiffer, 1999]: F. Pfeiffer, Diploma thesis, Ludwig-Maximilians-Universit¨at M¨unchen, Sektion Physik, Munich, Germany, (1999).

[Pfeiffer, 2002]: F. Pfeiffer, C. David, M. Burghammer, C. Riekel and T. Salditt, Science **297**, 230, (2002).

[Pfeiffer, 2006]: F. Pfeiffer, T. Weitkamp, O. Bunk, and C. David, Nature Phys. **2**, 258, (2006).

[Pfeiffer, 2007]: F. Pfeiffer, O. Bunk, C. Kottler, and C. David, Nucl. Instrum. Methods Phys. Res. Sect. A – Accel. Spectrom. Detect. Assoc. Equip. **580**, 925, (2007).

[Pogany, 1997]: A. Pogany, D. Gao e S.W. Wilkins, Rev. Sci. Instrum. **68** (7), 2774, (1997).

[Rau, 2006]: C. Rau, I.K. Robinson, and C.P. Richter, Microsc. Res. Tech. **69**, 660, (2006).

[Reynolds, 1989]: G.O. Reynolds, J.B. De Velis, G.B. Parrent Jr., e B.J. Thompson, *The New Physical Optics Notebook: Tutorial in Fourier Optics,* Spie Optical Engineering Press, (1989).

[Robinson, 2001]: I.K. Robinson, I.A. Vartanyants, G.J. Williams, M.A. Pfeifer, J.A. Pitney, Phys. Rev. Lett. **87**, 195505 (2001).

[Robbins, 2002]: C. R. Robbins, "Chemical and physical behaviour of human hair", p.2, Springer, (2002).

[Robinson, 2003]: I.K. Robinson, F. Pfeiffer, I.A. Vartanyants, Y. Sun, Y. Xia, Optics Express **11**, 2329, (2003).

[Randebrook, 1964]: Randebrook, R.J.J., Soc. Cosmet. Chem. **15**, 691, (1964).

[Salditt, 2008]: T. Salditt, S.P. Kruger, C. Fuhse, and C. Bahtz, Phys. Rev. Lett. **100**, 184801, (2008).

[Salome, 1999]: M. Salome, F. Peyrin, P. Cloetens, C. Odet, A.M. Laval-Jeantet, J. Baruchel, and P. Spanne, Med. Phys. **26**, 2194, (1999).

[Sayre, 1952]: D. Sayre, Acta Crystallogr. **5**, 843 (1952).

[Sinha, 1988]: S.K. Sinha, E.B. Sirota, S. Garoff, H.B. Stanley, Phys. Rev. B **38**, 22976, (1988).

[Snigirev, 1995]: A. Snigirev, I. Snigireva, V. Kohn, S. Kuznetsov e I. Schelokov, Rev. Sci. Instrum. *66* (2), 5486, (1995).

[Spanne, 1999]: P. Spanne, C. Raven, I. Snigireva, and A. Snigirev, Phys. Med. Biol. **44**, 741, (1999).

[Strobl, 2008]: M. Strobl, C. Gruenzweig, A. Hilger, I. Manke, N. Kardjilov, C. David, and F. Pfeiffer, Phys. Rev. Lett. **101**, 123902, (2008).

[Swift, 2001]: Swift, J.A. & Smith, J.R., J. Microsc. **204**, 203, (2001).

[Smith, 2005]: J. R. Smith, J.A. Swift, Micron **36**, 261, (2005).

[Takeda, 1995]: T. Takeda, A. Momose, Y. Itai, J. Wu, and K. Hirano, Acad. Radiol. **2**, 799, (1995).

[Takeda, 2000]: T. Takeda, A. Momose, K. Hirano, S. Haraoka, T. Watanabe, and Y. Itai, Radiology **214**, 298, (2000).

[Takeda, 2000(2)]: T. Takeda, A. Momose, Q.W. Yu, T. Yuasa, F.A. Dilmanian, T. Akatsuka, and Y. Itai, Cell. Mol. Biol. **46**, 1077, (2000).

[Talbot, 1836]: H. F. Talbot, Philosophical Mag. **9**, 401, (1836).

[Tafforeau, 2006]: P. Tafforeau, R. Boistel, E. Boller, A. Bravin, M. Brunet, Y. Chaimanee, P. Cloetens, M. Feist, J. Hoszowska, J.J. Jaeger, R.F. Kay, V. Lazzari, L. Marivaux, A. Nel, C. Nemoz, X. Thibault, P. Vignaud, and S. Zabler, Appl. Phys. A– Mater. Sci. Process. **83**, 195, (2006).

[Tafforeau, 2008]: P. Tafforeau and T.A. Smith, J. Hum. Evol. **54**, 272, (2008).

[Thurner, 2003]: P. Thurner, B. Muller, F. Beckmann, T. Weitkamp, C. Rau, R. Muller, J.A. Hubbell and U. Sennhauser, Nucl. Instrum. Methods Phys. Res. Sect. B – Beam Interact. Mater. Atoms **200**, 397, (2003).

[Ulrich, 1975]: R. Ulrich, Opt. Commun. 13, 259 (1975).

[Van der Veen, 2004]: F. Van der Veen and F. Pfeiffer, J. Phys.: Condens Matter *16*, 5003, (2004).

[Weitkamp, 2005]: T. Weitkamp, A. Diaz, C. David, F. Pfeiffer, M. Stampanoni, P. Cloetens, and E. Ziegler, OPTICS EXPRESS **13** (16), 6296, (2005).

[Wilkins, 1996]: S.W. Wilkins, T.E. Gureyev, D. Gao, A. Pogany, e A.W. Stevenson, Nature *384*, 335, (1996).

[Williams, 2003]: G.J. Williams, M.A. Pfeifer, I.A. Vartanyants, I.K. Robinson, Phys. Rev. Lett **90**, 175501, (2003).

[Williams, 2007]: Williams, G.J., Quiney, H.M., Peele, A.G., Nugent, K.A., Phys. Rev. B **75**, 104102, (2007).

[Zabler, 2006]: S. Zabler, H. Riesemeier, P. Fratzl, and P. Zaslansky, Opt. Express **14**, 8584, (2006).